

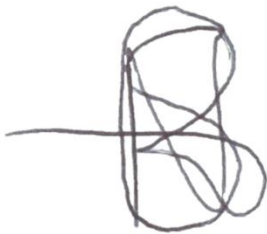
Reclaiming carbon from waste polymers via thermal decomposition using liquid metal alloys

Department of Chemistry and Biotechnology,
School of Science, Computing, and Engineering Technologies,
Swinburne University of Technology

Nicolas Schuecker-Rush
24-10-2023

Declaration

I hereby declare that this thesis is my original work and to the best of my knowledge does not contain material previously published or written by another person, except where the material has been properly acknowledged and reference as such made in text. This thesis also includes text and figures which were present in three of my original publications in journals. Wherever contributions of others were involved it was attempted to the best of my effort to acknowledge the respective workers and authors.

A handwritten signature in black ink, consisting of several overlapping loops and a long horizontal stroke extending to the left.

24-10-2023

Abstract

The massive production of a variety of polymers, mostly derived from fossil-fuel, poses serious threat to both the environment and human health. While nowadays there is a global consciousness about the issue of plastic waste, as a result of their ubiquitous usage, we are yet to find a sustainable surrogate to most general use polymers. For this reason, a major environmental issue is the increasing quantities of plastic waste, with less than 10% of that waste being successfully recycled. The majority is incinerated, sent to landfill, or ends up in the environment. There is thus a considerable need to identify environmentally friendly solutions. This work explores a novel low temperature tertiary recycling method using a liquid metal reaction medium to generate amorphous carbonaceous materials such as carbon black from waste polymer. The approach meets the criteria defining the cradle-to-cradle paradigm, being able to sequester waste plastic from the environment by transforming it into a high value material used in many industrial applications. It is cradle-to-cradle in its approach as it transforms the waste plastic into a pristine source of raw materials that could be used in numerous applications, thus reducing reliance on fossil-based resources. Finally, when taking into account the negative value of plastic waste, and the low energy requirements of this product, it is hopeful that this method could be further developed into an economically viable large-scale process. The core of the research consisted in designing and optimising a custom reactor, alongside with the preparation of a series of liquid metal alloys (gallium, eutectic gallium-indium, galinstan, and eutectic bismuth-tin). The carbonaceous products of various waste plastics are fully characterised by conventional and advanced analytical techniques (XRD, SEM, XPS, Raman, UV-Vis, TGA, BET, FTIR) and compared. This work also assesses methods for improving reaction rates and yields as well as product consistency of the process through precursor modifications: incorporating a secondary material to improve the thermal cracking of the polymers. The main results are critically discussed and speculation towards future experimental modifications are given.

Acknowledgements

First and foremost, I would like to thank my wonderful partner Nkumbu Sikanyika for her support throughout my time in my PhD. Through ups and downs, she was always a compassionate and understanding person that I could vent my excitements and frustrations to.

I would also like to extend my thanks to my parents Robert Schuecker and Tracey Rush for their encouragement and financial support throughout. Without their help, there would have been no way I could have provided for myself financially throughout this endeavour and I am eternally grateful to them.

I would like to thank my supervisors Dr François Malherbe and Prof Aimin Yu for their guidance throughout this project, without their insight I would not have been able to develop my project into what it became. I would also like to thank my fellow PhD students, particularly Parisa Tafazolymotie, for their assistance and advice when working in the lab. Their input definitely helped make things easier and to run smooth even if the equipment was constantly breaking.

For their assistance throughout my work, I would also like to thank the technical staff at Swinburne University of Technology especially for putting up with my requests and questions to do with various topics. Without them, none of this would have been possible.

Additionally, I'd like to thank all my friends. Many of you are completing or have completed your PhDs and having a network of people I can bounce ideas off and seek advice from has been invaluable to me.

The maintenance of my sanity I owe to the good folks at Ramblers Aleworks. Their delicious beverages have gotten me through more hard times than I care to admit.

Finally, I would like to extend my thanks to the Australian Government for the funding of my PhD through the RTP scholarships program.

Table of Contents

Declaration.....	2
Abstract.....	3
Acknowledgements.....	4
Figures.....	9
Tables.....	13
Equations.....	14
Abbreviations.....	15
Chapter 1: Introduction.....	16
1.1: Overview.....	17
1.2: Structure of the thesis.....	18
Chapter 2: Literature review.....	20
2.1: Introduction.....	21
2.1.1: Current recycling techniques.....	23
2.1.2: Tertiary recycling.....	25
2.1.3: Waste plastics as a material source.....	28
2.2: Carbonisation.....	32
2.2.1: Zero-dimensional carbons.....	34
2.2.2: One-dimensional carbons.....	37
2.2.3: Two-dimensional carbons.....	38
2.3: Liquid metals.....	42
2.3.1: Metallurgical overview.....	42
2.3.2: Properties of liquid metals.....	45
2.3.3: Liquid metals in chemical reactions.....	46
2.3.4: Fluid dynamics and their effect on reactor design.....	50
2.4: Summary.....	52

Chapter 3: Materials and methods	54
3.1: Overview	55
3.2: Materials and reagents	55
3.3: Processing and production of materials and reagents	55
3.4: General apparatus setup and use of reactor	55
3.5: General modification of polymer precursors.....	57
3.6: Post-run processing.....	58
3.7: Product characterisation.....	58
3.7.1: Scanning electron microscopy	58
3.7.2: Energy dispersive X-ray analysis	58
3.7.3: Raman spectroscopy.....	59
3.7.4: X-ray diffraction	59
3.7.5: Fourier-transform infrared spectroscopy	59
3.7.6: Ultraviolet-visible spectroscopy	59
3.7.7: Thermogravimetric analysis.....	59
3.7.8: X-ray photoelectron spectroscopy	59
3.7.9: Nitrogen adsorption.....	60
3.8: Software	60
Chapter 4: Carbonisation of polyethylene and the effects of liquid metals	61
4.1: Introduction	62
4.2: Reactor design.....	63
4.3: Reactor optimisation.....	66
4.4: Effect of liquid metals on carbonisation	68
4.4.1 Gallium	68
4.4.2: Eutectic gallium-indium	69
4.4.3: Galinstan	69

4.4.4: Eutectic bismuth-tin.....	69
4.5: Raman spectroscopy of carbon products	70
4.6: Summary of findings	75
Chapter 5: Low temperature carbonisation of plastics using galinstan	76
5.1: Introduction	77
5.2: Decomposition characteristics of plastics.....	79
5.3: Polymer carbonisation	81
5.4: Characterisation of plastic derived carbon materials	88
5.4.1: Scanning electron microscopy	88
5.4.2: Energy dispersive X-ray elemental mapping	89
5.4.3: Energy dispersive X-ray analysis	91
5.4.4: Raman spectroscopy.....	92
5.4.5: X-ray photoelectron spectroscopy	101
5.5: Summary of findings	108
Chapter 6: Modification of plastic precursor materials.....	109
6.1: Introduction	110
6.2: Modification of plastic precursors	111
6.2.1: Fourier transform infrared spectroscopy of the modified plastic precursors.....	112
6.3: Properties of metal oxides	115
6.4: TGA of plastic composites	119
6.5: Properties of carbon derived from modified precursors.....	122
6.5.1: X-Ray diffraction	122
6.5.2: Raman spectroscopy.....	125
6.5.3: X-ray photoelectron spectroscopy	137
6.6: Summary of findings	146
Chapter 7: Conclusions and future work	147

7.1: Conclusions	148
7.2: Future work.....	148
8: References	150

Figures

Figure 2.1: The Plastic Cycle.	21
Figure 2.2: Infographic showing resin code pictograms and their recycling status in Australia.	28
Figure 2.3: A diagram of the schematic structure of N-graphene. Pyrrolic nitrogen shown in red, pyridinic nitrogen shown in red and internal pyridinic nitrogen shown in green.	30
Figure 2.4: Diagram demonstrating charge mobility in sp^2 hybridized carbon species.	38
Figure 2.5: A schematic representation of bulk and interfacial applications of liquid metals. Adapted from work from ⁹⁹	47
Figure 2.6: A proposed mechanism for methane dehydrogenation and nucleation of carbonaceous materials in liquid metal. Adapted from work from ¹⁰⁹	48
Figure 4.1: Custom reactor used for low temperature carbonisation of plastics.	63
Figure 4.2: An example of the thermocouple flange setup used to calibrate internal furnace temperatures under reaction conditions.	64
Figure 4.3: A close-up schematic of the bubble column; point 3 in Figure 4.1.	65
Figure 4.4: A schematic illustration of dangling bonds in an aromatic carbon lattice.	70
Figure 4.5: Raman spectrum of a carbonaceous sample produced from waste PE in EGaIn with Smith et al. deconvolution method ¹⁴² applied.	71
Figure 4.6: Raman spectrum of a carbonaceous sample produced from waste PE in galinstan with Smith et al. deconvolution method ¹⁴² applied.	73
Figure 5.1: Consumption of plastics in Australia, and proportion produced from locally recycled sources ¹⁵³	78
Figure 5.2: TGA/DTG graphs of various plastics.	80
Figure 5.3: Thermal decomposition pathways for polyethylene ¹⁵⁴	81
Figure 5.4: Thermal decomposition pathways for polypropylene ¹⁵⁴	82
Figure 5.5: Thermal decomposition pathways for polystyrene ¹⁵⁴	83
Figure 5.6: Thermal decomposition pathways for polyacrylonitrile ¹⁵⁷	85
Figure 5.7: Thermal decomposition pathways for polyamides ¹⁵⁹	86

Figure 5.8: SEM images of PE sample showing (a) an overview of morphologies seen, (b) magnified view of the clump morphologies, and (c) a close look of the surface of a sphere morphology.....	89
Figure 5.9: SEM image and EDX elemental mapping of a carbonisation sample using a PAN precursor.....	90
Figure 5.10: SEM image and EDX elemental mapping of a carbonisation sample using a PET precursor.....	91
Figure 5.11: (a) Raman spectra of carbonaceous samples produced from several waste polymers. An example of Smith et al. deconvolution method ¹⁴² applied to (b) polyethylene, (c) polyethylene terephthalate, (d) polypropylene, (e) polystyrene, and (f) polyacrylonitrile derived carbon respectively.....	94
Figure 5.12: A proposed structural example of plastic derived carbon from systems (a) with pure hydrocarbon precursors & (b) precursors with endogenous heteroatoms.....	99
Figure 5.13: A chart of deconvoluted intensity ratios between G and D bands for various polymer precursors.....	100
Figure 5.14: High resolution C1s and O1s spectra of polyethylene derived carbon.	103
Figure 5.15: High resolution C1s and O1s spectra of polypropylene derived carbon.....	104
Figure 5.16: High resolution C1s and O1s spectra of polyethylene terephthalate derived carbon.	105
Figure 5.17: High resolution C1s and O1s spectra of polystyrene derived carbon.	106
Figure 5.18: High resolution C1s and O1s spectra of polyacrylonitrile derived carbon.....	107
Figure 6.1: An example of homolytic fission followed by carbocation rearrangement forming cyclic rings.	110
Figure 6.2: A photo of polymer condensation in the furnace exhaust (part number 2 in Figure 4.1)	111
Figure 6.3: Colours of various metal oxide/waste plastic composites.....	112
Figure 6.4: FTIR of polyethylene waste plastic, and its zeolite composite, silica composite, and alumina composite (top to bottom).	113
Figure 6.5: FTIR of polyethylene terephthalate waste plastic, and its zeolite composite, silica composite, and alumina composite (top to bottom).	114

Figure 6.6: FTIR of polypropylene zeolite composite, silica composite, alumina composite, and waste plastic (top to bottom).	115
Figure 6.7: BET isotherm plots of metal oxide additives.	117
Figure 6.8: XRD of metal oxide additives.	118
Figure 6.9: Nitrogen TGA of polyethylene and its metal oxide composites.	119
Figure 6.10: Nitrogen TGA of polypropylene and its metal oxide composites.	120
Figure 6.11: Nitrogen TGA of polyethylene terephthalate and its metal oxide composites.	121
Figure 6.12: XRD of carbonaceous products derived from modified polyethylene precursors.	123
Figure 6.13: XRD of carbonaceous products derived from modified polypropylene precursors.	124
Figure 6.14: XRD of carbonaceous products derived from modified polyethylene terephthalate precursors.	125
Figure 6.15: A chart of deconvoluted intensity ratios between G and D bands for various polymer precursors.	126
Figure 6.16: A schematic of Raman vibrational modes of graphene responsible for the D band.	128
Figure 6.17: Raman spectra for polyethylene derived POGC modified with (top to bottom) alumina, silica, and zeolite.	130
Figure 6.18: Raman spectra for polypropylene derived POGC modified with (top to bottom) alumina, silica, and zeolite.	133
Figure 6.19: A schematic of Raman vibrational modes of graphene responsible for the G band.	134
Figure 6.20: Raman spectra for polyethylene terephthalate derived POGC modified with (top to bottom) alumina, silica, and zeolite.	136
Figure 6.21: High resolution C1s and O1s spectra of polyethylene-alumina derived carbon.	140
Figure 6.22: High resolution C1s and O1s spectra of polyethylene-silica derived carbon.	141
Figure 6.23: High resolution C1s and O1s spectra of polyethylene-zeolite derived carbon.	141
Figure 6.24: High resolution C1s and O1s spectra of polypropylene-alumina derived carbon.	142
Figure 6.25: High resolution C1s and O1s spectra of polypropylene-silica derived carbon.	143

Figure 6.26: High resolution C1s and O1s spectra of polypropylene-zeolite derived carbon.	143
Figure 6.27: High resolution C1s and O1s spectra of polyethylene terephthalate-alumina derived carbon.	144
Figure 6.28: High resolution C1s and O1s spectra of polyethylene terephthalate-silica derived carbon.	145
Figure 6.29: High resolution C1s and O1s spectra of polyethylene terephthalate-zeolite derived carbon.	145

Tables

Table 2.1: Carbon content of various common polymers.....	23
Table 2.2: The lifespan and recovery rate of common plastics ^{1,31}	25
Table 2.3: Summery of products of pyrolysis of municipal waste polymers at various temperatures ^{34, 35}	26
Table 2.4: A comparison of the electrical properties of various carbonaceous materials and their synthetic methods.....	31
Table 2.5: A summary of bond characteristics for those commonly present in plastics.	32
Table 2.6: A comparison of carbonisation temperatures for various polymers.	33
Table 2.7: Properties of various gallium based liquid metal alloys ⁸²	44
Table 2.8: Experimentally determined solubility of common catalytic additives in gallium ¹²¹	50
Table 5.1: A summary of the decomposition mechanisms and products of PE, PP, PS, PET, PAN, and nylon 6/6 from literature, and a brief description of results from this work.....	87
Table 5.2: Average EDX analysis of carbon samples from various waste plastics.	92
Table 5.3: Summary of peak assignments for amorphous carbon chars ¹⁴²	93
Table 5.4: A summary of R ² values of Raman curve fitting from Figure 5.11.	95
Table 5.5: Atomic percentages of surface oxygen from various plastic derived carbons as determined by XPS wide scan.....	101
Table 6.1: Summary of BET results of metal oxides.	116
Table 6.2: A summary of R ² values of Raman curve fitting from metal oxide modified carbon samples.	127
Table 6.3: Atomic percentages of surface oxygen from various modified plastic derived carbons as determined by XPS wide scan.....	138

Equations

$2Al(S) + 6H_2O(l) \rightarrow 2Al(OH)_3(aq) + 3H_2(g)$ Equation 1	48
$\eta D \propto kTa$ Equation 2	50
$\gamma \Delta \cos \theta = cV^2$ Equation 3	51

Abbreviations

SEM	Scanning Electron Microscopy
EDX	Energy Dispersive X-Ray analysis
XRD	X-Ray Diffraction
FTIR	Fourier-Transform Infrared Spectroscopy
UV-Vis	UV-Visible spectroscopy
TGA	Thermogravimetric analysis
XPS	X-Ray photoelectron spectroscopy
BET	Brunauer–Emmett–Teller nitrogen adsorption analysis
PE	Polyethylene
PP	Polypropylene
PET	Polyethylene Terephthalate
PS	Polystyrene
PAN	Polyacrylonitrile
LM	Liquid metal
EGaIn	Eutectic Gallium-Indium
EBiSn	Eutectic Bismuth-Tin
CNM	Carbon Nanomaterial
PEDC	Polyethylene Derived Carbon
PPDC	Polypropylene Derived Carbon
PETDC	Polyethylene Terephthalate Derived Carbon
PSDC	Polystyrene Derived Carbon
PANDC	Polyacrylonitrile Derived Carbon
PE-AIDC	Polyethylene-Alumina Composite Derived Carbon
PE-SiDC	Polyethylene-Silica Composite Derived Carbon
PE-ZeDC	Polyethylene-Zeolite Composite Derived Carbon
PP-AIDC	Polypropylene-Alumina Composite Derived Carbon
PP-SiDC	Polypropylene-Silica Composite Derived Carbon
PP-ZeDC	Polypropylene-Zeolite Composite Derived Carbon
PET-AIDC	Polyethylene Terephthalate-Alumina Composite Derived Carbon
PET-SiDC	Polyethylene Terephthalate-Silica Composite Derived Carbon
PET-ZeDC	Polyethylene Terephthalate-Zeolite Composite Derived Carbon
wt%	Weight %

Chapter 1: Introduction

1.1: Overview

Our planet is dying. Waste plastic is a growing problem that has significant and lasting environmental consequences. Plastic production and use have increased rapidly in recent decades, leading to increasing amounts of plastic waste in landfills, oceans, and other environments. The accumulation of plastic waste not only affects the quality of life for wildlife and human communities, but also contributes to the loss of biodiversity and the degradation of ecosystems. Moreover, the persistence of plastic waste in the environment for centuries to millennia means that the problem will exist for generations to come.

One of the key challenges in addressing the plastic waste crisis is the limited effectiveness of current recycling techniques. While recycling is highly touted amongst plastic producers and policy makers, anthropogenic polymer waste remains a problem without a solution. Despite the widespread availability of recycling programs, only a small fraction of plastic waste is recycled. This is due, in part, to the lack of effective methods for collecting, sorting, and recycling plastic waste, as well as the limited market for recycled plastic products. As a result, primary and secondary recycling techniques are ultimately a cradle-to-grave approach to the issue. All the while, these methods are being flaunted as a way to justify individual consumption and assuage the guilt of consumers as the problem continues to get worse. Additionally, many plastic products are not recyclable or are too difficult or expensive to recycle, which further exacerbates the waste problem.

To find a solution to the plastic waste crisis, it is essential to understand the problems with waste plastic and current recycling techniques, as well as the opportunities and challenges for promoting sustainable plastic use and waste management. Such a solution would encompass several factors. Firstly, it would sequester contaminants from entering our environment entirely. Secondly, it would be cradle-to-cradle in its approach to ensure that the non-renewable resources being consumed aren't being wasted. Thirdly, it would be economically viable so that the process could be self-sustaining. Tertiary recycling, or chemical recycling, is a process by which plastic waste is broken down into fundamental molecular or atomic components to be reused as a starting material to make new things from. This can be depolymerisation where monomers have been regenerated and can be used to create new plastics, or they can recover the constituent atoms of the polymer to produce functional, positive value materials. Many such tertiary recycling methods have been demonstrated in

literature; however, they have thus far failed to surpass pilot plant scale as a result of missing one of the factors outlined above.

This work proposes a novel low temperature tertiary recycling method using a liquid metal reaction medium to create amorphous carbonaceous materials such as carbon black from waste polymer. Literature has reported liquid metals achieving low temperature carbonisation of carbonaceous gasses, as well as strong reductive properties towards other gasses such as nitrogen. The novelty of this work presents a unique methodology in application to solids, as well as a application to larger macromolecules such as polymers. This method meets the criteria outlined above, being able to sequester waste plastic from the environment by transforming it into a high value material used in many industrial applications. It is cradle-to-cradle in its approach as it transforms the waste plastic into a pristine new material. Finally, when taking into account the negative value of plastic waste, and the low energy requirements of this product, it is hopeful that this method could be economically viable.

1.2: Structure of the thesis

This work begins by assessing the issue through exploring the current state of waste plastic and recycling, identifying the barriers to waste reduction and recycling, and developing innovative solutions for reducing plastic waste and promoting recycling. The literature review focuses on several key areas, including the life cycle of plastic waste, the economic and environmental impact of plastic waste, and the barriers to plastic waste reduction and recycling. Through an exhaustive review of existing literature, this work aims to provide a comprehensive understanding of the problems with waste plastic and current recycling techniques, and to identify opportunities for waste reduction and recycling. Next, a novel angle for recycling is considered and the properties and benefits of liquid metals are outlined.

Following that, the design and optimisation of a custom reactor is discussed, alongside the selection ethos of the liquid metal alloy used. The carbonaceous products of various waste plastics are characterised and compared. Then, this work looks to methods of improving the reaction rates and product consistency of this process through precursor modification. Finally, conclusions are drawn, and speculation towards future experimental modifications are given.

Overall, this work aims to provide a comprehensive and innovative understanding of the problems with waste plastic and current recycling techniques, and to outline a new and

improved method for reducing plastic waste. The research will contribute to the development of a more sustainable future by advancing our understanding of the plastic waste crisis and by providing a unique, cradle-to-cradle solution for reducing plastic waste and promoting recycling.

Chapter 2: Literature review

2.1: Introduction

Currently, almost all widely deployed approaches to recycling are cradle-to-grave, where the products of each subsequent processing represent a value-lost over that of their virgin precursors. As such, via current recycling techniques, all recyclables eventually reach a point at which they are no longer reclaimable. After this point, they will inevitably make their way to landfill, or into the environment. These approaches are known as primary and secondary recycling¹. This is outlined graphically in Figure 2.1.

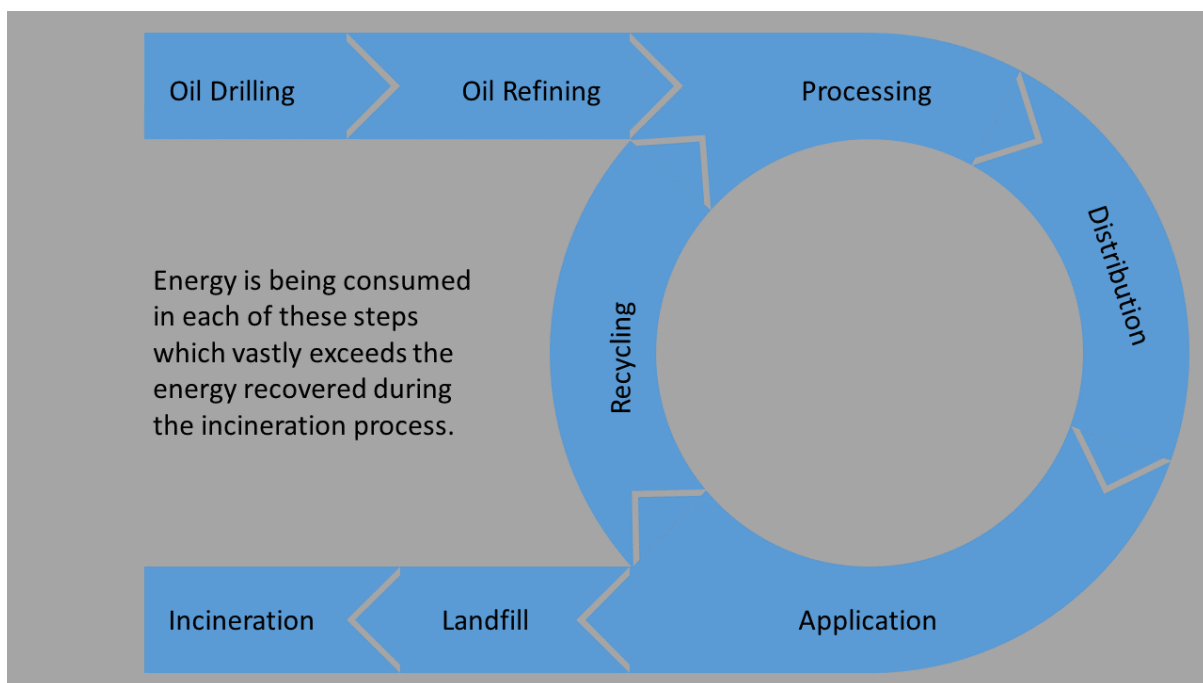


Figure 2.1: The Plastic Cycle.

To be truly sustainable, a cradle-to-cradle approach must be found. This is one where the products of the process are value-added, or at minimum value-neutral, when compared to their virgin precursors. Additionally, this approach must be part of a cycle which is infinitely repeatable with little or no material going to waste².

Potential methods of achieving this have been well documented in literature. These range from the production of pyrolysis oils for use as fuels³, to that of partial coke substitutes used in the manufacture of steel⁴ and the manufacture of conductive, paramagnetic carbon microspheres⁵. These approaches are known as tertiary recycling, or chemical recycling. They involve the use of waste as a raw material for the generation of new materials, whose purposes are completely different to that of their starting materials¹. As a result, tertiary

recycling methods offer high potential to achieve the above goal of being cradle-to-cradle processes.

In practice however, these processes have proven to be expensive⁶ and, as a result, the value of a product produced via tertiary recycling must offset its manufacturing cost for it to hope to be markedly viable. Many tertiary recycling methods for synthetic polymer recycling have been demonstrated in literature going back around fifty years⁷. Most polymers are produced from fossil fuel precursors, and some of the earliest methods of the tertiary recycling of polymers demonstrated the ability to reverse this process, turning polymers back into their fuel precursors^{3, 8}. However, despite much research, and advancements in methodologies and catalysts, this technique has repeatedly proven to be economically unviable as the fuel produced has never been competitive with traditional fuel sources. Additionally, fossil fuels do not represent a true cradle-to-cradle technique because of their single use nature. Additionally, with future energy production looking to trend away from the use of fossil fuels, this method may already be antiquated and unviable⁹.

Carbon nanomaterials (CNMs) have been the focus of a large amount of research, particularly over the past two decades¹⁰⁻¹³ due, in part, to their notable collection of mechanical, electrical and optical properties. CNM's generally consist of a zero, one or two dimensional hexagonal lattice of sp² hybridized atomic carbon¹⁴. The most well-known example of CNMs is that of graphene, a two-dimensional hexagonal lattice of sp² hybridized carbon atoms. However, due to the complexities of their manufacture, the cost of CNMs has been prohibitively expensive, which has kept their application outside of a laboratory setting largely theoretical. An element of this cost is the requirement for expensive pure and precursor materials, usually consisting of some sort of highly homogenous source of carbon containing molecule¹⁵.

Recent research has focused on the possibility of replacing these expensive, pure, homogenous precursor materials with more economically viable options. One potential replacement which has been considered is waste polymers. Biological polymers, such as cellulose containing wastes, were some of the first to start receiving attention in this space^{16, 17}. These wastes are produced in abundance in the agricultural sector and are carbon rich¹⁸, which presents an intriguing option for sourcing precursor materials for CNM synthesis¹⁹.

In addition, waste plastics have started to receive similar attention^{12, 20, 21} as they are abundant, carbon rich (shown in Table 2.1) and represent a negative value commodity¹; that is, one that costs money to dispose of. Furthermore, their processing during the CNM synthesis can also result in useful by-products. Examples include pyrolysis oils¹, which could be used to fuel syntheses, and elements, such as nitrogen, which can be incorporated into the structure of the CNMs to enhance their properties^{22, 23}. In addition to lowering cost, the environmental effect of repurposing these waste polymers should not be understated. In this review, we will look at the current state of carbon nanomaterial synthesis using waste polymers as precursors and apply lessons learned from more traditional CNM syntheses to help understand and streamline future methodologies.

Table 2.1: Carbon content of various common polymers

Polymer	Molecular formula of monomer	Carbon Content (wt %)
Polyethylene (PE)	$(C_2H_4)_n$	85.6
Polyethylene terephthalate (PET)	$(C_{10}H_8O_4)_n$	62.6
Polypropylene (PP)	$(C_3H_6)_n$	85.6
Polystyrene (PS)	$(C_8H_8)_n$	92.2
Polyurethane (PU)	$(C_{15}H_{16}N_2O_4)_n$	62.5

2.1.1.1: Current recycling techniques

Currently, we primarily employ three main types of recycling for plastics, primary secondary and tertiary¹. Primary recycling involves taking pristine, uncontaminated, first use waste plastic and turning it back into the original product. This is known as closed loop recycling and is limited by its requirement of near-pristine, uncontaminated starting materials. However, because of these limitations, the products of primary recycling are the most valuable and functional relative to their source material²⁴. This type of recycling is seen widely in the production of recycled PET water bottles for example.

Secondary recycling is similar to primary recycling, though the produced material is used for the manufacture of products different to that of the source material. Both of these processes involve mechanical grinding, washing and extruding waste plastics to form pellets of recycled plastic which can then be used to create new products. This type of recycling concerns mostly the processing of first-use consumer materials, but due to the degradation of the plastic after each process cycle, the resultant product is mechanically inferior¹. This inferiority is the result

of the degradation of polymer chain lengths, and the effect of the thermal treatment processes on their intermolecular interactions. As a result, recycled polymers may be more brittle, weaker, less chemically resistant, or any combination thereof. As a result, the value of the recycled product decreases after each processing cycle until it reaches a point where primary and secondary recycling are no-longer viable as the resulting product is no longer usable. In addition, these recycling techniques require a very homogenous source of polymer for the feedstock as contaminations in the feedstock can drastically reduce the quality of the subsequent product. As a result, unsustainable amounts of energy and time are required for sorting recyclables for this method of recycling¹.

Finally, energy recovery involves the combustion of polymer waste to recover the energy in its bonds in the form of heat. This is a process which almost all polymer waste eventually goes through once primary and secondary are no longer viable. This process is favourable to leaving waste in landfill because it involves some form of energy recovery and prevents solid waste entering the environment. However, it results in large amounts of greenhouse and toxic gases being produced^{7, 25} and released into the atmosphere, contributing to global warming²⁶. Overall, existing widely employed methods of recycling can be described as cradle-to-grave. With the extensive resources consumed in the process of making these goods at every step, they do not constitute sustainable practice.

Furthermore, while some of this waste is recycled, the vast majority is not. The European Union is the world leader when it comes to recycling plastics at only 39%²⁷. Other countries, like the United States of America, only recycle 9% of their waste plastics²⁸. What cannot be recycled makes its way into landfills, or into the environment. Once in the environment, plastic wastes cause two main problems for wildlife, relating to microplastics, and microplastics. Microplastics have a tendency to harm wildlife directly, by either internal choking, or external strangulation. Microplastics on the other hand are unwittingly eaten by animals lower on the food chain. From there, they biomagnify up the food chain, which causes issues for apex predators, as well as bioaccumulate which is problematic for all wildlife. This issue is amplified because of the environmental persistence of plastics. As shown in Table 2.2 some plastics have been estimated to persist in the environment for hundreds of years^{29, 30}.

Table 2.2: The lifespan and recovery rate of common plastics^{1, 31}.

Polymer	Environmental Persistence (Years)	Recovery Rate
Polyethylene Terephthalate (PET)	450	19.5%
High-density Polyethylene (HDPE)	450	10%
Polyvinyl Chloride (PVC)	600	0%
Polystyrene (PS)	50	1%

2.1.2: Tertiary recycling

Historically, tertiary, or chemical recycling of polymers has focused on the recovery of petrochemical components from waste polymers. It has been known for decades that polymers can be converted into fuel using pyrolysis. Matsumoto et al. began investigating the viability of the production of hydrocarbon fuels from the pyrolysis of plastics and even set up pilot plants as early as 1975³. As part of preliminary research, they found that the percentage yield of solid, liquid and gaseous components from pyrolysis were highly dependent on the operating temperature, heating parameters and retention time at which the waste was being treated. The investigation found that gaseous yields increased continuously with temperature in the ranges studied, up to 1000 °C. The liquid yield increased to a maximum of approximately 45% at 450 °C, then decreased with any additional increase in temperature. Finally, while the goal was to optimise for liquid yields, they did find that solid yields increased to a maximum of 20% at 1000 °C but were also found to increase with longer dwell times. After preliminary studies, two pilot plants were set up. After one month of operation, it was concluded that, for the process to be economically viable, pyrolysis plants would need to process 50 tonnes per day of municipal waste.

Sharuddin et al. assembled a comprehensive review the pyrolysis of the various types of common municipal waste polymers, both homogenous and comingled samples, and the effect of different parameters on each³². There has been a past tendency to focus on the production of liquid and gaseous components. As a result, this review is again from the perspective of evaluating the viability of creating a usable fuel source. It reaches similar conclusions to those of Matsumoto et al. They provide a summary of twenty-seven studies, the parameters used to maximise liquid yields, the types of reactors used and the yields. In general, liquid yields are optimised between 400 and 500 °C. However, with the advances in

catalyst design, yields are commonly seen in the 70 to 90% range³², with one study³³ giving a liquid yield of 97% under elevated pressure of 15.8 atm using a polystyrene feedstock.

Particularly notable is a kinetics study which looked at the vacuum pyrolysis of polyvinyl chloride. The study found that PVC decomposition occurred over three stages. The kinetics model proposed three reactions taking place at each of those stages, resulting in various sample mass loss. Their findings are summarised in Table 2.3 below.

Table 2.3: Summary of products of pyrolysis of municipal waste polymers at various temperatures^{34, 35}.

Temperature holds	280°C	320°C	520°C	End
Weight loss	48.75%	15.08%	27.64%	91.47%
HCl	46.16%	11.95%	0.25%	-
Liquid hydrocarbons	2.59%	3.45%	-	-
Gaseous hydrocarbons	-	-	27.39%	-
Solid ash	-	-	-	8.53%

This is notable because the solid fraction produced under vacuum pyrolysis is substantially higher than those of reactions taking place at atmosphere or elevated pressures.

In a further study of the synergistic effects of co-pyrolysis, Miranda et al. expanded the above work to include PS, PP, HDPE and LDPE and various combinations of the four³⁵. In this study, it was found that some interactions occurred between plastics during vacuum pyrolysis. This did not however represent a significant change in the activation energy, which only exhibited an $\sim\pm 13$ kJ mol⁻¹ difference between single polymer pyrolysis and mixtures. Therefore, it was concluded that the degree of interactions mainly depended on the cracking process and the reactivity of intermediary products released. As a result of this, the most significant interactions were seen when PVC was reacted in conjunction with other polymers. This was attributed to the reactivity of Cl radicals, most commonly hydrogen abstraction and promoted the low temperature formation of lighter hydrocarbon fractions³⁵.

A study by Jung et al. corroborates these findings in that the yields of solid increases both with high temperatures and longer dwell times³⁶. In addition, the study reported that the

yield of char also increased at lower temperatures using longer dwell times. Sharuddin et al. concluded that, given the negative value of the waste used as a source, with the appropriate catalysts and parameter optimisation, pyrolysis could provide an economically viable and sustainable method of generating fuel from waste polymers³².

However, economically viable or not, the conversion of polymers to fuel does not adequately tackle the wider problem in a sustainable manner. This is because the process of converting waste polymers to fuels is still a cradle-to-grave process. As eluded to previously, once the fuel has been used there can no longer be any recovery of components as they have been released into the atmosphere, predominantly as carbon dioxide, contributing to global warming²⁶. For a truly sustainable, long-term solution, the process must be cradle-to-cradle. One which does not ultimately result in the production of greenhouse gases, but instead sequesters and fixes the carbon into highly valuable, long-life products.

Figure 2.2 shows a breakdown of commonly polymers in Australia, their uses, and their recycling status. At present, this plastic waste which has passed its maximum number of recycling cycles is a negative value commodity. This loss of value is attributed to its limited usefulness and the cost required to dispose of it in landfill. As a result, the processing of this material can be seen a dual income stream as a facility would not only be receiving payment for its product but also for taking the waste in the first place. This would help to offset cost the processing itself. In addition, processing involving pyrolysis could utilise pyrolysis oils and gases, produced as a by-product of the carbonization, as fuel, further lowering the cost³⁷.

Pictogram	Polymer name and abbreviation	Uses	Recycling status in Australia
	<u>Polyethelene</u> terephthalate (PET)	Drink bottles and single use containers, as well as <u>polyesther</u> fibres.	✓
	High-density polyethylene (HDPE)	Single use containers, cutlery, and cups, bags, and storage containers.	✓
	Polyvinyl chloride (PVC or V)	Plumbing, siding, fencing and other outdoor or high wear environments.	✓
	Low-density polyethylene (LDPE)	Plastic bags, flexible tubing, and general applications where flexibility is required.	✗
	Polypropylene (PP)	Shells for electronics, car parts, and containers.	✓
	Polystyrene (PS)	Insulation, and hot beverage cups, as well as anything where insulation is required.	✗
	Others; acrylics, polyamides, etc.	Various.	?

Figure 2.2: Infographic showing resin code pictograms and their recycling status in Australia.

2.1.3: Waste plastics as a material source

Owing to their carbon backbone, the primary mass of polymers is made up by carbon atoms. Therefore, the solution to this recycling problem is going to be one which utilises that carbon in a manner which is both useful, valuable and environmentally sustainable³⁸. Carbon chemistry is very diverse owing to the carbon atom's electronic structure. Many valuable allotropes exist and have been extensively studied. Carbon allotropes are best characterised with Raman spectroscopy and their structure is shown by the ratio between D-band and G-band intensity. Larger G-band intensities are the result of more in-plane vibrations of sp² bonded carbon atoms, and lower D-band intensities represent the lack of out of plane vibrations. The higher this ratio, the longer the range of crystallinity and vice versa³⁹.

As outlined in the previous chapters, many carbon allotropes possess impressive electrical properties, and as a result, there is great interest in their electrical applications. Furthermore, it is possible for the electrical properties of these materials to be enhanced by doping. A very common doping agent for enhancing the electrical properties of graphitic carbon lattices is nitrogen. Several studies have produced CNMs with impressive electrical properties from a

variety of carbonaceous sources, including organic wastes. A summary can be seen in Table 2.4.

In a very comprehensive study, Wiggins-Camacho and Stevenson⁴⁰ investigated the effect of nitrogen concentration on the capacitance and electronic conductivity of carbon nanotube (CNT) electrodes. In their work, they showed that a nitrogen content of 4% by number of atoms gave a maximum conductivity of $416 \pm 80 \Omega^{-1} \text{cm}^{-1}$, compared to $333 \pm 77 \Omega^{-1} \text{cm}^{-1}$ for a pure CNT electrode. They also noted a positive relationship between CNT length and conductivity as well as a negative parabolic relationship between conductivity and roughness factor (a ratio between electrochemical surface area, and the geometric surface area). The study concluded that the change in conductivity due to nitrogen doping was largely junction dominated. It also determined that both compositional and morphological factors were at play in influencing the conductivity of carbon nanotubes⁴⁰.

Similarly, Jeong et al.²³ investigated the effects of the nitrogen doping of graphene for applications in electrodes. Similar to the findings of Wiggins-Camacho and Stevenson, the investigation found that introducing around 2% nitrogen to the graphitic structure resulted in increased specific capacitance of 280 F g^{-1} . This is approximately four times higher than that of pristine graphene. The study also found that this process is largely junction dominated occurring at the graphene basal planes. They propose that this increase in capacitance is the result of increased binding energy and thus a greater interaction with ions in the electrolyte. However, it was noted that there is a balance required, as increasing binding energy too high will make the binding process difficult to reverse, thus decreasing the capacitance²³. This phenomenon would explain the capacitance decrease seen in Wiggins-Camacho and Stevenson's work beyond 4% nitrogen content.

Given the usefulness of nitrogen doping in increasing the capacitance of graphitic carbon lattices, it stands to reason that nitrogen containing polymers such as polyurethane and polyimides would be an excellent addition to the proposed process of material recovery from waste polymers. Jin et al.²² demonstrated a similar concept using dried distillers grains with solubles (DDGS), a nitrogen containing waste biomass product from the production of alcohol. They found that by carbonizing DDGS at high temperatures under inert atmosphere, they were able to produce nitrogen doped graphene with specific capacitance of 324 F g^{-1} . Both the works from Jeong et al., Jin et al. determined that the mechanism of this increase is the

result of nitrogen binding to the graphene basal plane, enhancing the materials binding energy^{22,23}. The structural arrangement of this can be seen in Figure 2.3.

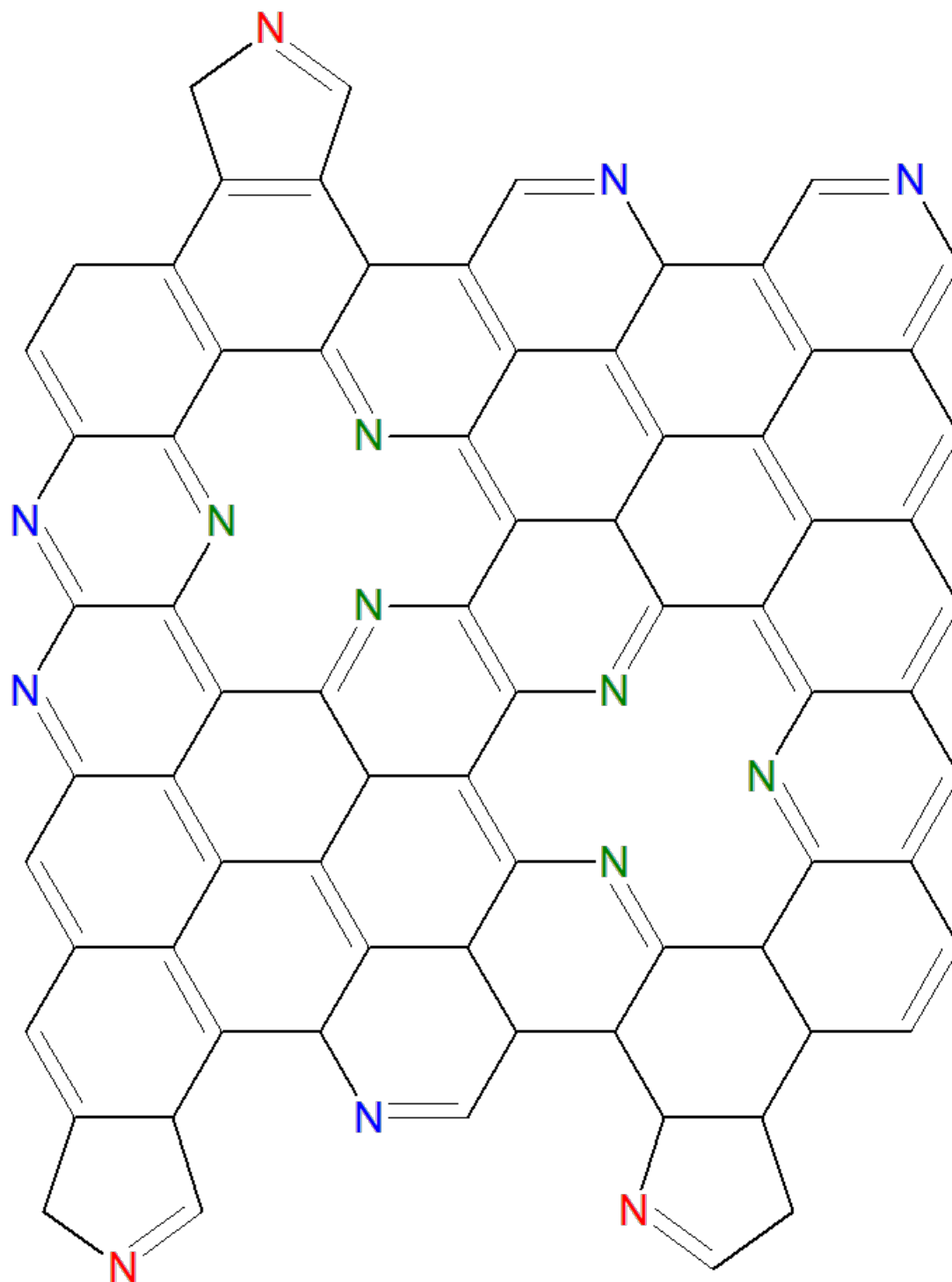


Figure 2.3: A diagram of the schematic structure of N-graphene. Pyrrolic nitrogen shown in red, pyridinic nitrogen shown in blue and internal pyridinic nitrogen shown in green.

Table 2.4: A comparison of the electrical properties of various carbonaceous materials and their synthetic methods.

Electrode	Method of Synthesis	Material Source	Catalyst	Specific Capacitance	Conductivity	Reference
Graphene	Modified Hummers Method	Graphite	None	135 F g ⁻¹	200 Ω ⁻¹ m ⁻¹	11
N-Graphene	Inert atmosphere carbonization of thin-films	Chitosan	None	-	220 Ω ⁻¹ m ⁻¹	41
N-Graphene	Graphitized activation @700°C	Distillers Dried Grain w/ solubles	-	324 F g ⁻¹	-	22
SWCNT	Arc Discharge	Graphite	Nickel	180 F g ⁻¹	-	42
CMS	Pyrolysis in sealed chamber	Various synthetic polymers	None	-	45 S m ⁻¹	5
N-CB	Pyrolysis in sealed chamber, followed by KOH activation	Distillers Dried Grain w/ solubles	Electrolyte: KOH	150 F g ⁻¹	-	17
CB	Pyrolysis	Peach stones	Electrolyte: KOH	267 F g ⁻¹	-	43

2.2: Carbonisation

Carbonisation typically refers a heat treatment process by which organic materials are converted to solid carbon by the breaking of their bonds. This is typically a highly endothermic reaction, requiring high energy input to achieve. Bond dissociation energies of those commonly found in plastics, as well as other bond characteristics are summarised below in Table 2.5. These solid carbons may be amorphous, or graphic as is discussed later in this review. This process can occur under anoxic or oxidative atmospheres, in the absence, or presence of a catalyst, and under atmospheric, or high pressures⁴⁴. When relating to plastics, the carbonization process, and pyrolysis are often difficult to distinguish, and frequently the terms are used interchangeably⁴⁵.

Table 2.5: A summary of bond characteristics for those commonly present in plastics.

Bond type	Bond length (Å) ⁴⁶	Bond dissociation energy (kJ mol ⁻¹) ⁴⁷	Electronegativity difference ⁴⁸
C-C	1.55	607.0	0.000
C-H	1.08	337.2	0.244
C=C	1.34	682.0	0.000
C=O	1.22	749.0	1.066
C-O	1.42	358.0	1.066
C-N	1.47	174.9	0.512
N-H	0.99	314.0	0.766
C≡N	1.16	937.0	0.512

For the purposes of this review, as it relates to liquid metal (LM) catalysts, it will focus on anoxic carbonisation. Anoxic carbonisation refers to carbonisation occurring in a non-oxidative atmosphere under approximately atmospheric pressure. The mechanism of this process is extremely complex, and still not fully understood⁴⁹. For example, the initial decomposition of polyesters is thought to typically start with polymer chain scission through a 6-member aromatic heterolytic transition phase, followed by secondary reactions involving the formation of vinyl ester chains and leading to cross linked olefin structures and light weight volatile products. Kinetic models have shown that this process can range in activations

substantially, between 100 and 250 kJ/mol⁴⁹. While complicated and highly varied, the process generally involves aromatisation, followed by removal of various other elements present, like hydrogen, oxygen and nitrogen⁵⁰. This results in by products such as steam, carbon monoxide, carbon dioxide, hydrogen, methane, and ammonia⁴⁴. This is further discussed Chapter 5. As a result of the endothermic nature of this process, pyrolysis temperatures are generally extremely high, as summarised in Table 2.6. As such, energy requirements are typically too high to make practical use of this process.

Table 2.6: A comparison of carbonisation temperatures for various polymers.

Polymer	Temperature of Pyrolysis	Methodology	Product	Reference
Polyethylene	1800 °C	Pyrolysis of thin-films under Ar.	Graphitic carbon	51
Polyethylene Terephthalate	700 °C	Pyrolysis of waste PET under Ar.	Porous carbons	52
Polystyrene	700 °C	Pyrolysis of PS nanospheres under N ₂ .	Monodispersed N-doped carbon nanospheres	53
Polyacrylonitrile	1000 °C	Pyrolysis of PAN thin films under nitrogen.	Carbon paper	54
Nylon 66	1000 °C	Pyrolysis of nylon 66 fibres under A2.	Carbon fibres	55
Comingled PP, PE, PS, PET, & PVC	700 °C	OOMT modified assisted pyrolysis of comingled polymers under Ar.	Porous carbon nanosheets	56
Melamine-formaldehyde resin	700-1800 °C	Pyrolysis of melamine foam under nitrogen.	Elastic carbon foam	57
NUT-2	600 °C	Pyrolysis of NUT-2 polymer under N ₂ .	N-doped porous carbons	58
Polyethylene Terephthalate	600 °C	Pyrolysis of waste PET under N ₂ .	Activated carbon.	59

2.2.1: Zero-dimensional carbons

Carbon dots or carbon nanospheres, are examples of zero-dimensional arrangement carbon. Zero-dimensional arrangements of carbon are perhaps the most diverse and tuneable. Some have demonstrated desirable optical, electronic and photoelectric properties which, unlike with graphene and CNTs, are largely determined by their crystallographic orientation of edge structures¹³. Others have been synthesised with extremely high surface area for enhanced adsorption and energy storage properties⁶⁰. They have also been produced with magnetic properties of targeted pollutant adsorption⁶¹ and catalytic properties⁶².

Their morphology and properties can vary greatly, depending on application, synthesis method and precursor materials. In terms of describing their morphology, they can be hollow⁶⁰ or solid⁵, and can vary in size from a few nanometres¹³ up into the micrometre range⁵. Indeed, their only tangible defining morphological traits are that they consist primarily of sp² hybridized carbon and form a spherical shape.

Their production from a waste polymer source has been well documented in literature. In a 2010 study, researchers published a methodology for the conversion of comingled polymer waste into paramagnetic, conductive solid carbon microspheres⁵. The study provides a breakdown of the morphology difference as a result of varying polymer feedstock as well as synergistic effects of co-pyrolysis with multiple polymers. The reactions took place in a sealed vessel under autogenous atmosphere at 700°C. The products of the reaction were found to be exceptionally hard as a result of sp² and sp³ bonding of carbon atoms within the spheres. Additionally, the study measured the conductivity of individual carbon spheres using a two-point nanoprobe, finding it to be 45 Sm⁻¹. Finally, as a result of their unpaired electron spin, the synthesised particles exhibited paramagnetic properties. As a result, they exhibited standard paramagnetic properties, such as a positive magnetic susceptibility.

In a similar vein, but using a very different methodology, Mohsenian et al. produced hydrogen rich gases by way of thermal plasma pyrolysis of various polymers, such as PP, PE, PVC and ABS⁶³. Of particular note was a by-product of carbon nanospheres which were found in a follow up study looking into the solid products of this process using ABS. The reactions took place in an oxygen free thermal plasma pyrolysis reactor at arc currents of 80, 100, 120 and 140 A. The investigation found that above an arc current of 100 A, the carbon nanospheres produced contained no significant impurities of either contaminants or other forms of carbon.

This results in the post processing of the products being significantly simpler. This is attributed to the lack of oxygen in the reaction chamber, resulting in a distinct lack of CO and other ash components. As a consequence, this process shows significant prospect in terms of product output due to the nature of the fractions being produced. The study cites the potential application of this product being similar to that of carbon black, in applications like tyre production. However, there may be further applications in other areas based on properties like conductivity, surface area and optical properties⁶³. A production of hydrogen gas as a by-product of carbon nanosphere production, coupled with the negative-value of the feedstock may significantly help offset the processing costs. The main significant issue with this method however is the scalability of such a process as a result of the plasma reactor.

While the study discussed above suggests application in the production of tires, a study by Maroufi et al. proposes the reverse by turning waste tyre rubber into zero dimensional carbons using a rapid, ultrahigh temperature approach. In their work, waste tyre rubber was carbonised at 1550 °C inside a horizontal tube furnace under argon purge by exposing it to the heat for 5 seconds. The resulting char was then milled and pressed into briquettes, where it was again carbonised over times ranging from 5 seconds to 20 minutes. XPS revealed the complete removal of oxygen and the presence of primarily C-C bonds after 20 minutes of exposure, while XRD showed the presence of graphitic carbon. Additionally, surface area increases were seen with increasing dwell times up to 117.7 m²g⁻¹. This was attributed to the removal of oxygen groups in the form of CO₂ and the subsequent corrosion of the nanospheres by CO₂ to CO according to Boudouard reaction which increased the porosity of the nanospheres⁶³. Again, conductivity of these products were not measured. However, as a result of the relatively high surface area and the graphitic network present, it stands to reason that these particles may have electrical applications. Also of note, the method described is easily scalable lending to an industrially viable methodology. However, the reaction temperatures of 1550 °C are a significant barrier in the method being economically viable. The energy costs would need to be offset with an extremely high material value.

Another method commonly employed to restore a graphitic network to amorphous carbon is chemical vapour deposition. Tripathi et al. employed a CVD method to convert PP into solid, hollow and nitrogen doped carbon nanospheres⁶⁴. For solid carbon nanosphere production, waste PP was placed inside a quartz reactor inside a two-stage heating chamber, one at 500°C

and the other at 900°C. The quartz reactor was heated in the first stage, before being moved to the second stage for an hour and then left to cool naturally inside the apparatus. Hollow nanospheres were produced in the same way, but using a silica template, and nitrogen doped spheres used melamine as a nitrogen source. Silica templates were removed with HF treatment. The two-stage heating was required to convert the solid PP into a gas before being introduced to the second stage heating. Raman spectroscopy revealed all three class of products to largely consist of graphitic carbon. XPS revealed them to be largely pure and free of contaminants that may be present from the use of catalysts⁶⁴. The investigation suggests the typical applications of these forms of carbon, however many of their properties outside their morphology were not characterised. While interesting from the perspective of the tunability of the products, the same drawbacks of CVD remain; primarily its scalability and cost. However, the production of nitrogen doped hollow nanospheres lends the possibility of sourcing the nitrogen directly from nitrogen containing polymers, similar to the graphene synthesis method of Primo et al.⁴¹.

The growth mechanism of these carbon nanospheres was proposed in a study by Gong et al.⁶⁵. They synthesised hollow carbon nanospheres through thermal carbonization of PS using a cocatalyst of organically modified montmorillonite and cobalt at 700 °C with 5 minutes of exposure in an inert atmosphere. The resulting char was treated with HF and nitric acid to remove the catalysts and amorphous carbon. The resulting products demonstrated high surface areas of up to 227.3 m²g⁻¹ and yields of up to 10 wt.%. As a result of the acid cleaning, the products proved highly pure, with ordered graphitic networks. The proposed mechanism of action put forward was similar to that of other, similarly produced CNM's; a three step process of dissociation, diffusion and precipitation which is discussed in detail the following chapter⁶⁵.

Lastly, carbon black (CB) and activated carbon (AC) are semicrystalline forms of zero dimensional carbon. Carbon black has a high surface area to volume ratio and possesses good thermal and electrical conductivity, though not on the same level as other carbon allotropes like graphene and CNTs. Activated carbon on the other hand has a very high surface area and is microporous making it useful in adsorption applications. Of equal importance though is the fact that they can be used as precursors for other carbonaceous materials such as graphene and carbon nanotubes.

2.2.2: One-dimensional carbons

One dimensional carbon arrangements are largely encapsulated by carbon nanotubes (CNTs). They have a cylindrical, one-dimensional structure. They can consist of single or multiple walls of graphene which are rolled into a cylinder. Similar to graphene, CNTs possess exceptional mechanical, electrical and optical properties. This is due to their similar electronic structures involving sp² hybridized carbon atoms and as such, they share many similar applications¹². However, unlike graphene, they possess a 1-D nanostructure, giving them extremely high aspect ratios, well in excess of 1000. This makes them particularly favourable for use in the production of continuous conductive carbon networks⁶⁶.

Several studies have demonstrated the viability of the production of carbon nanotubes (CNTs) from waste polymers. Tang et al. reported on the synthesis of multiwalled CNTs (MWCNTs) via the catalytic combustion of polypropylene⁶⁷. To achieve this, the researcher's combusted polypropylene samples in air using a gas lamp at 600 °C in the presence of an organic-modified clay and a nickel catalyst. The char product was then purified using hydrofluoric acid and nitric acid to remove the clay, nickel and amorphous carbon leaving behind MWCNTs, with yields up to 41.16 wt. %. The success of the system in air relied on the presence of the organic modified clay, which acted to restrict the path of gaseous carbon precursors allowing for slower interaction with the catalytic nickel.

Mishra et al. published a similar concept, only this time, using pyrolysis, rather than combustion⁶⁸. The investigation mixed polypropylene pellets with various metal oxides, nickel, cobalt and iron, and activated carbon as synergistic catalysts, at elevated temperatures. These mixtures were then carbonised in a quartz tube furnace under nitrogen flow at temperatures between 600 and 800 °C. Downstream of the polypropylene was a nickel catalyst where the vaporised carbon nucleated to form carbon nanotubes, making this ultimately a chemical vapour deposition method. This method relies on a temperature differential across the nickel catalyst to allow for carbon diffusion across the catalyst. This is similar to the method of graphene production presented by Narula et al.^{69, 70}. In their work, Mishra et al. were able to achieve yields of 20 wt. % CNTs⁶⁸.

Gong et al. published a paper suggesting a mechanism for the catalytic carbonization of polypropylene by combined catalysis of activated carbon with nickel oxide into carbon nanotubes⁷¹. Using a similar methodology to that of Mishra et al., involving using activated

carbon and nickel oxide as co-catalysts, the researchers were able to produce CNTs. They proposed a mechanism of layer by layer assembly of benzene rings to support the growth of their CNTs.

The only example of a polymer source other than polypropylene being used for the production of CNTs comes from the work of Nath and Sahajwalla⁷². They first produced a polyvinyl alcohol/fly ash composite by dissolving both into deionized water and then transferring it to a petri dish to dry. Once dried, the composite material was pyrolysed in a horizontal tube furnace under nitrogen flow at 500 °C for 10 minutes. Similar to the activated carbon in the previous two studies, the fly ash served as a catalyst in the cracking of the PVA structure. Ultimately, the study achieved 54 wt. % CNTs.

2.2.3: Two-dimensional carbons

Of particular interest over the past two decades has been graphene. Graphene is a hexagonal arrangement of carbon atoms along a 2D plane in such a way that each carbon atom in the crystal lattice is in a sp^2 hybridized state. This means that each atom supports both sigma bonds and pi bonding components⁷³. Graphene has been shown to possess exceptional mechanical and electrical properties such as the highest known intrinsic electron mobility and its extremely high charge carrier mobility¹⁰ shown in Figure 2.4.

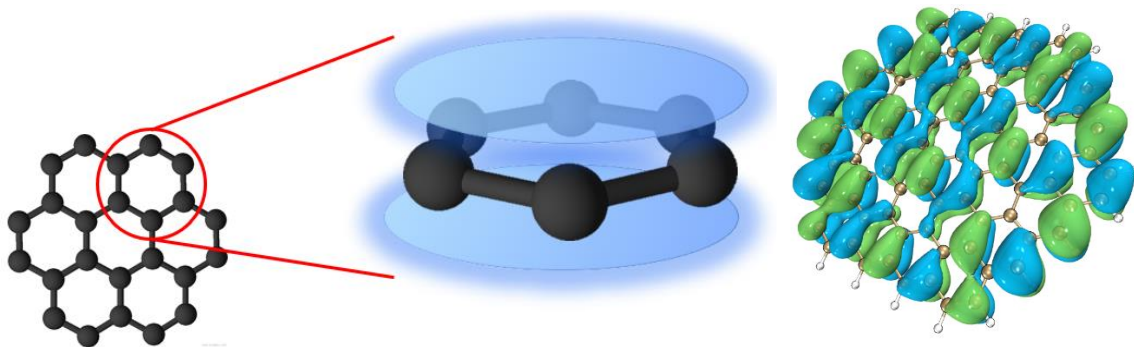


Figure 2.4: Diagram demonstrating charge mobility in sp^2 hybridized carbon species.

Several studies have shown the potential of converting polymers to graphene; however, the vast majority of these papers involves biological polymers^{16, 17, 19, 22}. In a 2012 study, Primo et al. carbonized chitosan coatings on arbitrary substrates to produce high quality, nitrogen doped graphene⁴¹. The methodology proposed started by coating hydrophilic surfaces, such as glass, quartz and metals with a chitosan thin-film. The film was then pyrolysed those substrates and coatings at temperatures up to 800 °C under argon flow. The result was the

production of few-layer, nitrogen doped graphene using a negative-value, waste precursor as a source of both the carbon and nitrogen. This is attributed to the presence of nitrogen in the chitosan's polymeric structure. They found that nitrogen doping occurred during the graphene formation, and that the chitosan precursor was advantageous for this application due to the propensity of carbohydrates to undergo carbonisation.

Similarly, Jin et al. demonstrated a process by which a more comingled biopolymer waste sample, dried distillers grains with solubles (DDGS), could be used as both a nitrogen and carbon source for the production of nitrogen-doped graphene²². After DDGS was processed with a solution of $\text{Ni}(\text{NO}_3)_2$ and then KOH, the nitrogen-doped graphene samples were obtained by graphitized activation at various temperatures under nitrogen. By pre-treating the grains with a nickel salt in the presence of KOH, nickel could be deposited onto the surface of the material. This surface modification acts as a catalyst during the pyrolysis process. The study found that the samples showed exceptional electronic properties, including a high specific capacitance (324 F g^{-1}) and an extremely low inner resistance (0.1Ω). It was noted that the most important factor affecting the electrical properties of the samples produced was the temperature at which the graphitized activation occurred. Results showed that 700°C under nitrogen flow was optimal for their precursor material.

Many studies have demonstrated the effectiveness of biopolymer waste as a source of material for the production of graphene. However, far fewer have been able to successfully demonstrate the use of synthetic polymers as a material source. Wang et al. demonstrated the synthesis of few-layer graphene sheets from a Kapton polyimide source⁷⁴. In a similar approach to that reported by Primo et al., the study used a polymer thin-film deposited onto a copper substrate, though in this case it was a synthetic polymer. The film was irradiated under microwave Ar/H_2 plasma which resulted in few layers of "urchin-like" carbon particles which consisted of few-layer graphene sheets vertically aligned relative to their longitudinal axis.

Sharma et al. looked into the synthesis of graphene from solid polymer waste using chemical vapour deposition²⁰. This represents a fundamentally different approach to the use of waste polymers as a source of materials for the production of graphene. This is attributed to its use of a single step process where the graphitization of the carbon was achieved by creating a carbon vapour. The researchers found that they could vaporise a polyethylene rich plastic

source in a furnace under Ar/H₂ flow and have it nucleate on a copper substrate in the form of graphene. This was achieved via chemical vapour deposition, a method of graphene synthesis which has been widely discussed for many years⁷⁵. While, again, characterisation was limited to the physical properties of the product, the research demonstrates a method by which a homogenous synthetic polymer could be used as a carbon source for the production of graphene²⁰. However, in a practical sense, this method has scalability issues due to its reliance on chemical vapour deposition (CVD). Due to the nature of CVD, production is limited to the size of the substrate able to fit into the furnace (Wang et al., 2009). The study also noted that it requires a very pure, clean substrate, with large grain sizes within the metallic lattice to reduce mismatch and help to minimise the number of graphene nucleation sites. Furthermore, for the large-scale growth of very uniform graphene crystals, the growth rate needs to be carefully controlled and proceed at a slow rate (Sharma et al., 2014). Due to these factors, the method is not practical for large scale graphene synthesis, certainly not on the scale required to process society's waste plastic. Still, it does present an interesting and different approach to waste plastic processing.

Essawy et al. presented the first demonstrated success of using an actual waste plastic as a carbon source for the production of graphene, using waste PET bottles⁷⁶. The study demonstrated a method by which recycled PET water bottles were processed into a uniform fraction size. This was achieved by crushing and sieving, then placed in a sealed autoclave reactor and heated at 800 °C for an hour. The resulting product was crushed, and characterisation showed the presence of few-layers graphene. While interesting for many reasons, its simplicity, its practicality and its scalability, just to name a few, the method does have some issues. From their characterisation, it is notable that the product of this method is largely amorphous, based on X-ray diffraction analysis, similar to highly amorphous, graphite-like carbon. Graphene is present however, which is corroborated by Raman spectroscopy, but the product is a far cry from pristine graphene. The researchers go on to experiment with the adsorption characteristics of the product and present a surface area of 721.7 m²g⁻¹ with a microporous structure having an average pore diameter of 2.1007 nm. While these properties are important for the focus of this research, dye adsorption, they are similarly important for the electrical properties of the material, particularly for use in electrode applications⁷⁷. It is notable that this study did not characterise the electrical properties of this material, nor did

it research potential doping, however the method seems promising for the reasons outlined above⁷⁶.

While this work is all important, there are still traditional areas of graphene production that have yet to be explored from a standpoint of a polymer waste source. One of the most well-known wet chemical methods of producing graphene oxide is the Hummers method⁷⁸. It is a wet chemical method for oxidising graphite as its sp² sites, increasing the interlayer spacing and dispersing the three-dimensional graphite structure into two-dimensional graphene oxide sheets. However, the method relies on a prolific dispersion of benzene rings to provide those sp² sites for oxidation, something which the amorphous carbon solid produced by pyrolysis of polymers lacks⁷⁸. That said, Alfe et al. have published a method by which strongly oxidized carbon black (a state of carbon which is semicrystalline) was then reduced with hydrazine. This process created water-insoluble few-layer graphene sheets which underwent self-assembly on a substrate after drying⁷⁹. This method is greatly impactful as it does not rely on harsh conditions typically required to restore carbon black to a graphitic network. All reactions took place in aqueous environments in standard laboratory conditions. Furthermore, the use of N-methylpyrrolidinone (NMP) as a solvent introduces the possibility to replace it with Cyrene. Cyrene has been described as a green bio-solvent. It is dipolar, aprotic and is derived from cellulose waste. It has a Kamlet-Abboud-Taft (KAT) polarity of 0.93, similar to that of NMP at 0.88 and Hansen solubility parameters and hydrogen bonding parameters indicate Cyrene is a very close solvent match to NMP⁸⁰.

Narula et al. have investigated a method by which an amorphous carbon source (not unlike the char created from the pyrolysis of waste polymers) can be deposited in a graphene layer on a copper substrate. The study also proposed mechanisms by which the graphene growth occurs^{69, 70}. The method involves the deposition of amorphous carbon, of thickness 80 nm onto a silicon/silicon dioxide substrate, followed by an 800 nm film of highly pure copper. When annealed in a hydrogen flow environment at high temperature and low pressure, the hydrogen gas is able to diffuse through the copper grain boundaries and interact with the amorphous carbon below. This creates thermomechanical stress in both the copper and amorphous carbon films, instigating the growth of graphene on the top side of the copper layer. Given its use of an amorphous carbon source, it is possible that this method could be applied to the pyrolysis char created from waste plastics.

Following on from this, another common method of graphene generation is physical vapour deposition. Like chemical vapour deposition (CVD) (which has been used in the generation of graphene from polymer waste) PVD gasifies a pure source material by evaporation. The gaseous component is then deposited onto a substrate in a thin-film via condensation using physical techniques such as electrical attraction and laser ablation. Only physical forces act in this process. This differs from CVD in which a precursor material and volatile carrier are vaporised. From the mixture, the precursor material condenses on a substrate and adheres via chemical attractions while the volatile carrier is removed via gas flow⁸¹. As of the time of writing, literature describing graphene production from polymer waste by PVD could not be found. This offers an interesting opportunity to explore the possibility of using PVD as a method to produce Graphene from a polymer waste source.

2.3: Liquid metals

For the purpose of this review, it is important to define what is meant by liquid metals. While all metals may be liquid, within the scope of this review, liquid metal refers to those which exist in a liquid state below a temperature of 250°C. These may be elemental metals, such as mercury and gallium, or alloys such as bismuth-tin, or gallium-indium-tin. These materials offer interesting opportunities for research in a wide variety of applications, due to their unique properties that result from their metallic bonding. Metallic bonding is broadly described as an electrostatic attraction between metal cations and their valence electrons, existing in a delocalised cloud. Typically, this results in a strong, but ductile material with good electrical and thermal conductivity, as well as generally high melting points. Of all elemental metals, only ten meet the aforementioned definition of being liquid metals. Six of these are the alkali metals, which will be excluded from discussion due to the fundamentally different nature of group 1 metals. One more, mercury, is also excluded, due to its limited use in the modern world because of its high toxicity. This leaves only three post-transition metals, which form the foundation of this discussion: gallium, indium, and tin.

2.3.1: Metallurgical overview

Liquid metals may broadly be categorised as being either elemental, or alloys, which are usually eutectic, leading to the material being monophasic. Biphasic liquid metals may be created through various methods, such as nucleation from a supersaturated state. However, these more closely resemble a colloidal suspension in a covalent liquid solvent, rather than a

true liquid. Unlike covalent, or ionic liquids, whose ratios of composition are defined by strict stoichiometric ratios, liquid metals are extremely tuneable. They may form throughout a range of substituent concentrations, which alters their properties greatly. As a result, they are more comparable to solvent mixtures, which makes them extremely versatile in the specificity of their application. Their low melting point is largely attributed to the crystalline structure of the materials solid phase. Gallium, for example, does not crystallise in a uniform manner. Its crystal structure contains short range Ga_2 dimers consisting of covalent bonds. These dimers then form longer range coordination with gallium atoms, forming an orthorhombic unit cell. As a result, the crystal structure of solid gallium is less symmetrical, with a higher degree of delocalisation than most metals. This results in weak bonding which is responsible for its low melting point. Similar trends can be seen in other low melting point post transition metals, such as indium and tin. This is contrary to most high melting point metals, such as tungsten, which exhibit highly symmetrical crystal structures, with lower degrees of delocalisation.

Alloying metals may modify their physical properties beyond that of their elemental counterparts. Various examples of gallium based alloys are presented in Table 2.7. In liquid metals, their melting point can be lowered below that of any of their constituent parts. Galinstan, as an example, is an alloy with a base of gallium, with indium and tin solutes at their eutectic point. This results in a melting point of 13.2°C . This can be attributed to the added solutes introducing disorder to the crystal structure of the base, which further reduces symmetry, thus lowering its melting point. This is achieved by the introduction of varying localised charge densities due to the solutes in the alloy. Indium atoms features a lower degree of delocalisation when compared to those of gallium and tin. This promotes movement of the crystallographic structure, where the indium atoms act to lubricate those of gallium and tin on an atomic scale.

Table 2.7: Properties of various gallium based liquid metal alloys⁸².

Elements	Concentration at which melting point is lowest (at.%)	Melting point (°C)
Aluminium	2.4	25.9
Silver	3.6	26.0
Bismuth	61.7	222.0
Mercury	2.0	27.0
Indium	14.2	15.4
Tin	8.3	21.0
Zinc	3.9	24.7
Indium/Tin	14.9/6.8	13.2

Additionally, alloying can provide enhanced properties which may be tuneable to electronic, and catalytic applications. LMs typically demonstrate supercooling, a process by which they remain liquid when cooled below their freezing point. This suggests the presence of short range crystallographic coordination within the liquid metal bulk as ordering during the freezing process is being disrupted⁸³. As an example of this short-range coordination, computational studies of liquid gallium suggest that the bulk consists of polygonal superstructures which themselves are made up of β -Ga, as well as Ga II and Ga III phases⁸⁴⁻⁸⁶. However, due to the complexity of analysis of liquid metals, many of these constituent structures have yet to be fully resolved, particularly in the case of alloys. One example of these structures within a LM alloy could be found. In the case of eutectic bismuth and tin, small covalent tetrahedral coordinated lattices were observed. Furthermore, these were found to persist to extremely high temperatures of 1000 K, at which point the covalent Sn-Sn and Bi-Sn bonds broke down⁸⁷.

In addition to the above being properties of the bulk, this short-range coordination has effects on the liquid metal surface and its interaction with materials at the interface. They have the effect of disrupting Van Der Waals forces between different LM species, thus lowering surface tension. In alloys, these constituent species may present at differing layers within the alloy, thus substantially changing their properties. For example, in the case of binary gallium alloys with other post transition metals, surface segregation creates a nearly homogenous surface layer of the solute metal at the air interface with the LM⁸⁸⁻⁹¹. Similarly, but not to the same extent, are eutectic alloys. Eutectic bismuth and tin demonstrates a surface concentration of

96% bismuth, with that concentration decreasing further into the bulk⁹². In a more extreme example, the surface of eutectic gallium and lead (containing 0.05 at.% lead) was demonstrated to contain exclusively lead frozen in a hexagonal monolayer encapsulating liquid gallium⁹³. This behaviour is associated with the varying surface tensions of the constituent elemental components with the lower surface tension metal forming the outer layer of the alloy⁹⁴.

The culmination of these factors offer interesting applications in catalysis. Surface compositions may be modified either in eutectic or binary alloys by tailoring the composition based on constituent surface tensions. Binary alloys may also provide a framework for access to active metal nodes within the liquid metal itself. This is discussed further in Chapter 2.4.3.1.

2.3.2: Properties of liquid metals

As a product of their metallic bonding, liquid metals share many of the properties that are common to all metals. However, their liquid state under relatively low temperatures gives them distinct advantages. For example, they are somewhat analogous to liquid solvents, and can be used to facilitate reaction environments that are utterly unique. While liquid metals generally exhibit low melting points, they offer extremely high boiling points when compared to other liquid solvents. Along these lines, liquid metals may also maintain their liquid phase at extremely high pressures, while maintaining low melting point. Gallium, for example, remains liquid at pressures exceeding 2.5 GPa at only 42°C without reaching its critical point⁹⁵. These properties allow liquid metals to be used as solvents for applications in extreme reaction environments at high temperatures and pressures.

Liquid metals also offer interesting electronic properties and applications. Metallic bonding is a result of electrostatic attraction between positively charged metallic cations and their delocalised valence electrons, which exist in a cloud. Typically, we describe solid metals as having positively charged cores fixed in a lattice, with free-flowing electrons. This is responsible for metals generally being good conductors of heat and electricity. In liquid phases of metals however, there is no such fixing of cations, and so both positive and negative charges are free to move. This fact makes for interesting applications of liquid metals, but also adds complexity in predicting electronic behaviour. This offers attractive opportunities for applications in flexible electronics, electrocatalysis, energy storage, electrochemistry, and microfluidics.

Furthermore, post transition metals are known to support localised surface plasmon resonances. Surface plasmons are electron oscillations at the interface between two materials that occur when excited by photons. In these materials, excitation occurs in the UV region below 280 nm. This phenomenon has applications in sensors, photocatalysis, and 3D printing.

2.3.3: Liquid metals in chemical reactions

In recent years, liquid phase catalysis has been demonstrated to be a successful concept. It originated in the form of high boiling point organic solvents containing metal complexes⁹⁶, and has matured to supported ionic liquid phase catalysis⁹⁷. These ionic liquids have been an improvement in many ways over their covalent liquid precursors, such as offering low vapour pressures and a highly electron rich environment. However, their limited thermal stability has relegated their use to applications below 200 °C. This makes their use unsuitable for highly endothermic reactions, and those with intrinsically slow kinetics⁹⁸. As discussed previously, liquid metals offer an extremely broad working temperature range, making them favourable for this type of application, while maintaining advantages of ionic liquids, such as low vapour pressures. In addition, their electron rich environment, and their support for photonic surface plasmon resonance offer prospects for electrocatalytic and photocatalytic properties, respectively. This leads to a diverse range of applications summarised in Figure 2.5. This distinguishes liquid metal catalysts from traditional ionic and covalent liquid catalyst environments⁹⁹. However, drawbacks do exist and must be understood when looking at applications of liquid metal catalysts. One such drawback is the minimal solubility of organic molecules in liquid metals. As such, catalysis between organic molecules and liquid metals is relegated to surface interactions¹⁰⁰.

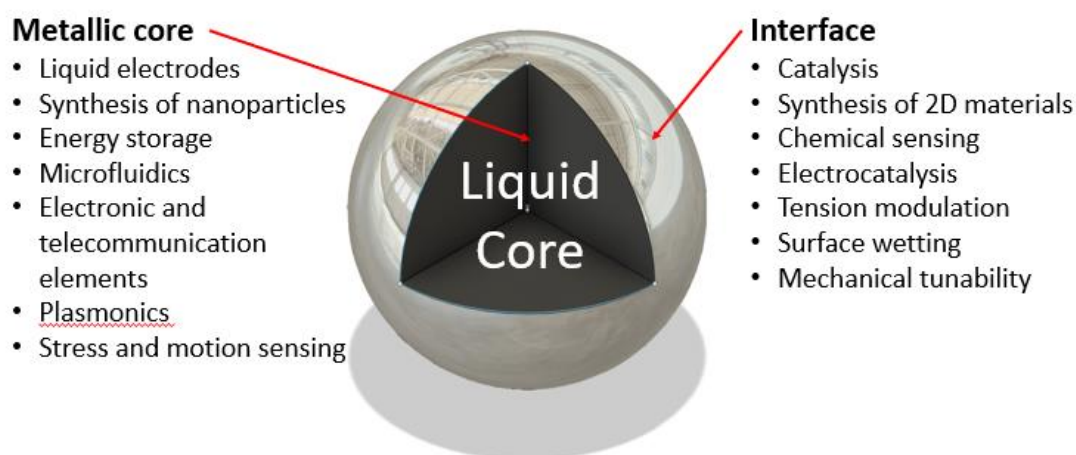


Figure 2.5: A schematic representation of bulk and interfacial applications of liquid metals. Adapted from work from⁹⁹.

Gallium provides an excellent base for the production of liquid metal catalysts due to its low melting point, and the relatively high solubility of almost all other metals in it. This means that, while catalytically active itself, gallium may also be tuned to suit specific applications by the introduction of other metals in catalytically active quantities. Despite its limitation of low organic solubility, this makes gallium a particularly suitable base for binary, tertiary and quaternary alloys with catalytic applications involving organic reactants¹⁰¹⁻¹⁰⁷. As a result, these types of catalysts have shown promise in applications of thermal cracking of organic molecules, where reaction temperatures are significantly lowered, and yields of valuable materials such as functional carbons¹⁰², and valuable gases such as hydrogen^{107, 108} are significantly increased as shown in Figure 2.6. However, these processes are still very much in their infancy. This presents exciting opportunities for further application of tuned liquid metal catalysts.

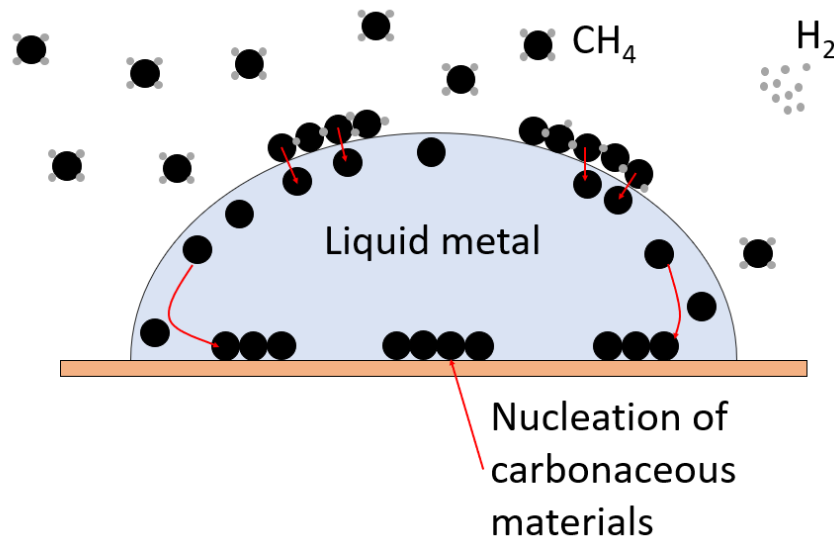
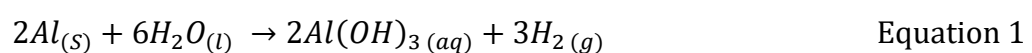


Figure 2.6: A proposed mechanism for methane dehydrogenation and nucleation of carbonaceous materials in liquid metal. Adapted from work from¹⁰⁹.

In addition to their applications in heterogeneous and homogeneous catalysis, applications in electrocatalysis have also been demonstrated. As a result of their metallic bonding, liquid metal catalysts offer a significant increase in conductivity compared to other liquid catalytic counterparts. Particularly promising is their application in green fuel production, particularly relating to hydrogen generation. In a particularly simple example, gallium can facilitate the dehydrogenation of water in the presence of aluminium under atmospheric conditions. The reaction can be given as:



Aluminium is particularly resistant to corrosion due to the rapid formation of a thin, strong oxide layer on its surface. However, in the presence of gallium, this oxide layer is degenerated, allowing the reaction with water to take place. In the presence of a strong acid, the aluminium hydroxide product is dissolved, facilitating a self-sustaining reaction until the aluminium has been consumed¹¹⁰. Earlier work has found that gallium offers the lowest enthalpy of activation for dehydrogenation reactions as well as the lowest overpotential in comparison to other liquid metals, including mercury. However, at a requirement of 0.7V to achieve current density of 1 mA cm⁻², it is not competitive with electrocatalytic alternatives from 50 years ago, let alone modern alternatives¹¹¹. However, this area is extremely under researched, and the alloying of gallium with other transition

metals may offer extreme advancements in both lowering the enthalpy of activation for dehydrogenation reactions, as well as overpotential.

Similarly, an under researched potential application of liquid metal catalysts is their photocatalytic properties. As previously discussed, post transition metals are known to support surface plasmon resonance. As a result, they have demonstrated photocatalytic properties. However, at the time of writing, the bulk of published research focuses on the photocatalytic properties of solid state post transition metals. Only two examples taking advantage of this photocatalytic property of liquid metals could be found^{112, 113}. Both studies referred to take advantage of the self-limiting nature of oxidation of liquid metal surfaces, as well as their surface uniformity to create 2D nanoflakes of high quality, monocrystalline gallium oxide. These studies demonstrate the tuneable plasmon resonance¹¹², and enhanced photocatalytic performance, which was attributed to a narrowed bandgap of 1.65 eV caused by the raised valence band and induced by trap states¹¹³.

2.3.3.1: Dehydrogenation

LM's have been shown to be a viable method for the dehydrogenation of light hydrocarbons when employed as a support media for catalytically active solutes¹¹⁴. Supported catalytically active liquid metals (SCALMS) involve utilising a catalytically inactive LM as a solvent for active metals. The concept was initially developed as supported ionic liquid phase (SILP) catalysts¹¹⁵, however, the application of the concept to liquid metal solvent comes with several key advantages. LM's have a significantly higher boiling point than any ionic liquid, making them more versatile in thermocatalytic applications when needing to overcome an endothermic reaction. As mentioned in previous chapters, LMs also have excellent resistance to coking⁹⁸, which is extremely beneficial in hydrocarbon dehydrogenation, as deactivation of solid catalysts has proven a significant hurdle to overcome. This makes SCALMS extremely promising for application in the dehydrogenation of hydrocarbons^{98, 116}. Several common catalytic additives to gallium for use in SCALMS are given in Table 2.8.

Two active elements have been predominantly proposed for use in SCALMS for this application: palladium, and rhodium. Rh and Pd SCALMS systems have shown promise as hydrocarbon dehydrogenation catalysts^{104, 117}. It is presumed that the mechanism of action is the activity of Pd and Rh atoms, to which the LM provides a homogenous environment^{98, 105, 118}. In favour of this hypothesis, *Redekop et al.*¹¹⁹ found that Ga-Pt SCALMS with Ga to Pt ratios

greater than 2 demonstrated lower activity but more selective and resulted in a higher resistance to coking. However, this is not well understood, and other mechanisms may contribute, or be solely responsible for the catalytic activity¹²⁰.

Table 2.8: Experimentally determined solubility of common catalytic additives in gallium¹²¹.

Element	Solubility (at.%) (400°C)	Solubility (at.%) (600°C)
Chromium	$1.2 \cdot 10^{-2}$	$4.9 \cdot 10^{-2}$
Cobalt	$7.8 \cdot 10^{-2}$	0.3
Copper	15.0	28.0
Germanium	8.9	19.8
Iron	$1.9 \cdot 10^{-2}$	0.1
Nickel	0.6	1.4
Palladium	12.5	23.0
Rhodium	1.3	-
Vanadium	$2.0 \cdot 10^{-3}$	$1.0 \cdot 10^{-2}$

In situ characterisation is required to fully understand this process, leaving opportunities for future work. Despite this lack of understanding, if coupled with carbonisation reactions, and applied to polymers, further recovery of resources could be achieved. Recovered H₂ could potentially be used to offset the energy requirements of the heating process of carbonisation in a way which would not contribute to the release of greenhouse gases.

2.3.4: Fluid dynamics and their effect on reactor design

Consideration must be made when LM reactors which incorporate bubble columns are designed. The fluid dynamics of liquid metals can have substantial effects on the gas-LM interaction of the system. The surface area of the reaction is largely dictated by the size of the bubbles passing through the bubble column. This is principally determined by two factors: the LM viscosity, and the LM surface tension. The viscosity of a catalytic system is associated with its reaction rate since viscosity is the primary factor in influencing the diffusion, deformation and motion of bubbles moving through a liquid catalyst¹²⁰. The relationship between these factors can be expressed as follows:

$$\eta D \propto \frac{kT}{a} \quad \text{Equation 2}$$

where η is the viscosity of the liquid, D is the self-diffusion coefficient, k is Boltzmann's constant, T is the absolute temperature, and a is the atomic size parameter¹²². Higher diffusivities are inversely proportional to viscosity, which is proportional to temperature.

The surface tension of a LM catalytic system, as well as pressure at the nozzle of a bubble column dictates the size of the gas bubbles expelled from that nozzle¹²³. High surface tension and pressure reduces the surface area of gas bubbles due to spontaneous coalescence, resulting in fewer, larger bubbles, as well as shorter residence time.

Two common methodologies exist for maximising the surface area contact in LM bubble column reactor designs. The surface area of the LM may be increased through the generation of nanodroplets of LM^{124, 125}. This simultaneously has the effect of lowering surface tension, as electrons are enclosed inside each nanodroplet, and unable to flow freely resulting in the inter-droplet attraction is far less than the intra-droplet attraction and allowing gas bubbles to pass between these nanodroplets. Nanodroplet generation can be achieved easily through the application of a high shear force, commonly sonication¹²⁶. These droplets will tend to coalesce over time but can be stabilised by performing the process in a protective organic liquid environment¹²⁷.

Additionally, electrochemical fragmentation may be applied to reduce the capacitance of the LM electric double layer. This in turn lowers the surface tension, and is shown by the Young-Lippmann equation:

$$\gamma\Delta\cos\theta = \frac{cV^2}{2} \quad \text{Equation 3}$$

where γ is the surface tension, $\Delta\cos\theta$ is the difference in contact angle between 0 volts and the applied voltage, c is the capacitance, and V is the interface potential¹²⁸.

A third method is occasionally employed to lower surface tension, but more consideration needs to be made to its implementation. The introduction of impurities may decrease surface tension by disrupting the localised charge densities at the LM surface¹²⁹. This can be done by alloying metals with lower surface tension. However, it is necessary to consider the total composition of the LM with this approach. The solvent metal will have a limited solubility, and it may be more important to prioritise the dissolution of other metals, such as catalytic additives.

2.4: Summary

As outlined previously, polymer waste represents a significant issue for the planet. The feasibility of any solution relies on four main factors: technical feasibility, environmental impact, resource recovery potential and the economics of the process. These aspects are intertwined in a synergistic way, and so, all must be adequately addressed. As shown above, research is clear that the generation of carbonaceous materials from a waste polymer source is technically feasible. However, a primary consideration is the specificity of methods outlined. In any real world application, sorting of polymer waste is a difficult, energy intensive and costly procedure. As a result, contamination of precursors is likely to present as a technical issue if such processes were to be enacted as solutions. For a viable solution to be deployed, it must be resilient to the wide array of materials which may be fed into it. These not only include various types of polymers, but also other additives, like stabilising agents, and dyes, which are commonly found in waste polymer streams. Next, the environmental cost must be considered. At present, waste plastic represents a significant environmental concern. Waste plastic carbonisation would provide a significant step forward in this regard, because it would act as a form of carbon sequestration. However, a commonality to all the studies outlined is their requirement for high temperatures. This requires significant amounts of energy to achieve. As such, the environmental benefit must outweigh the detriments of high energy usage. This could be achieved by powering the process using renewable energy sources, or by lowering the energy requirements through the use of catalysts, such as LMs. Ideally however, the solution would employ aspects of both. If the technical feasibility and the environmental impact can be overcome sufficiently, then there needs to be some application for the carbon materials produced. As the generation of polymer waste is being measured in the millions of tonnes, this process would result in large amounts of carbonaceous materials being produced. Without an application, the need for a true processing cycle is not being adequately addressed. Traditional applications are already well understood, such as in electronics, catalysts and adsorbents. In addition to this, new, and large scale applications would need to be explored, such as soil remediation, and wastewater treatment. Finally, any solution should be economically viable. That is to say, that the process should be financially self-sustaining. Simplistically speaking, this would occur when the costs of the processing are outweighed by the value of the product. Already, waste plastics are negative value commodities, which may significantly offset the requirement for the

production of valuable products. By employing aspects of other outlined factors, this may be achievable. Lowering energy requirements would lower the overall cost of production of these carbonaceous materials. Research into applications may lead to increasing value of the carbonaceous materials. If the outlined factors are significantly addressed, the carbonisation of waste polymers may present a promising method for the management of our ever-increasing consumption of polymers.

Chapter 3: Materials and methods

3.1: Overview

This thesis aims to carbonise waste plastics at low temperature using a custom reactor, and various catalysts at different stages of the process.

3.2: Materials and reagents

Hydrochloric acid (37%), silica powder, and alumina combustion boats were obtained from Sigma Aldrich. Alumina powder was obtained from Fulka chemicals. Zeolite powder was obtained from Ajax Chemicals Molecular Sieve Type 5A which were ground to a powder in a mortar and pestle. Gallium (99.99%), indium (99.99%), and tin (99.9%) were obtained from RotoMetals.

Polyethylene terephthalate sample was obtained from waste coca cola bottles. Polyethylene sample was obtained from waste plastic shopping bags. Polystyrene sample was obtained from disposable cups. Polypropylene sample was obtained from used falcon tubes. These waste plastics were washed in water, then cut to $\sim 1\text{cm}^2$ sections. Nylon pellets and polyacrylonitrile powder were obtained from Sigma Aldrich. Milli Q water was used throughout this work.

3.3: Processing and production of materials and reagents

Galinstan was synthesised with a standard ratio of 68.5% gallium, 21.5% indium, and 10% tin¹³⁰. Indium and tin were cut from a larger stock ingot and weighed by difference into a Pyrex beaker. Gallium was first melted in a warm water bath. The required mass of liquid gallium was then transferred to the Pyrex beaker using a disposable pipette. The Pyrex beaker was placed on a hotplate with a thermocouple inside and insulated with aluminium foil. The hotplate was then heated above the melting point of the substituent components (232°C). Once desired temperature was achieved, the mixture was mechanically ground inside the beaker using a glass rod to ensure homogeneity of the product. Eutectic gallium-indium and eutectic bismuth-tin were synthesized in the same manner using their respective eutectic ratios¹³⁰.

3.4: General apparatus setup and use of reactor

A reactor was assembled using a horizontal tube furnace, a vertical tube furnace, Swagelok Ultra-Torr vacuum fittings, stainless steel tubing, and custom-made Pyrex glassware. Mass-flow controllers were obtained from Cole-Parmer. Alumina combustion boats were obtained from Sigma Aldrich. The reactor is summarised visually in Figure 3. 1.

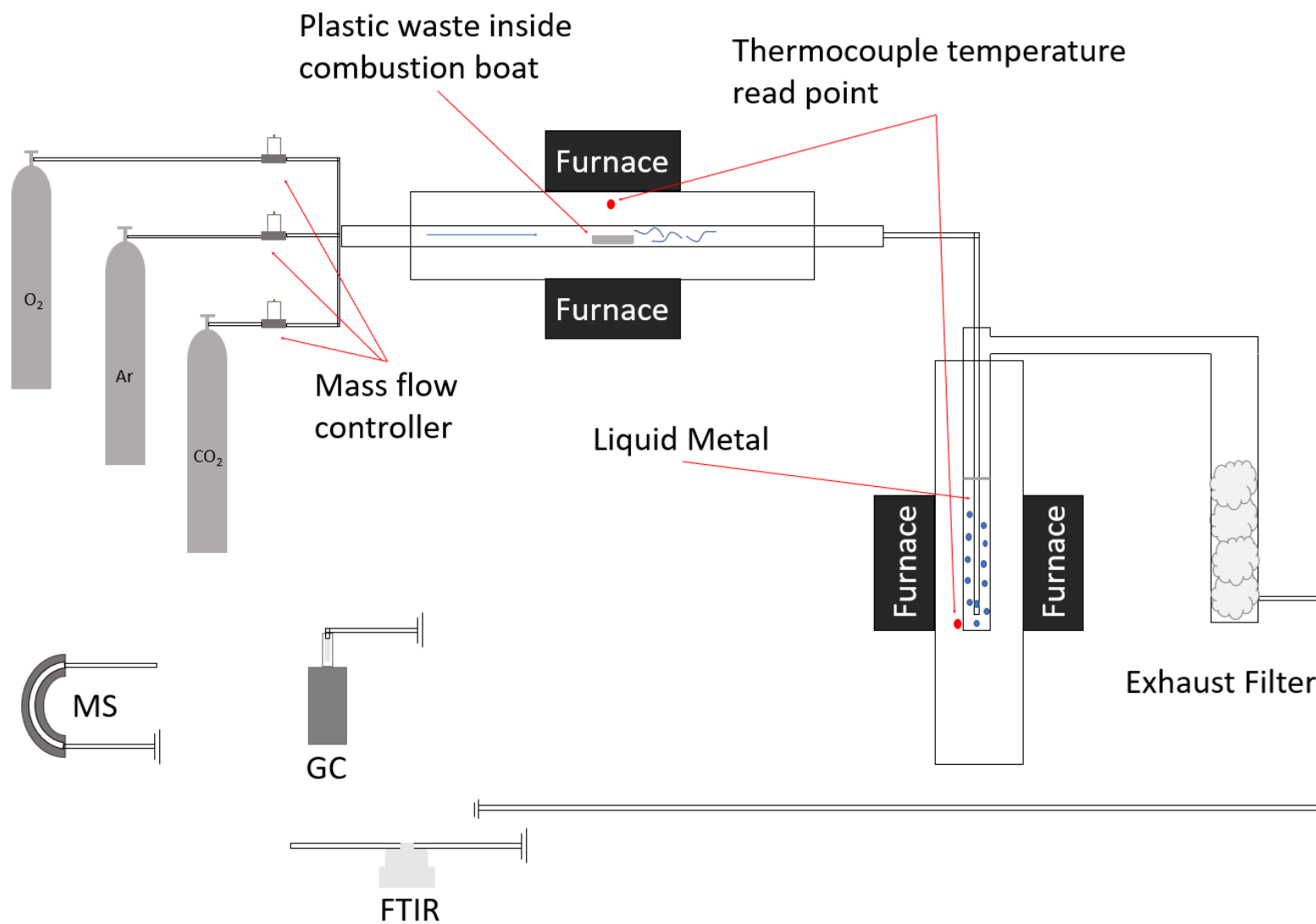


Figure 3. 1: General reactor design and setup.

A horizontal tube furnace with a quartz sacrificial tube was set up. Plastic samples of approximately 0.8 g were loaded into an alumina combustion boat and placed in the centre of the furnace. In experiments involving pre-catalysts to lower the temperature threshold for plastic decomposition, the additives were added to the combustion boat along with the plastic. Flanges were then secured to the sacrificial tube, and the system was purged with argon for 30 minutes at a flow rate of 0.5 L min^{-1} .

Meanwhile, a bubble column was filled with $\sim 40 \text{ g}$ of galinstan, prepared immediately beforehand as per the methodology outlined in Chapter 3.3. The column was secured inside a vertical tube furnace with a retort stand and clamp and heated to 375°C . To the exhaust of the bubble column, a filter consisting of quartz wool was attached using Quickfit ground connectors and rubber hosing.

After purging was complete, the gas flow rate was lowered to the desired flow rate, and the exhaust flange of the horizontal tube furnace was connected to the inlet of bubble column using SwageLok Ultra-Torr vacuum fittings, and stainless-steel tubing. These connections were wrapped in SuperWool insulation to maintain temperature between the horizontal and vertical furnaces. The horizontal tube furnace was heated to 600°C and the reaction was allowed to proceed for 6 hours.

After 6 hours elapsed, the furnaces were set to cool to room temperature, the gas was switched off, and the reactor was dismantled. The bubble column was removed from the vertical tube furnace and allowed to cool in air.

When cooled, the bubble column and filter were taken for further processing. The sacrificial tube, and combustion boat were cleaned by burning off contaminants with a Bunsen burner, then washed with pyroneg and water.

3.5: General modification of polymer precursors

Plastic precursors were modified with metal oxide additives to promote thermal cracking into lighter fractions. Plastic precursors were placed into Pyrex beakers along with a metal oxide powder (silica, alumina, or zeolite) in a ratio of 3:1 plastic to metal oxide. The mixture was then heated on a hotplate to the melting point of the plastic. Once liquid, the plastic was removed from the hotplate and mixed while cooling to roughly distribute the metal oxide particles amongst the plastic matrix. Once hardened, the composite was removed from the

beaker in a small puck and broken up into ~5mm cubes. These cubes would be the metal oxide composite precursors for relevant experiments.

3.6: Post-run processing

After reaction, the bubble column and filter were processed using an ~2 M hydrochloric acid wash. The bubble column and filter with HCl were capped with Parafilm and sonicated for 30 minutes with intermittent shaking.

The contents of the bubble column were poured into a 50 mL falcon tube. The Galinstan layer was removed into a fresh falcon tube using a disposable pipette. The acid and carbon dispersion from the filter were poured into a separate falcon tube. The two carbon and acid mixture were then centrifuged at 4400 RPM for 10 minutes. The supernatant was discarded, and the residue was redispersed in Milli Q water using sonication and vortexing to wash. This washing process was repeated three times to obtain washed carbon.

If small amounts of galinstan persisted through the washing process, the solution was transferred to a mortar and pestle. The solution was then ground to remove the oxide coating from the liquid metal surfaces allowing them to coalesce where they could then be removed to the Galinstan falcon tube.

3.7: Product characterisation

3.7.1: Scanning electron microscopy

Scanning electron microscopy (SEM) was performed using a Zeiss Supra 40VP scanning electron microscope to observe morphology. Samples were dispersed in a small amount of Milli Q water. Droplets were deposited onto silicon wafers mounted to a glass slide, and then dried to leave carbon sample affixed to silicon. Some samples used gold coating, which was performed by sputter coating for 45 seconds using an Emitech K975 sputter coater.

3.7.2: Energy dispersive X-ray analysis

Energy dispersive X-ray analysis (EDX) was performed using a Zeiss Supra 40VP scanning electron microscope fitted with an Oxford Instruments INCAx-act to measure the elemental composition of samples, and to perform elemental mapping. Samples were prepared in the same way as in Chapter 3.7.1.

3.7.3: Raman spectroscopy

Raman spectroscopy was performed using a Renishaw InVia Raman Spectroscopy, using a 514 nm laser, and 1900 gating. Samples were prepared by placing powdered sample on a glass slide, and measuring Raman shift between 200, and 3200 cm^{-1} at 10 % laser power for 10 seconds using a 50x L lens. Standard curve fitting and smoothing and deconvolution was performed on the resulting spectra using Origin Pro 2019 software.

3.7.4: X-ray diffraction

X-ray Powder Diffraction (XRD) was performed using a Bruker D8 Advanced X-ray Diffractometer with a copper X-ray source (0.154 nm). Diffractograms were measured between 5 and 90°2 θ with step sizes of 0.045°2 θ and 2 seconds exposure per step. Data was smoothed using 50-point Savitzky-Golay method with a polynomial order of 2.

3.7.5: Fourier-transform infrared spectroscopy

Fourier-transform infrared spectroscopy (FTIR) was performed using a Thermo Scientific Nicolet iS5 FTIR spectrometer, fitted with an iD7 ATR, running 32 scans. Specific sample preparation is commented on in the relevant discussion of results.

3.7.6: Ultraviolet-visible spectroscopy

Ultraviolet-visible spectroscopy (UV-vis) was performed using a Shimadzu UV-2600 spectrometer and quartz cuvettes between 1000 and 200 nm at a scan rate of 100 nm/min.

3.7.7: Thermogravimetric analysis

Thermogravimetric analysis (TGA) was performed using a TI Instruments TGA Q500 under a nitrogen atmosphere. Analyses involved a balance purge flowrate of 40 mL/m, a sample purge flow rate of 60 mL/min, a ramp rate of 20°C/min and ranged from ambient to 650°C. Approximately 25 mg of samples were used for each run.

3.7.8: X-ray photoelectron spectroscopy

X-ray photoelectron spectroscopy (XPS) was conducted using a Kratos Analytical Axis Nova XPS with the following scans: wide angle C1s, O1s, N1s, Ga2p3/2³, In3d5/2, and Sn3d5/2, and narrow angle C1s, O1s, and N1s. Samples were prepared by dispersion of sample in MiliQ water and then drop-casting onto a silicon wafer and drying at 105°C.

3.7.9: Nitrogen adsorption

Nitrogen adsorption measurements were taken using a Micromeritics Smart VacPrep 067 degasser and Tristar II Plus BET. Samples were degassed at 180°C over 24 hours under vacuum. All measurements were taken using nitrogen adsorbent at 77.30°K with all other parameters being measured by the machine and readings being recorded over 98 points between 0.01 and 0.9 atm relative pressure. Samples were weighed using a Sartorius A200S analytical balance and measurements were recorded after 60 seconds.

3.8: Software

MolView and ChemSketch were used to produce all structural formula images.

Origin graphing software was used for processing all data and graphs.

Chapter 4: Carbonisation of polyethylene and the effects of liquid metals

4.1: Introduction

In recent years, the study of post-transition metals has re-emerged as potential innovative materials with applications in electronics, microfluidics, catalysis, and as a reaction medium. These low temperature liquid metals maintain many of the properties expected of metallic solids such as conductivity relating to their sea of delocalised electrons and their high thermal stability. However, their liquid nature offers novel properties such as flexibility, atomically smooth surfaces, and various beneficial properties in solvation⁹⁹.

When applied as a solvent, liquid metals offer greater conductivity and thermal stability than even ionic liquids, while combining that with the tunability of solvent mixtures common to covalent solvents^{131, 132}. Furthermore, they may still provide a basis for the creation of colloidal suspensions by acting as a support for other materials, particularly other metals. As such, liquid metals offer solutions for applications as high-performance solvents for use as reaction environments^{98, 116}.

As a result of only recently renewed interest, many of their fundamental properties remain unknown. These include their atomic structure, and how that relates to fluidity and phasic nucleation, down to simple physical and chemical characteristics⁹⁹. This lack of understanding is also confounded by the difficulty in their characterisation, often requiring synchrotron radiation to fully resolve the nature of structures and properties of the liquid metal bulk, as well as observing in situ reactions. Additionally, while traditional ionic and covalent liquid systems follow defined proportions based on ridged atomic ratios¹³³, liquid metals do not. This means that alloys can exist in functionally infinite different combinations of constituent proportions.

Due to this lack of fundamental understanding, an analysis of candidate liquid metals must be assessed to support this work. It is theorised that the mechanism of action as it pertains to interaction with organic molecules relates to electron deficient and electron replete regions of the liquid metal. Galinstan as an example consists of a eutectic mixture of gallium, indium, and tin. The alloying of these creates disorder in the lattice by broadening the interatomic distances at indium and tin atoms¹³⁴. This is caused by electrons being tightly bound in lower orbitals in the indium and tin atoms, disrupting interactions between gallium atoms¹³⁴. This general principle of the introduction of atoms with tightly bound, low orbital electrons to

interfere with interatomic forces of the primary constituent component is the basis of the low melting point of many liquid metals^{135, 136}, and likely their ability to carbonise organic molecules. As such, a custom reactor was built, tested, and optimised. Three common liquid metal alloys were then chosen for analysis, as well as elemental gallium to act as a control. Optimised methodology outlined in Chapter 3 was used and polyethylene (PE) was chosen as a test plastic for further expansion to other waste plastics.

4.2: Reactor design

A custom reactor was constructed from a horizontal tube furnace, vertical tube furnace, Swagelok fittings and flanges, various glassware, and gas equipment. A photo of the setup is detailed in Figure 4.1.

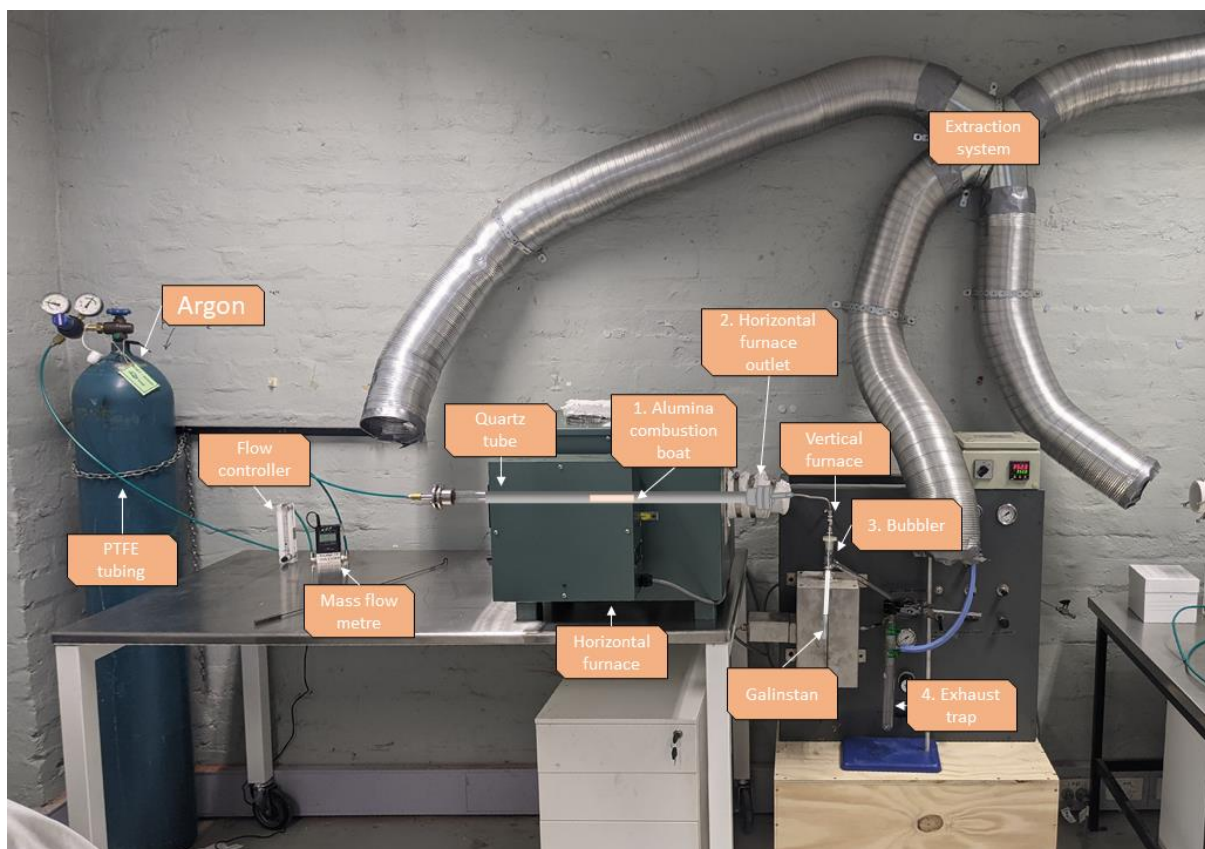


Figure 4.1: Custom reactor used for low temperature carbonisation of plastics.

Construction of the reactor setup first took place with a planning phase where the requirements were determined, and equipment was commissioned. An initial heating zone was required to melt and subsequently vaporise the polymer while thermally cracking it into a lighter molecular weight gas. This gas would then need to travel to a connected second heating zone where it would be bubbled through a column of liquid Galinstan at high

temperatures. As a result of the large volumes and distances travelled, autogenous pressure from the vaporisation of the polymer could not be relied upon to transport the polymer gas between heating zones; as such, a carrier gas was also required. Gas flow would need to be controlled and measured. Finally, a small volume bubble column was needed.

In the first design prototype, the initial heating zone consisted of a horizontal tube furnace, while the second heating zone was a paraffin oil bath on a hotplate. These zones were connected using 6 mm O.D. Teflon tubing and Swagelok compression fittings. An argon gas bottle using a BOC 6000 argon regulator provided the gas, and a bubble flow rate controller fixed and measured the flow rate. A small volume bubble column was constructed from a QuickFit Dreschel head and was adapted to a QuickFit borosilicate glass centrifuge tube. This first design presented several issues. It was observed that polymer condensation would occur at the exhaust of the first heating zone due to the significant drop in temperature between heating zones (point number 2 of Figure 4.1). The second heating zone was limited to the temperature of the hotplate; ostensibly 320°C, but in practice struggled to go any higher than 280°C. It was suspected that this was resulting in lower conversion rates. Polymer deposition was also observed between heating zones contributing to negligible yields. Finally, carbon was observed to deposit at the exhaust of the reactor suggesting that gas flow was carrying it out of the bubble column.

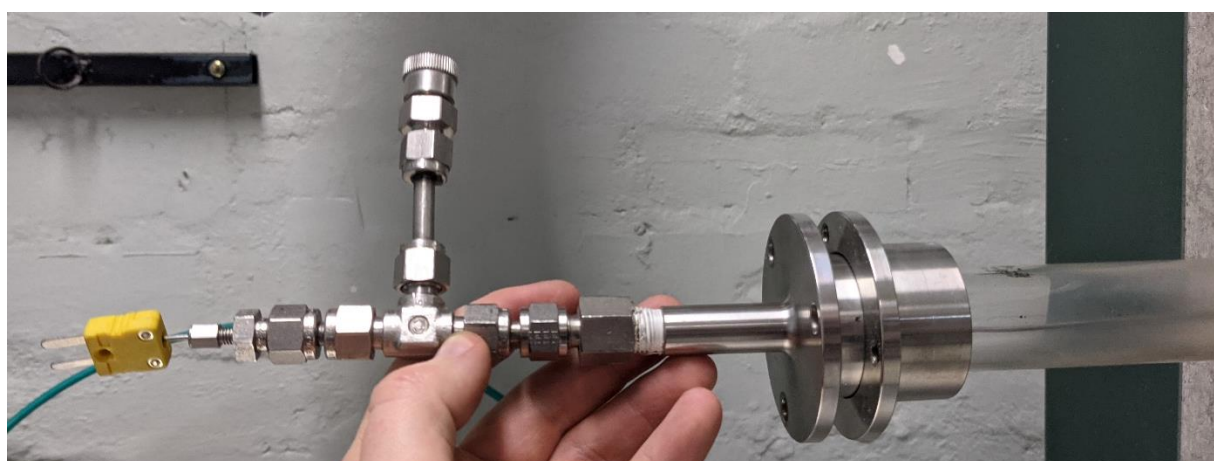


Figure 4.2: An example of the thermocouple flange setup used to calibrate internal furnace temperatures under reaction conditions.

A second prototype was developed to address issues identified with the first. The oil bath was replaced with a vertical tube furnace which allowed the carbonisation to occur at much higher temperatures, which were now limited by the melting point of the glassware being used. To

address polymer condensation the connection between the two furnaces was replaced with a shorter and more direct run of Swagelok stainless steel tubing with ferrule compression fittings. This connection was then insulated with Superwool ceramic insulation to keep internal temperatures as high as possible to avoid plastic condensation. Lastly, an exhaust trap filter was placed at the outlet of the bubble column using glass wool to filter particles carried by the gas flow (point #4 in Figure 4.1). The second prototype was further modified to address issues that continued to persist. It was found that the bubble flow controller was not suitable to accurately measure the gas flow through the system and so a mass flow metre was obtained and plumbed in series with the bubble flow controller. The internal temperatures of the horizontal tube furnace were calibrated under argon flow using a custom flange setup shown in Figure 4.2. Lastly it was observed that the tip of the Dreschel head was too wide in internal diameter. This resulted in the formation of larger bubbles; the effects of this are discussed later in the chapter. To rectify this, a Pasteur pipette was used as the gas injection tube. A small still head was used as the Y junction and a custom lid with a compression fit hole in the centre was used to insert the Pasteur pipette into the liquid metal. A diagram of this can be seen in Figure 4.3.

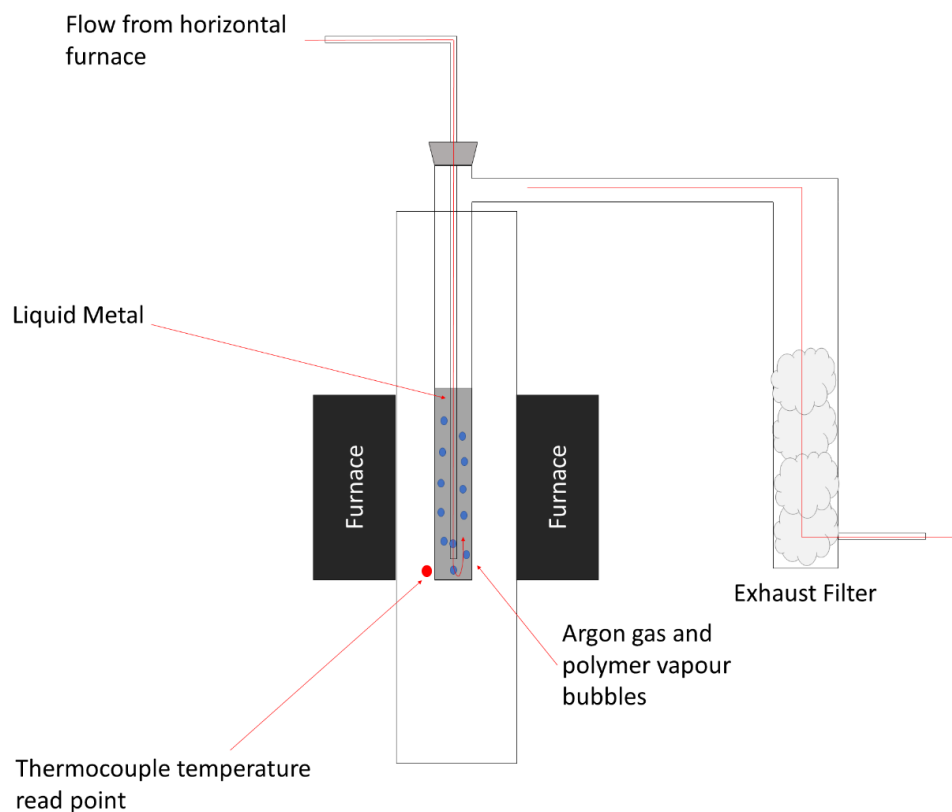


Figure 4.3: A close-up schematic of the bubble column; point 3 in Figure 4.1.

Some issues however could not be solved within the constraints of the project. Insulation and shortening of the connection between furnaces proved insufficient to keep the polymer gaseous and large amounts of deposition continued to occur in between heating zones (shown as point 2 in Figure 4.1). The methodology necessitates the vaporisation and thermal cracking of the plastic wastes, which occurs at temperatures below 450°C for all plastics investigated. However, horizontal furnace temperatures in the centre of the furnace (shown as point 1 in Figure 4.1) were calibrated to 600°C. This is much higher than literature reported decomposition temperatures shown in Table 5.1. However, this was done to keep the polymer vapours gaseous as they transitioned between heating zones. Further temperature increases were averted to avoid the pyrolytic decomposition of samples. With reactor design modifications discussed in Chapter 7.2 the temperature of heating zone 1 could be reduced significantly.

The use of a carrier gas was also noted to greatly affect carbonisation. The carrier gas was required to be inert so as not to contribute to polymer carbonisation and demonstrate Galinstan as the primary mediator of this reaction. However, it also had the effect of shielding the polymer vapours from the Galinstan surface. Reactions between liquid metals and reactants occur at the interface between the two. When a carrier gas is introduced to the system, a mixture of polymer vapours and gas occur, which extends to the bubbles in the bubble column. This dilutes the polymer vapours and reduces their concentration at the interface, thus reducing yields. It is desirable to eliminate carrier gas and rely on autogenous pressure to push polymer vapours through the system. Potential solutions to this are discussed in Chapter 7.2. However, the purpose of this work is to demonstrate the process at lab scale, and that discussed in Chapter 7.2 is beyond the scope of this work.

Lastly, the use of borosilicate glassware limited reaction temperatures in the bubble column. Observable damage was occurring beyond temperatures of 420°C. Quartz glassware would allow extended reaction temperatures to be assessed. This will be further discussed in Chapter 7.2.

4.3: Reactor optimisation

As a result of its custom nature, optimisation of the methodology first needed to occur. Carbonisation of five common municipal plastic wastes was conducted using galinstan, and

the products were characterised between iterations to the methodology. Finally, waste plastic samples were carbonised using the methodology outlined in Chapter 3.3. The characterisation methodology is covered in Chapter 3.7. Table 4.1 summarises tested properties.

Table 4.1: A summary of properties tried for optimisation.

Temperature (°C)	350	375	420
Time (hr)	2	16	
Nozzle depth (cm) (pressure (kPa))	3 (1.89)	6 (3.79)	9 (5.68)
Flow rate (L min⁻¹)	0.5	0.25	0.05

Various bubble column temperatures were tested, from 250°C to 450°C in 50°C increments. Temperatures exceeding 420°C were found to damage the borosilicate glassware used in the bubble column, while temperatures below 350°C produced negligible carbonisation. 375°C was found to strike a middle ground between reactor damage, and thermal catalysis.

Reaction times were investigated between 2 and 16 hours. Little apparent difference was observed based on longer reaction times. Thermogravimetric analysis showed that thermal degradation of plastics occurs rapidly. This is shown in Figure 5.2. It is theorised that, once thermal degradation temperature is reached, the plastic vapour is carried through the reactor by the carrier gas and subsequently through the bubble column. The reaction between LM and organic gasses occurs at the LM-gas interface¹³⁷⁻¹³⁹. As a result, once passed through the bubble column, any unreacted plastic vapour will be expelled from the system through the exhaust. As such, lengthening reaction times beyond that which allows the plastic to decompose and its vapour to be fully carried through the reactor has little effect on the resulting carbonaceous product.

Residence times could be assessed by varying the depth of LM in the bubble column. As opposed to reaction times, residence times significantly affected the carbonisation of the precursor. The depth of LM in a bubble column will define the time it takes for the gas bubble to pass through the LM and surface. Increasing the depth of LM in a bubble column increases the pressure at the nozzle, which has the effect of lowering the surface area of gas due to the spontaneous coalescence of bubbles, resulting in fewer, larger bubbles¹²³. As such, depth

must be carefully considered, as increasing depth beyond a point will reduce the LM-gas surface area, and the reaction rate will decrease. LM Bubble column depths were tested at 3, 6, and 9 cm, resulting in calculated nozzle pressures of 1.89, 3.79, and 5.68 kPa respectively. 3 cm depths were found to result in low carbonization. This was attributed to insufficient residence time between gas and LM.

At the other extreme, 9 cm depths were found to result in extremely large bubbles relative to the size of the column which displaced large amounts of LM. This created issues with flow rate, as bubble formation would not occur until the back pressure in the horizontal tube furnace exceeded the requirements to displace the mass of LM and overcome the pressure differential. This resulted in irregularly timed bubble formation and was observed to lead to more plastic deposition in the horizontal tube furnace, resulting from the back pressure. A depth of 6 cm was found to be a satisfactory middle ground between increasing residence time, maximising surface area, and progressing through the reaction without impeding flow.

Finally, carrier gas flow rates were tested at 0.500, 0.250, and 0.050 L min⁻¹. A high flow of carrier gas will result in a lower concentration of gaseous hydrocarbons in the bubbles in the bubble column, and as a result will reduce the efficiency of the furnace operation. Alternatively, a low flow rate will not be sufficient to carry gaseous hydrocarbons through the system reliably. As such, it is important that these factors be balanced when considering reactor methodology. It was concluded that flow rates of 0.250 L min⁻¹ met the required conditions optimally.

4.4: Effect of liquid metals on carbonisation

4.4.1 Gallium

Based on the mechanism of action discussed above, as well as in Chapter 2, it was hypothesised that gallium alone would not produce any carbonisation of PE. Gaseous remnants of thermally decomposed PE were pushed through gallium in a bubble column at 375°C using an argon carrier gas. When cooled, the gallium was processed using an ~2 M HCl acid wash in a warm water bath to keep the gallium in a liquid state. The hypothesis proved to be correct, and no carbon could be recovered from the gallium after the experiment.

4.4.2: Eutectic gallium-indium

Continuing with the use of the standard methodology and parameters, eutectic gallium-indium (EGaIn) was trialled. Due to its lower melting point, EGaIn was able to be processed using the standard post processing methodology outlined in Chapter 3.6. From this, a small amount of carbon was able to be recovered which proved to be insufficient for further analysis. As a result, further carbonisations were run, and the resulting product was combined to form a single sample for characterisation.

4.4.3: Galinstan

Galinstan samples were again processed with the standard methodology outlined in Chapter 3. Further supporting the mechanism of action discussed earlier in this chapter, galinstan resulted in the formation of a partially oxidised graphitic carbon from a PE precursor. Once again, this yield was extremely low, however it was observably larger in yield when compared to that of EGaIn carbonisation. Three syntheses were run to collect enough sample for characterisation. Notable here is that the reactor was optimised using galinstan, and so higher yields may be the result of an optimised process, rather than the addition of tin to the alloy. However, this is unlikely, as the process optimisations are primarily focused on elements of the reactor design, rather than the specific liquid metal in the bubble column. The one parameter which would be most likely to result in more favourable conversion using EGaIn is the bubble column temperature. This would likely only arise from a temperature increase. As such, galinstan would still be favourable over EGaIn as a lower energy alternative, only requiring the addition of a small amount of relatively cheap tin.

4.4.4: Eutectic bismuth-tin

Finally, eutectic bismuth-tin (EBiSn) is a considerably cheaper alternative to gallium based liquid metals due to the lower cost of bismuth and the higher percentage component of cheaper tin. This alloy has a melting point of 138°C ⁸² which presents problems with post-processing. As such, graphitic carbon could not be recovered from the bismuth-tin bubble column as it would resolidify upon the addition of ~ 2 M HCl and damage the glassware. Variations of bismuth tin alloys exist which lower this melting point below 100°C , however they contain lead and cadmium. Based on the environmental application of this work, alloys using toxic metals were avoided.

4.5: Raman spectroscopy of carbon products

Raman spectroscopy was employed to investigate the structure of the synthesised carbon. Samples produced from various liquid metals all demonstrated broad D band peaks around 1365 cm^{-1} , and G band peaks around 1590 cm^{-1} . Broadness of the peaks is attributed to inhomogeneous broadening resulting from a heterogeneous makeup of graphitic and amorphous carbons, as well as the presence of other potential impurities. The D band peak is typically associated with defects in a carbon lattice as a result of carbon atoms with dangling bonds (Figure 4.4) near the K point of the Brillouin zone^{56, 140}. G band peaks are associated with aromatic ring chain vibrations between carbon bonds and result from E_{g2} mode from sp^2 -bonded carbon atoms in a graphitic layer⁵⁶. Furthermore, on closer inspection, shoulders off the main D and G band peaks are clearly visible.

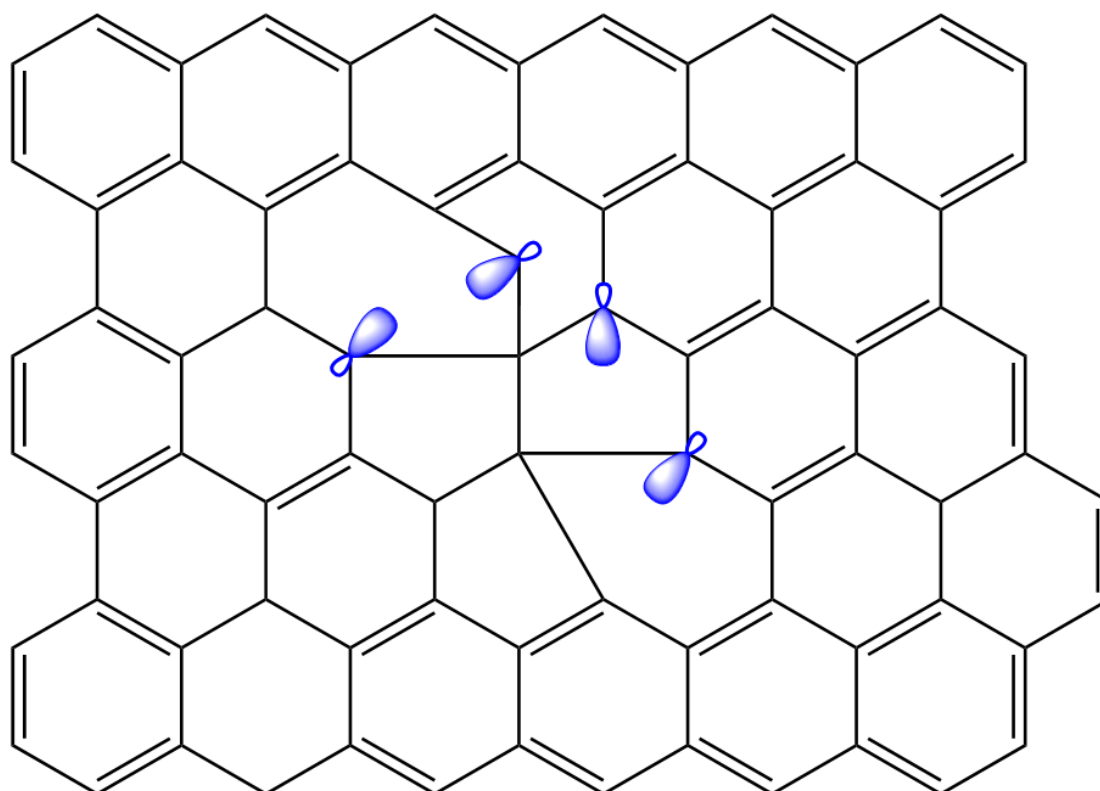


Figure 4.4: A schematic illustration of dangling bonds in an aromatic carbon lattice.

Amorphous carbons and chars typically exhibit a particularly complex Raman spectra as a result of their nonuniform lattice, the complicated nature of precursor materials, and the method of their formation¹⁴¹. Computational simulations of various polyaromatic hydrocarbons have provided an insight into the lattice features which give rise to these shoulders¹⁴² which can be seen in the deconvolution in Figure 4.5 and Figure 4.6. Smith et al

identify ten distinct peaks within the Raman spectra of amorphous chars. A summary of their findings can be seen in Table 5.3.

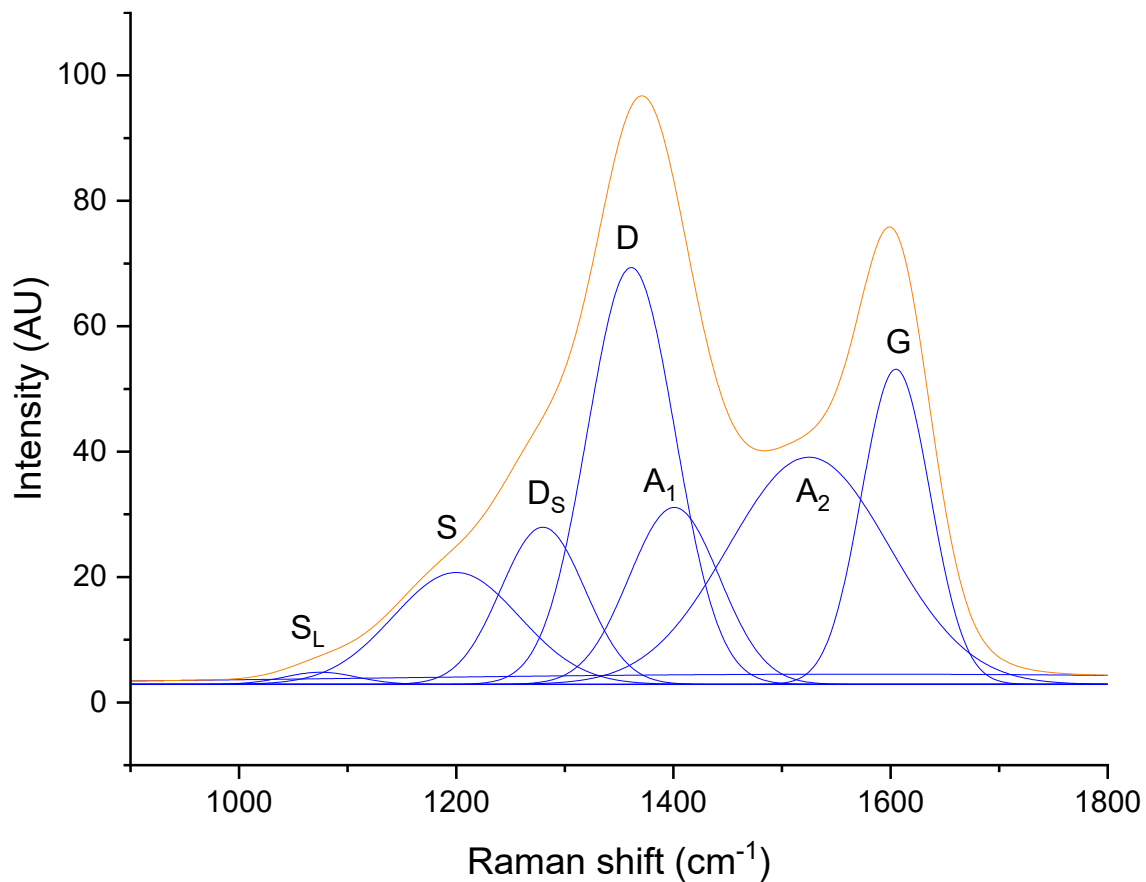


Figure 4.5: Raman spectrum of a carbonaceous sample produced from waste PE in EGaln with Smith et al. deconvolution method¹⁴² applied.

The Raman spectrum of partially oxidised graphitic carbon (POGC) synthesised from PE and EGaln shown in Figure 4.5 and that of PE and galinstan shown in Figure 4.6 have several features outlined by Smith et al. Shoulder band, low (S_L) is the product of weak breathing modes for small aromatic regions. These are ascribed to hydrogen motion along the carbon edge and are typically weak compared to other vibrations in the spectrum¹⁴². S_L is also associated with a secondary breathing mode for 7+ membered rings¹⁴³, as well as specifically with naphthalene. However, these vibrations are described as being stronger relative to the rest of the spectrum¹⁴². As such, it is likely that the small S_L band observed in the PE EGaln and PE galinstan samples are indicative of small aromatic regions in the POGC structure.

Shoulder band (S) is described as the product of primary breathing modes for 7+ member rings¹⁴³ and benzene rings adjacent to heteroatom defects¹⁴². The S band was strongly

present in the PE EGaIn sample, suggesting the presence of heteroatom defects and 7+ member rings. Given the lack of heteroatoms endogenous to the PE precursor, it is likely that these defects arise from the presence of atmospheric gases, primarily oxygen in the system. Due to the nature of the custom reactor, the horizontal tube furnace outlet shown in Point 2 of Figure 4.1 isn't located at the highest point of the quartz tube. During the purging process, the argon likely displaces atmospheric gases up to the point of this outlet, leaving a small amount of atmosphere in the top of the quartz tube which may result in partial oxidation during thermal decomposition of the PE. This is theorised to give rise to oxygen heteroatom defects in the POGC product of PE EGaIn. This band was not present in the PE galinstan sample, however due to a particularly prominent D_s band, a smaller S band is likely to be present, but unable to be deconvoluted from its neighbouring peak.

Defect band, shoulder and defect band (D_s and D respectively) are both present in all sample. The defect bands are of primary interest in the Raman characterisation of carbons, alongside the graphitic bands discussed later. D_s is the result of assorted breathing modes for polyaromatic hydrocarbons (PAHs), while D is the combined breathing and Kekulé vibrations for PAHs. In highly ordered systems, a double resonance effect, coupled with degeneracy intensifies the D band peak¹⁴⁴. In less ordered systems, coupling of breathing and Kekulé modes results in the D band being blue shifted away from the expected 1350 cm^{-1} ¹⁴². This further differentiates the D and D_s bands, resulting in a more pronounced shoulder. This is the case in the PE galinstan sample, whereas PE EGaIn exhibits a less prominent D_s band suggesting a more ordered lattice structure.

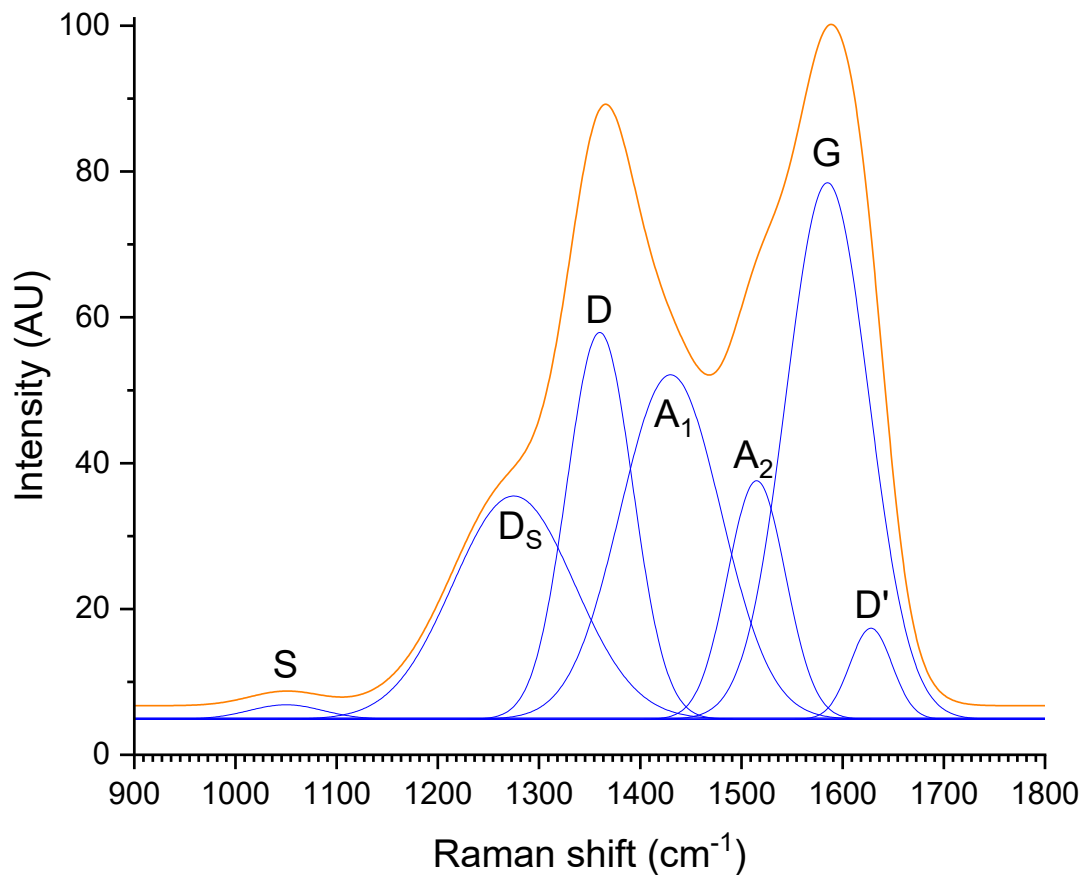


Figure 4.6: Raman spectrum of a carbonaceous sample produced from waste PE in galinstan with Smith et al. deconvolution method¹⁴² applied.

Literature on the origin of the amorphous bands (A_1 and A_2) is lacking in consensus. However, agreement exists suggesting they originate from the presence of irregular structures^{145, 146}. Smith et al.¹⁴² identified two distinct amorphous bands with origins in different sources. A_1 is found between 1400 and 1460 cm^{-1} and is ascribed to the Kekulé vibrations coupled to symmetric breathing of adjacent cyclopentane rings and is strongly associated with out of plane deformation around these defects. A_2 is found between 1500 and 1550 cm^{-1} and is primarily the result of point defects which give rise to asymmetric stretching and breathing modes in nearby ring systems. Secondly, A_2 may also arise from nearby oxygen defects which restrict the asymmetric stretch modes and result in the A_2 peak being red shifted¹⁴². It is in these two bands that another notable difference is presented, with PE galinstan samples demonstrating a more intense A_1 band and PE EGaIn demonstrating a more intense and broader A_2 band. This would suggest that PE galinstan samples contain a higher degree of out of plane deformations as a result of five-member ring structures while PE EGaIn samples

contain a higher degree of point defects. This is likely due to oxygen heteroatom defects as is suggested by the presence of the S band in the EGaIn sample.

The G-bands, like the D-bands, are peaks of primary interest in the Raman characterisation of carbons. They are well studied, and strongly associated with the asymmetric stretch of sp^2 carbons, particularly E_{2g} stretching in aromatic rings. While E_{2g} stretching is present in an array of molecules, the overall system symmetry has a large effect on the area and intensity of the G-band peaks. As a result of the complexity of the makeup of the G-band region, it can be theoretically broken up into a Gaussian and Lorentzian model to describe PAH cluster sizes, system symmetry, and the effects of defects¹⁴². The Gaussian model is assigned to the distribution of small PAH structures, while the Lorentzian model is assigned to large PAH structures. However, in all the spectra, attempts at separating these G-band components consistently yielded a lower coefficient of determination. As such, differentiation could not be achieved, and the G-band was left as a single peak. This is likely a result of working with low yields as signal to noise ratios were quite high and the Savitzky-Golay smoothing necessary for deconvolution likely masked the ability to differentiate these peaks. The PE EGaIn sample demonstrates a relatively small G band peak in comparison to that of the PE galinstan sample suggesting a higher degree of symmetry is present in the galinstan samples. This is likely the result of larger regions of aromaticity in these samples compared to PE EGaIn samples. Galinstan samples demonstrate characteristics of less ordered systems based on the blue shift of the D_s band. The prominence of this in comparison to EGaIn samples is likely due to larger regions of aromaticity giving more opportunities for coupling of breathing and Kekulé modes and resulting in the prominence of the D_s band.

Finally, D' band is assigned to the weak breathing mode of a central ring surrounded by asymmetric stretching behaviour. This band was only shown to be significant in coronene and cycloheptene centred ring systems. The D' band was only able to be deconvoluted from the PE galinstan sample. Due to the prominence of the A_2 band, this is expected and further reinforces the presence of 5 member ring structures in this sample.

4.6: Summary of findings

- A custom reactor was designed and constructed for waste plastic carbonisation in the presence of liquid metals.
- Reactor parameters including temperature, gas flow rate, liquid metal volume, and reaction time were optimised for best carbonisation and a summary of results can be seen in .
- The component of liquid metal has significant effect on carbonisation. Gallium alone produced no carbon from waste plastics, reinforcing theories as to the mechanism of action being related to charge discrepancies between constituent atoms in the liquid metal structure.
- Observable yields show a slight preference for the use of galinstan going forward.
- The higher melting point of EBiSn made it unsuitable for experimentation going forwards.
- Analysis of the POGC structure favours galinstan as a reaction environment due to its production of larger regions of aromaticity.

Table 4.2: A comparative summary of results from each liquid metal used in this chapter.

Liquid metal	Effect on process	Product summary
Gallium	Compatible with process	No product recovered.
EGaIn	Compatible with process	PAH formed. Smaller regions of aromaticity.
Galinstan	Compatible with process	More PAH formed. Larger regions of aromaticity.
EBiSn	Not compatible with process	No product recovered.

Chapter 5: Low temperature carbonisation of plastics using galinstan

5.1: Introduction

Since the first synthetic plastic, Bakelite, was reported in 1907¹⁴⁷, plastics have made them an ever increasing part of our daily lives due to their diversity in application, low cost, and robustness. Their disposal on the other hand, represents a loss in our non-renewable natural resources, huge losses in energy, and an environmental concern which rivals global warming³⁷. The persistent nature of plastic in the environment means that it poses a long-term threat to the planet. The accumulation of plastic waste in the ocean has created large gyres of floating plastic debris affecting marine life and disrupting the delicate balance of ocean ecosystems. The impact of plastic waste extends beyond the ocean and affects terrestrial-based ecosystems as well. Landfills overflowing with plastic waste are a source of greenhouse gas emissions, and the release of toxic chemicals from the degradation of plastic can contaminate soil and water sources¹⁴⁸. As indicated in Figure 5.1, only a small fraction of plastic waste is recycled in Australia, while most of the consumption is driven by the utilisation of virgin materials.

As such, a great deal of attention has been put towards finding a way to remediate these concerns. As outlined in Chapter 2, tertiary recycling, as a concept, offers the most promising solution, as it solves the traditional drawbacks of plastic recycling²⁴. However, finding a process that is low cost, produces valuable materials, and does not contribute to further pollution has proven to be challenging.

Galinstan is a eutectic alloy consisting of gallium, indium, and tin in a 68.5:21.5:10 % ratio by mass⁹⁹. As a result of their asymmetric, highly delocalised crystal structures, a mixture of these metals creates a disordered crystallographic structure due to varying localised charge densities¹³⁴, giving the alloy a melting point of only 13.2°C¹⁴⁹. As such, it can be used as a novel reaction environment which is highly tuneable, with an extremely broad usable temperature range⁹⁹.

It has been suggested that pure liquid metals do not catalyse reactions alone, but act as a heat transfer medium¹⁵⁰, in support of other catalytic methods of action¹⁵¹. Alloying of pure liquid metals has been shown to significantly increase their catalytic activity, and as such have shown promise in applications such as pyrolytic catalysts^{138, 139, 152}. Liquid metals show excellent resistance to coking, which demonstrates a significant advantage over their solid

counterparts⁹⁸. Liquid metals show very poor carbon solubility. As such, the lower density carbon product is separated from the liquid metal by buoyancy¹³⁹. It has been hypothesized that catalytic activity of atoms within a LM alloy is enhanced by electron donations between constituents¹³⁴. One constituent of the alloy will donate electrons to another constituent, which act as the surface activation site between the gas and liquid metal¹⁵². However, at present, this process is poorly understood, largely due to the difficulty of analysing *in situ* reactions involving LM's.

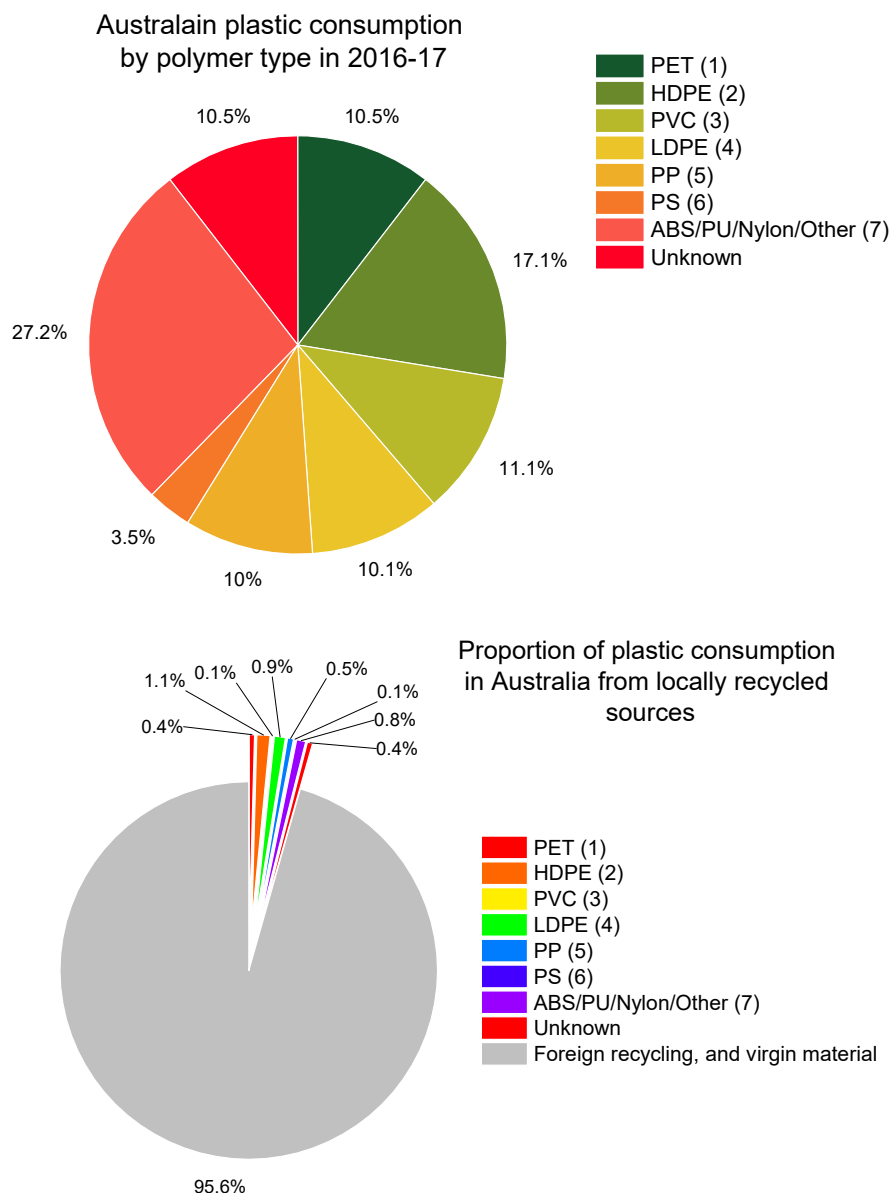


Figure 5.1: Consumption of plastics in Australia, and proportion produced from locally recycled sources¹⁵³.

Despite many clear advantages, the use of LMs as a reaction environment has been relatively unexplored; particularly in the area of recycling. Herein, this chapter describes the use of LM's as a reaction environment for the low temperature carbonisation of various industrially significant plastics (polyethylene, polyethylene terephthalate, polypropylene, polystyrene, polyacrylonitrile, and nylon 6/6). The chosen plastics represent a significant portion of both municipal and industrial plastic waste and encompass a wide variety of plastic types and properties. This work demonstrates the potential viability of this method of recycling.

5.2: Decomposition characteristics of plastics

Thermogravimetric analysis was utilised to characterise the thermal decomposition of various municipal waste plastic samples and virgin plastic samples outlined in Chapter 3.2. The results can be seen in Figure 5.2. The decomposition process can be generally categorised into four groups. Pure hydrocarbon plastics such as PE, PP, and PS experience a single decomposition step and decompose 100% by mass into volatile hydrocarbons. Oxygen containing plastics such as PET experience a single step decomposition with approximately 60% mass loss to volatile hydrocarbons. The remaining 40% is attributed to char as a result of PET oxidation by oxygen present in its structure. Plastics containing both nitrogen and oxygen such as Nylon similarly show a single step decomposition but lose 100% of their mass, similar to pure hydrocarbon plastics. Finally, plastics containing nitrogen but no oxygen such as PAN, show a more complicated decomposition and thermograms will often be dependent on parameters such as heating rate which will dictate intermediary reactions. However, typically nitrogen containing plastics will decompose in a two-step process, with overall mass loss dependent on heating parameters.

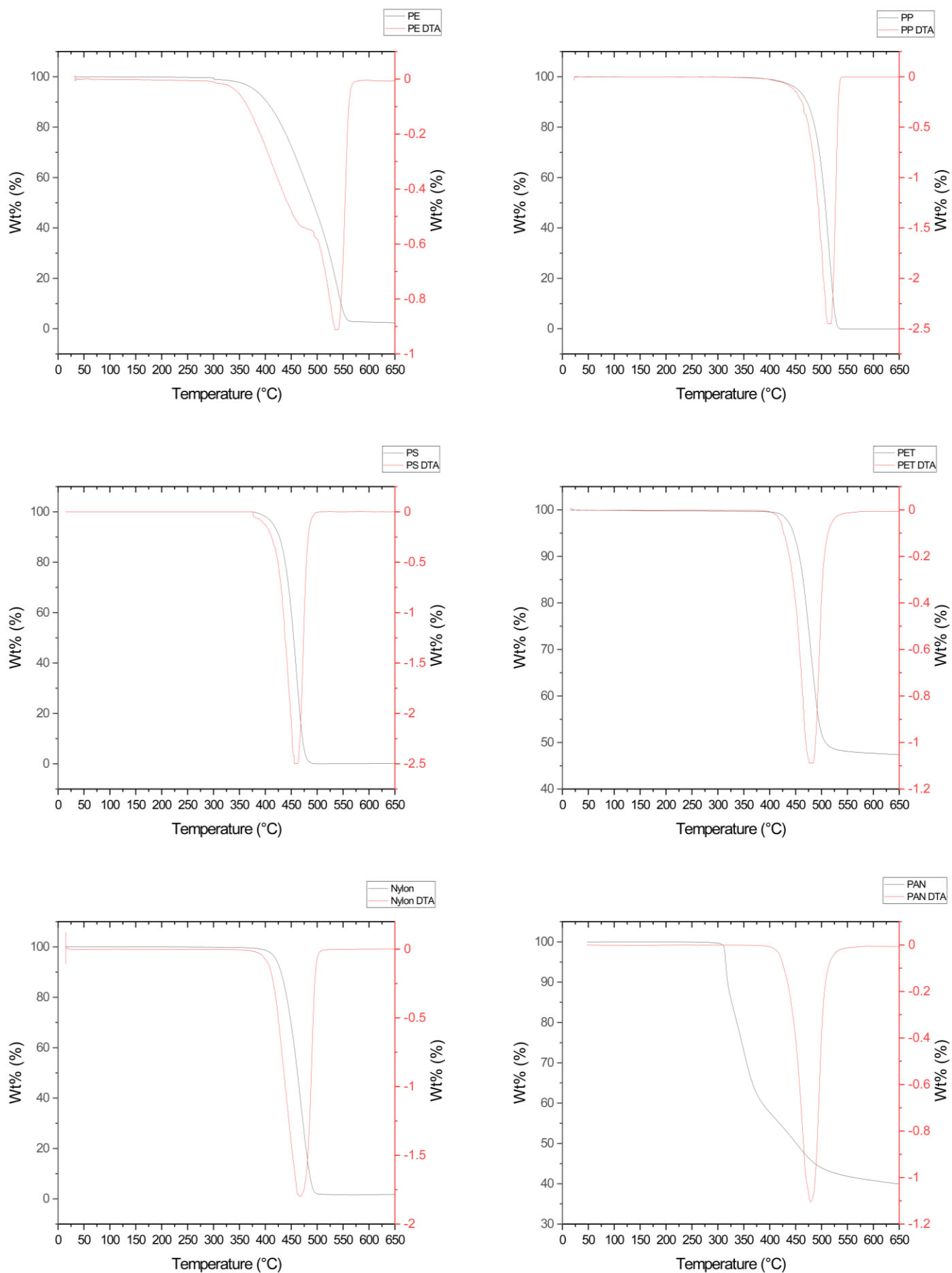


Figure 5.2: TGA/DTG graphs of various plastics.

5.3: Polymer carbonisation

Six examples of waste plastic were carbonised using the designed reactor of Chapter 4. Polyethylene (PE) vaporised from the combustion boat at the centre of the horizontal furnace, but significant deposition was observed at the furnace extremities. This suggests that thermal cracking is taking place in a limited capacity, as the molecular weight of the residue remains high enough to form a powder as it cools. The presence of a carbon residue at the surface of the bubble column suggests that some of this vapour is making its way through the reactor and carbonizing in contact with the LM. Primary thermal decomposition pathways for PE are shown in Figure 5.3. Figure 5.3, and literature proposes an enthalpy of activation of between 193 and 277 kJ mol⁻¹ for these reactions¹⁵⁴, and increases with molecular weight. The range of this decomposition has been attributed to a rate limiting step in the degradation kinetics, however this has yet to be shown experimentally¹⁵⁴.

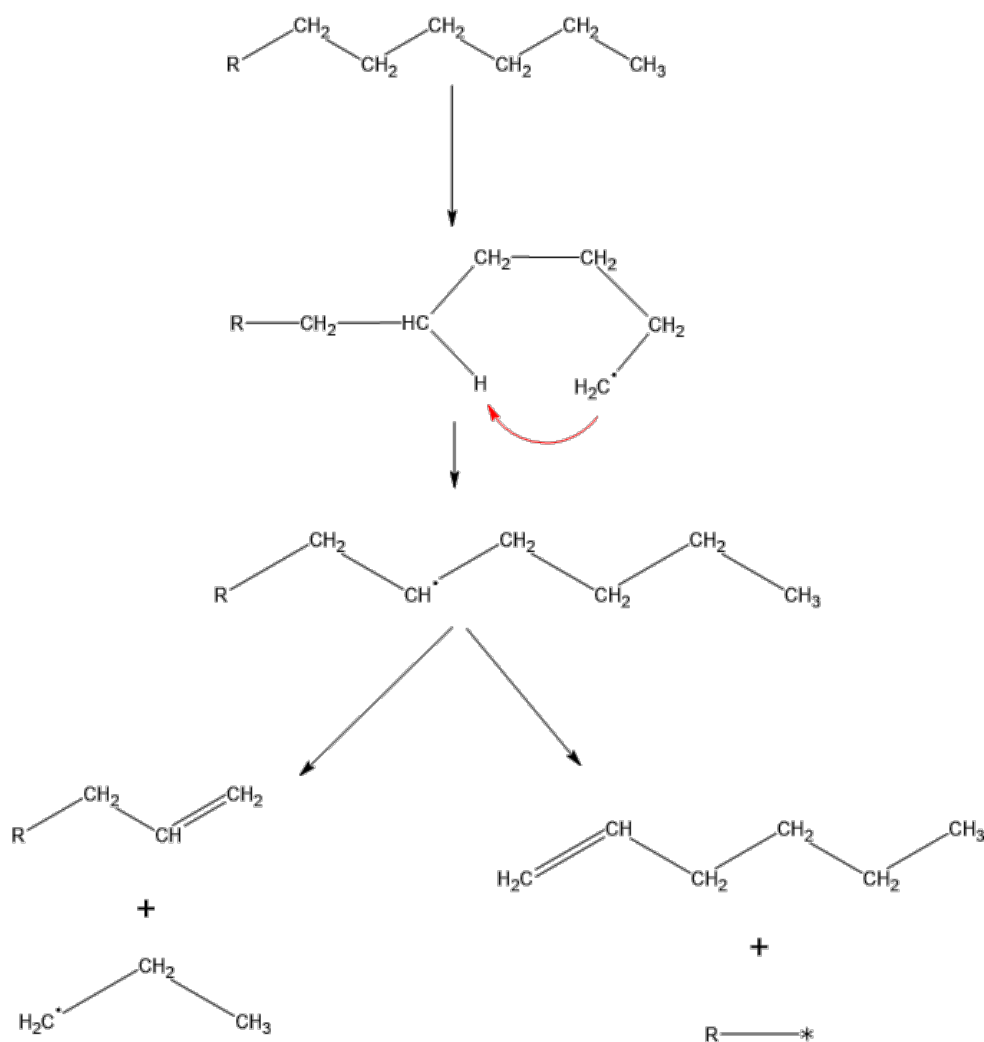


Figure 5.3: Thermal decomposition pathways for polyethylene¹⁵⁴.

Polypropylene (PP) shows no such residue present in the horizontal furnace. Given the relatively high melting point of PP this suggests that thermal cracking is taking place and lighter hydrocarbon fractions are being formed. The current consensus as to the primary decomposition pathways for PP are shown in Figure 5.4. There is however less consensus as to the activation energy of this process, with values being reported from 120 to 260 kJ mol⁻¹¹⁵⁴. This range suggests that kinetics are limited by a rate limiting step, similar to that observed in PE. As the processes are like that of PE, this range is sensible. It is likely the true value lies somewhere towards the middle, and relates to the molecular weight of the PP.

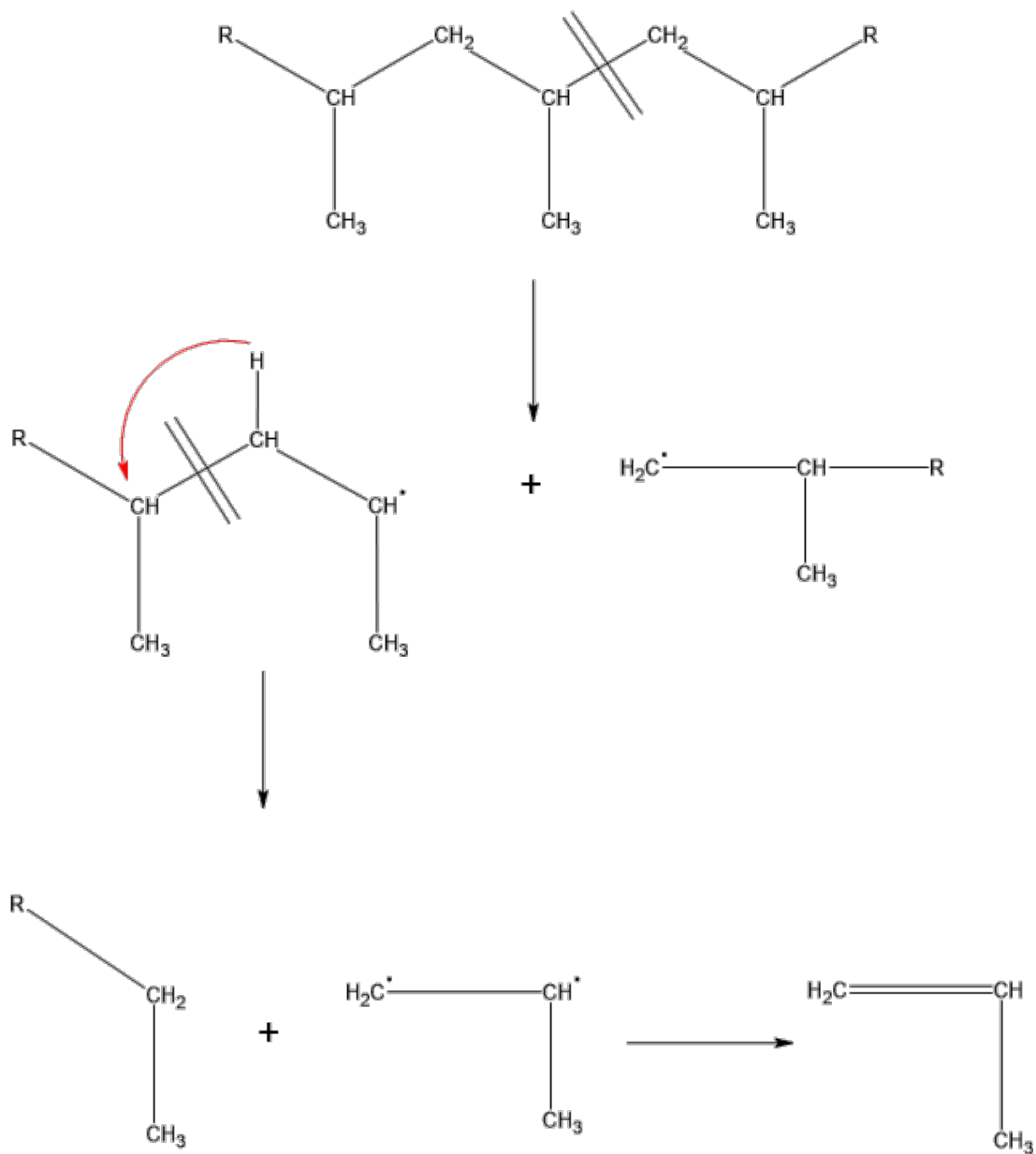


Figure 5.4: Thermal decomposition pathways for polypropylene¹⁵⁴.

Polystyrene (PS) demonstrates a lack of residue in either the horizontal furnace, or bubble column. Based on degradation pathways described in literature¹⁵⁴, pyrolysis of PS is largely a depolymerisation reaction, primarily producing styrene monomers. This can be seen in Figure 5.5. A relatively consistent enthalpy of activation is reported for PS, at $\sim 200 \text{ kJ mol}^{-1}$, suggesting that the degradation kinetics are limited by a single step, being depolymerisation to styrene monomers, and dimers¹⁵⁴. Styrene has a boiling point of 145°C , which is low enough to keep it gaseous all the way through the reactor system. The lack of residue in the bubble column indicates that styrene monomers resist further decomposition by LM and pass through the exhaust line.

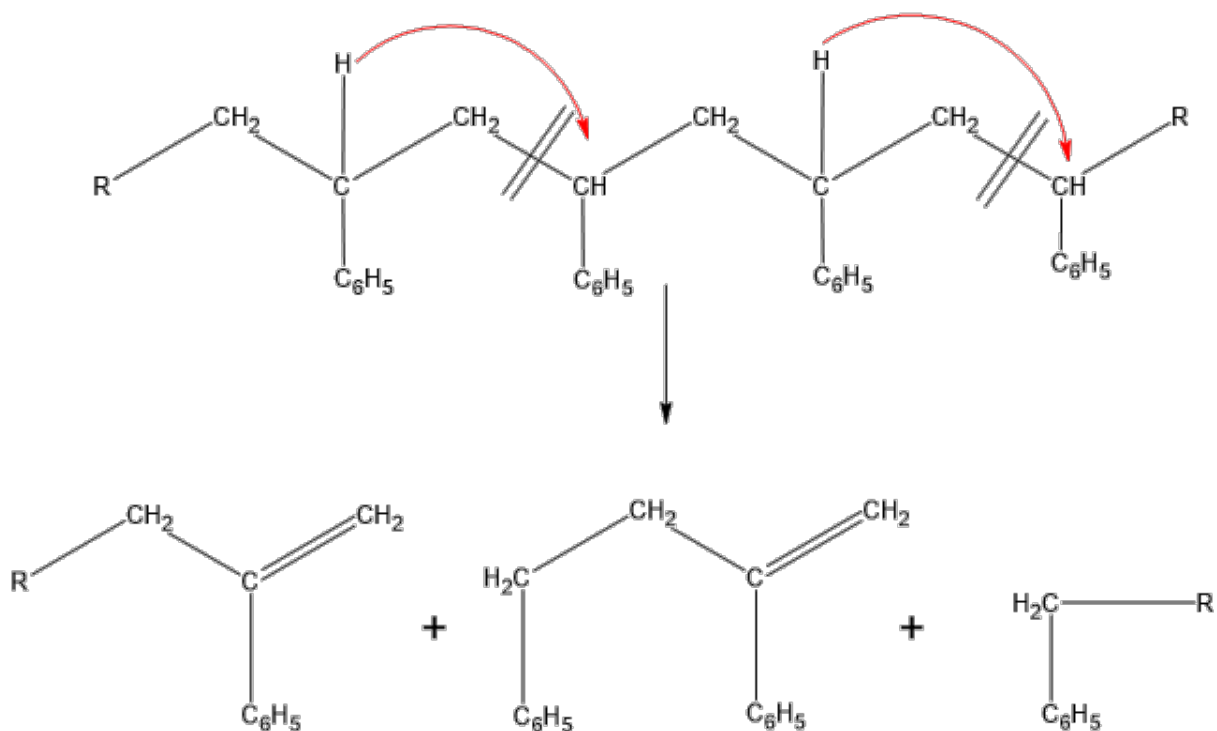


Figure 5.5: Thermal decomposition pathways for polystyrene¹⁵⁴.

Polyethylene terephthalate (PET) exhibits minimal residue in the horizontal tube furnace, and similar conclusions can be drawn to those of PP. LM in the bubble column however exhibited significant oxidation not seen in other polymers. Literature decomposition pathways of PET are extremely complex with many intermediary molecules, however, these pathways generally include several oxidised species¹⁵⁵. Consequentially, it is theorised that the observed LM oxidation is the result of the liberation of oxygen, either from the products of PET thermal decomposition through mechanisms such as the reduction of carbon oxides, or

from the vapourised PET molecules themselves. PET exhibits a similar enthalpy of activation for its decomposition as previously discussed polymers at 227 kJ mol^{-1} ¹⁵⁵.

Polyacrylonitrile (PAN) resulted in the formation of a dark residue in the exhaust of the horizontal furnace, as well as a yellow pyrolysis oil. Enthalpy of activation of PAN decomposition has been reported as 37.6 kJ mol^{-1} , much lower than that of previously discussed polymers¹⁵⁶. Pathways from literature for PAN, which can be seen in Figure 5.6 suggest that the primary products of decomposition are ammonia, hydrogen cyanide, and oligomers of various lengths¹⁵⁷. FTIR of this pyrolysis oil identifies it as being a long alkene, likely pentadecene or nonadecene, suggesting that PAN pyrolysis is liberating nitrogen from the structure, likely in the form of ammonia and cyanides, and then undergoing addition reactions to form longer chain alkenes. This somewhat differs from reported decomposition pathways and may be attributed to the reflux of these products back into the hot zone of the horizontal furnace due to backpressure build-up's, where they may react further with one another to form these compounds. Carbon, as well as pyrolysis oil can be recovered from the bubble column from PAN carbonisation, suggesting some of these decomposition products make their way through the reactor, and are susceptible to carbonisation by LM. However, it is unknown whether this carbon is the result of the carbonisation of the pyrolysis oil, or other products formed from PAN decomposition.

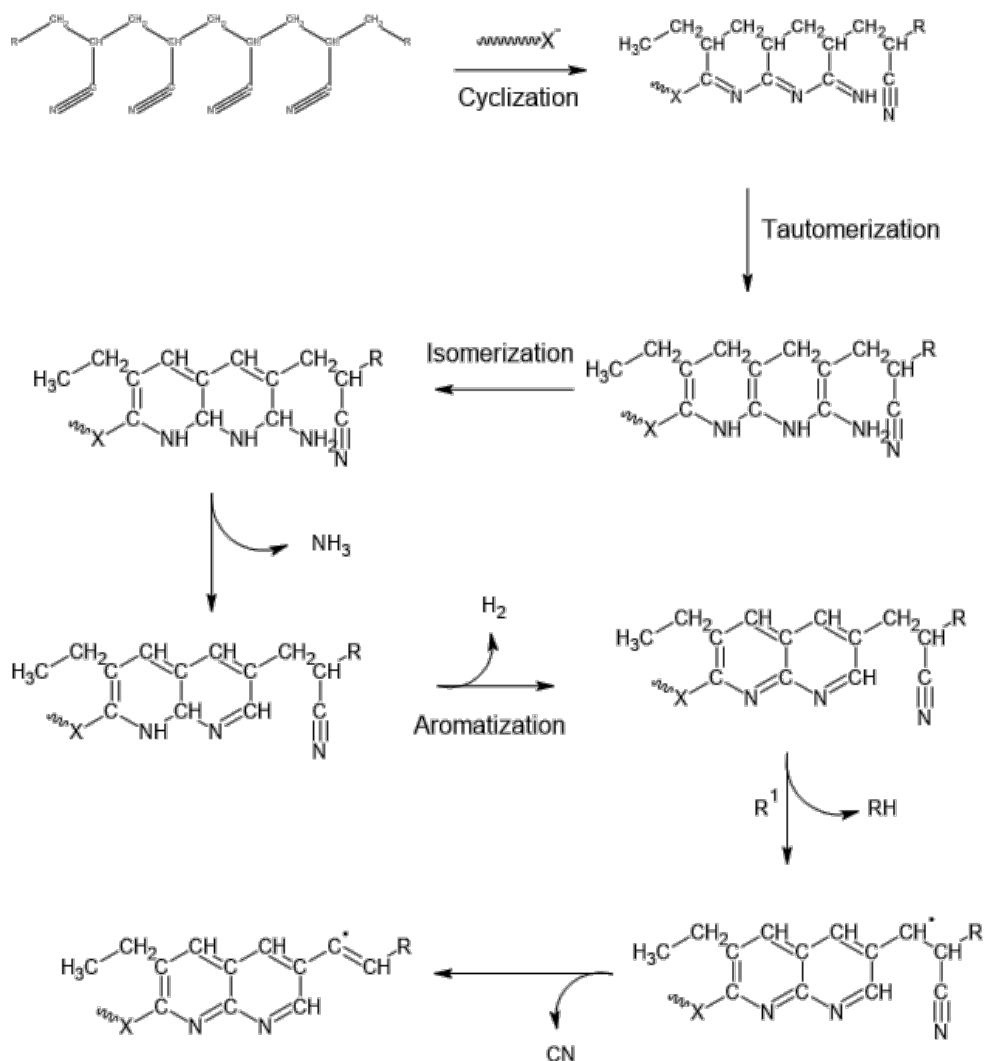


Figure 5.6: Thermal decomposition pathways for polyacrylonitrile¹⁵⁷.

Finally, nylon 6/6 pyrolysis resulted in a thick dark residue in the horizontal tube furnace. Polyamides decompose by pathways outlined in Figure 5.7, with an enthalpy of activation of between 123 and 260 kJ mol^{-1} ¹⁵⁸. Like that of PE and PP, this range suggests a second rate limiting step, in this case the cyclisation between ester bonds. FTIR showed this residue had similarities with nylon II, but with a broader, less resolved peak in the 3300 cm^{-1} region, and a less resolved fingerprint region in general. This may be the result of the production of a pyrolysis oil, which is dissolving condensed nylon and forming a resin. This resulting resin caused exhaust blockages of the horizontal furnace setup, which prevented flow into the bubble column, and as a result very little residue could be recovered. A summary of these results can be seen in Table 5.1.

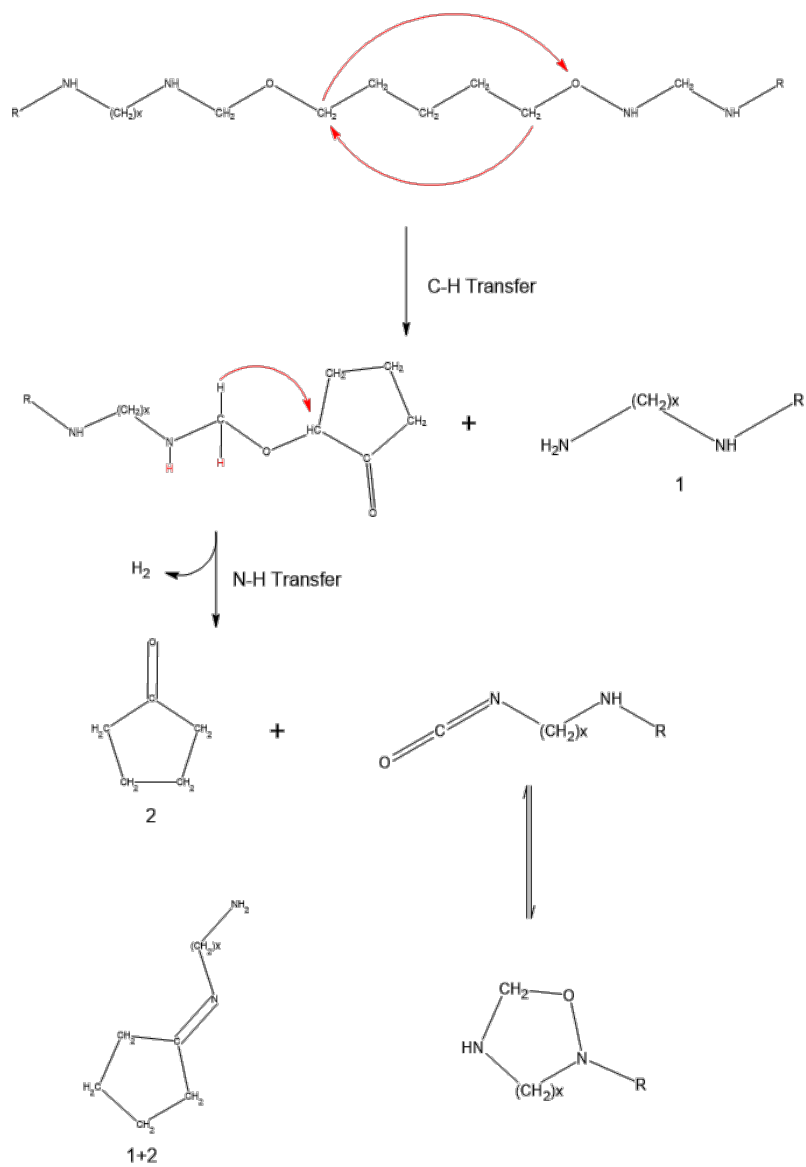


Figure 5.7: Thermal decomposition pathways for polyamides¹⁵⁹.

Table 5.1: A summary of the decomposition mechanisms and products of PE, PP, PS, PET, PAN, and nylon 6/6 from literature, and a brief description of results from this work.

Plastic	Decomposition temperature (°C)	Primary method of decomposition	Primary products of thermal decomposition	A brief description of carbonisation results	Yield wt.%
Polyethylene (PE)	335-450 ¹⁵⁴	Aromatisation, branching, or cross linking, followed by scission at peroxide, carbonyl, chain branch and unsaturated structures ¹⁵⁴ .	Propene, & 1-hexene ¹⁵⁴ .	Significant deposition occurred on the inlet and exhaust extremities of horizontal tube furnace. Residue recovered from bubble column.	6.09±1.69
Polypropylene (PP)	328-410 ¹⁵⁴	Random scission ¹⁵⁴ .	Pentane, 2-methyl-1-pentene, & 2,4-dimethyl-1-heptene ¹⁵⁴ .	No significant observation of solid residue in either horizontal furnace. Residue recovered from bubble column.	6.39±0.89
Polystyrene (PS)	300-400 ¹⁵⁴	Plastic link scission ¹⁵⁴ .	Styrene monomers, dimers and trimers ¹⁵⁴ .	No significant observation of solid residue in either horizontal furnace, or bubble column.	4.12±1.52
Polyethylene Terephthalate (PET)	283-306 ¹⁶⁰	Scission of acetaldehyde groups, and reaction with intermediaries ¹⁶⁰ .	Acetaldehyde, carbon monoxide, carbon dioxide, benzaldehyde, styrene, benzoic acid, phenacyl, p-terphenyl, & 4-biphenylcarboxylic acid ¹⁶⁰ .	Minimal deposition observed. Significant oxidation of LM in bubble column. Solid carbonaceous deposit recovered from cleaning.	7.88±1.29
Polyacrylonitrile (PAN)	>300 ¹⁵⁷	Nitrile group aromatisation, followed by evolution of un-aromatised oligomers ¹⁵⁷ .	Ammonia, & hydrogen cyanide, followed by oligomers ¹⁵⁷ .	Dark residue in horizontal furnace. Carbonaceous product at surface of LM layer in bubble column, along with yellow pyrolysis oil.	7.84±1.56
Nylon 6/6	310-380 ¹⁵⁹	Scission at C-N-C bond, followed by aromatisation and reaction with intermediary radicals ¹⁵⁹ .	trans-4-(Dimethylamino)-3-buten-2-one, H ₂ C=CH=CH-CH ₂ -CO-NH-(CH ₂) ₅ -CN, & H ₂ C=CH-(CH ₂) ₃ -CO-NH-(CH ₂) ₅ -CN ¹⁵⁹	Thick, dark residue at exhaust of horizontal furnace. Little discernible solid residue in bubble column.	1.84±0.86

The thermal decomposition of plastics is highly varied, as are the products of thermal decomposition. This variation only increases in examples of real-world waste, where additives must also be considered. However, the interaction between these products and the LM can all be summarised in similar terms. As shown previously, decomposition of plastics is highly endothermic. LMs retain typical properties of metals by way of a delocalised sea of electrons, which results in LMs showing similar thermal and electrical conductivity properties as seen in solid metals⁹⁹. The consequence of this is their ability to act as a heat transfer medium, as well as an electron donor which assists in the overcoming of activation energies, and then stabilising the resulting products. As molecules become smaller, the effect of steric forces in the kinetics of bond dissociation diminish, and consequentially small hydrocarbons like methane have much higher enthalpies of activation for their decomposition (423 kJ mol^{-1} ¹⁶¹) when compared to the above polymers. As such, heat transfer mediums such as LMs may offer an effective way of overcoming these enthalpies of activation and promote the decomposition of lighter hydrocarbons into their constituent components. It is theorised that this is the mechanism observed in this study, resulting in the production of solid carbon from the products of thermal decomposition of polymers.

5.4: Characterisation of plastic derived carbon materials

5.4.1: Scanning electron microscopy

Scanning electron microscopy (SEM) was employed to investigate the morphology of the products. An example of PE can be seen in Figure 5.8 (a), samples typically show a dispersion of two common morphologies: spheres and clumps. These spheres ranged in size from between 2 and 20 μm , while the clumps are more varied and do not show a consistent pattern of size or shape. These spheres were further determined to be galinstan by EDX and are discussed further in the following Chapters. On close inspection, the clumps consist of smaller granular components, as shown in Figure 5.8 (b). This is consistent with literary examples of amorphous carbon species^{162, 163}. Clumps demonstrated a tendency for charging, under SEM which suggests they are poorly, or non-conductive. At higher magnification (Figure 5.8 (c)), the surface of the galinstan spheres are seen to have these carbon attached. This is likely indicative of an electrostatic attraction between the carbon product and the galinstan resulting from the washing process.

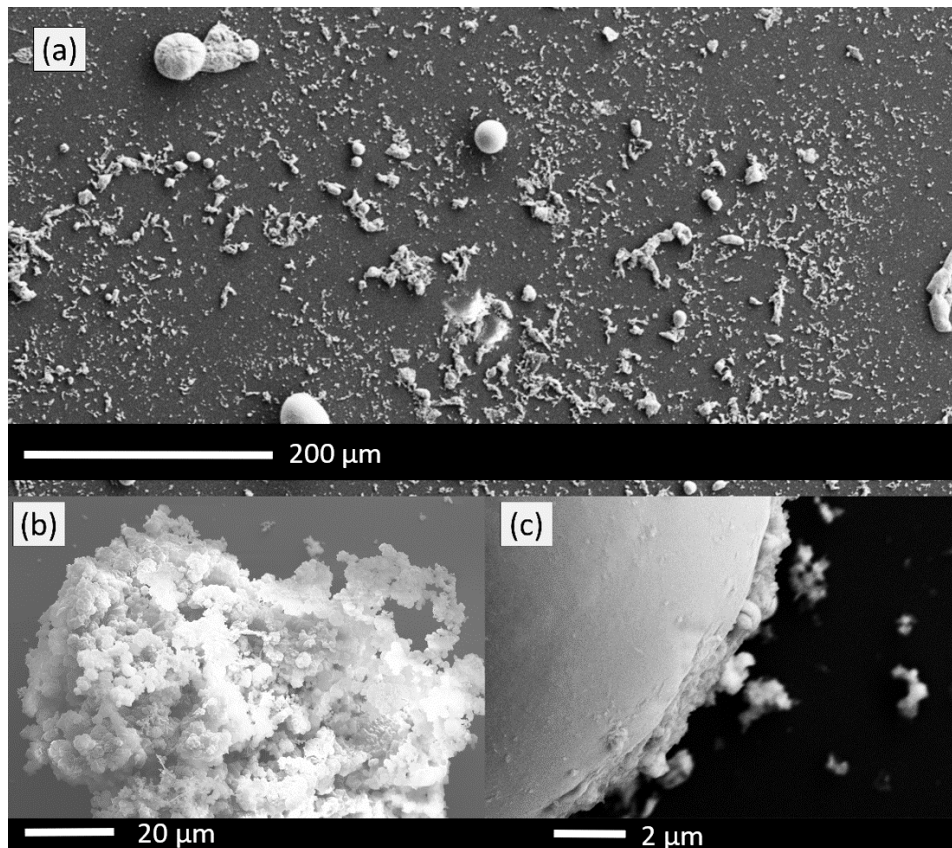


Figure 5.8: SEM images of PE sample showing (a) an overview of morphologies seen, (b) magnified view of the clump morphologies, and (c) a close look of the surface of a sphere morphology.

5.4.2: Energy dispersive X-ray elemental mapping

EDX elemental mapping were used to characterise the distribution of constituent elements in the collected samples. Samples were dispersed in MilliQ water and then affixed to a silicon substrate after drying. This was necessary to avoid the need for carbon tape, which would interfere with EDX results. The result of this method however was a more dispersed distribution of sample. EDX maps in Figure 5.9 and Figure 5.10 show a dispersion of carbon, oxygen and gallium in a PAN derived sample on a large scale, and PET on a small scale. It is important to note that EDX is a surface analysis technique and may not necessarily be representative of the bulk properties of samples. Furthermore, EDX is limited in elements it is capable of detecting and as such nitrogen and hydrogen content of the product are not reported.

Two characteristics are of note in these maps. Firstly, the gallium content of these samples is relatively consistently dispersed, and made up of small spheres, rather than larger clumps as seen in the previous section. This is likely the result of gallium micro and nanodroplets being

formed in the sonicating portion of the sample wash. As discussed in Chapter 2.4.4, LMs may form nanodroplets when a high shear force is applied when in a solution, such as through sonication. This results in samples containing an amount of gallium that is difficult to remove. Secondly, the distribution of oxygen is not strongly correlated to the distribution of carbon in the sample. This suggested that the presence of oxygen is largely unrelated to the presence of oxygen containing hydrocarbons, but more likely the result of surface oxidation of the silicon substrate, as well as, to a lesser extent, the surface of the gallium remaining in sample. In PET samples, this could likely be due to the presence of oxygen in the precursor molecule. However, in non-oxygen containing samples, such as PAN, it may be indicative of oxygen being present in the system. As discussed in Chapter 4.2, despite the reactor being purged with argon, sections of the reactor above the outlet may allow a small amount of lighter atmospheric gasses to remain, rather than being displaced. This may lead to a partial oxidation of the products, even when no endogenous oxygen is present to the plastic precursor.

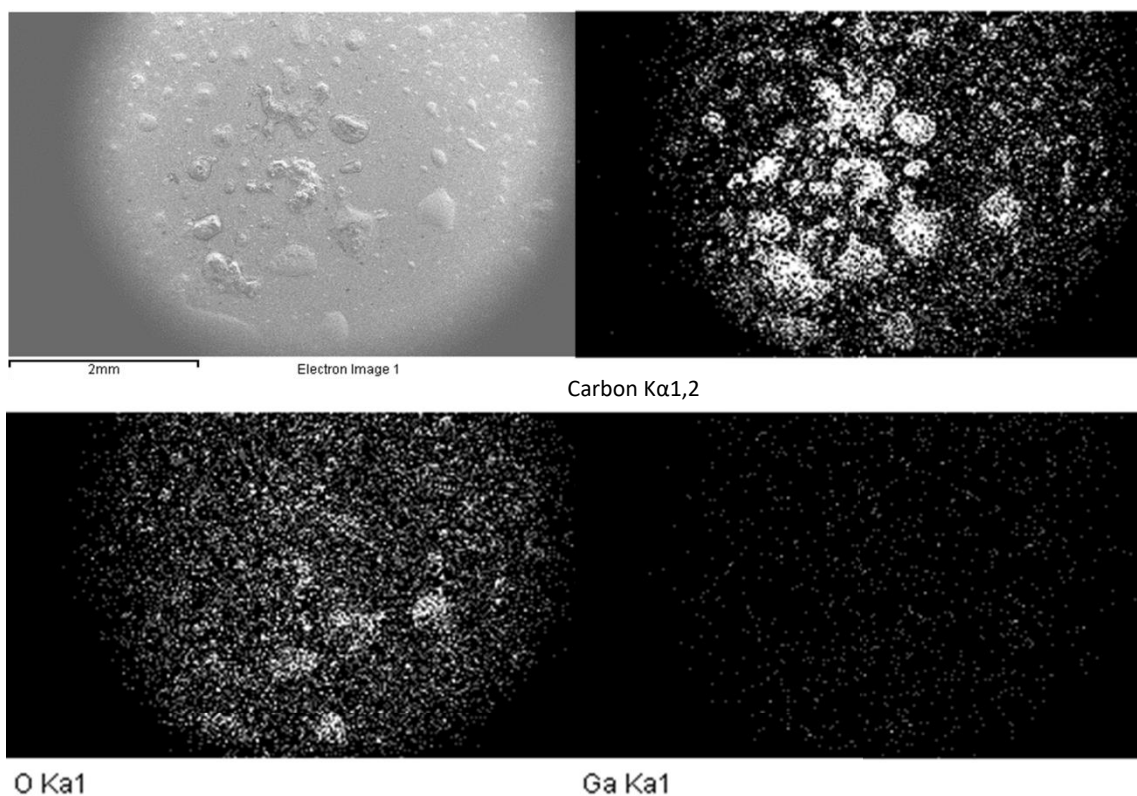


Figure 5.9: SEM image and EDX elemental mapping of a carbonisation sample using a PAN precursor.

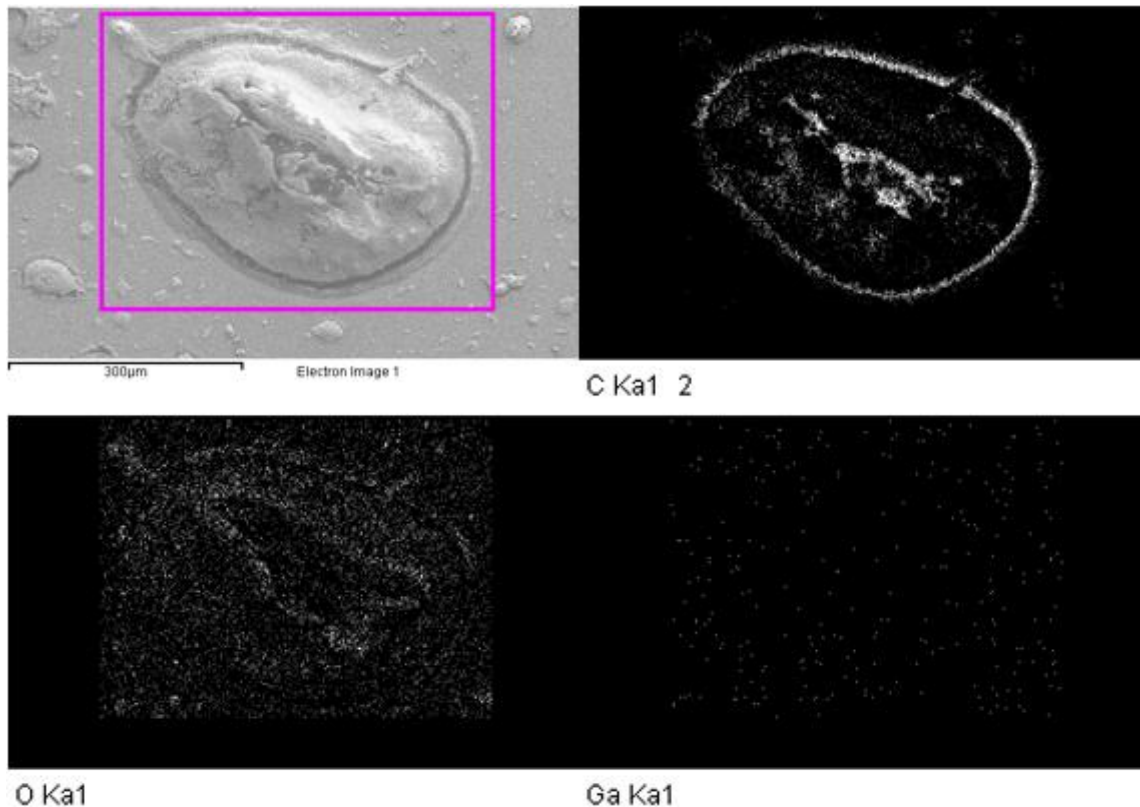


Figure 5.10: SEM image and EDX elemental mapping of a carbonisation sample using a PET precursor.

5.4.3: Energy dispersive X-ray analysis

EDX analysis was used to determine elemental composition of samples. The results can be seen in Table 5.2. Oxygen was consistently present, which likely results from the presence of oxygen in the system above the outlet of the horizontal furnace that could not be purged. The reactor creates positive pressure inside the system between the gas supply and the surface of the bubble column. As a result, a leak is more likely to release gas from the system, rather than allow atmosphere to enter the system. The presence of oxygen to such a high degree may also be the result of additives used in commercial plastics. Plasticisers for example are common additives, and usually exist in a concentration of approximately 10 wt%. They are often non-volatile organic molecules which act to reduce energy barriers between polymer chains and increase flexibility. Examples of commonly used plasticisers all include oxygen in their structure¹⁶⁴. In similarly significant quantities in plastics are fillers. Commonly used to bulk up plastics cheaply and reduce material costs, fillers (most commonly CaCO_3) may comprise up to 20 wt% of a plastic composite¹⁶⁴. This is significant, as thermal decomposition of CaCO_3 results in its decomposition, and the production of CO_2 gas, which may itself be

reduced by the LM to form solid carbon and oxygen gas. As a result, it is important to keep the horizontal tube furnace below $\sim 650^{\circ}\text{C}$ where the majority of this decomposition occurs¹⁶⁵.

Table 5.2: Average EDX analysis of carbon samples from various waste plastics.

Atomic weight percentage of elements present in residue from each respective plastics precursor						
Element	Polyethylene (PE)	Polypropylene (PP)	Polystyrene (PS)	Polyethylene Terephthalate (PET)	Polyacrylonitrile (PAN)	Nylon 6/6
Carbon	88.45 \pm 4.35	56.34 \pm 3.84	26.09 \pm 12.87	45.92 \pm 4.49	67.28 \pm 2.23	10.93 \pm 2.21
Oxygen	10.06 \pm 3.23	43.66 \pm 3.84	48.28 \pm 7.18	50.81 \pm 5.59	23.50 \pm 0.69	67.90 \pm 8.55
Gallium	1.49 \pm 1.13	0.00	21.07 \pm 2.62	3.27 \pm 1.10	9.22 \pm 1.54	21.17 \pm 6.34
Tin	0.00	0.00	4.56 \pm 3.08	0.00	0.00	0.00
C:O ratio	8.79	1.29	0.54	0.90	2.86	0.16

Note: substrate and residual chlorine from washing has been removed.

5.4.4: Raman spectroscopy

Raman spectroscopy was employed to investigate the structure of the synthesised carbon. It can be seen in Figure 5.11 that all samples demonstrated broad D band peaks around 1365 cm^{-1} , and G band peaks around 1590 cm^{-1} . Broadness of the peaks is attributed to inhomogeneous broadening resulting from a heterogeneous makeup of graphitic and amorphous carbons, as well as the presence of other potential impurities. The D band peak is typically associated with defects in a carbon lattice as a result of carbon atoms with dangling bonds near the K point of the Brillouin zone^{56, 140}. G band peaks are associated with aromatic ring chain vibrations between carbon bonds and result from E_{g2} mode from sp^2 -bonded carbon atoms in a graphitic layer⁵⁶. Furthermore, on closer inspection, shoulders off the main D and G band peaks are clearly visible.

Amorphous carbons and chars typically exhibit a particularly complex Raman spectra as a result of their nonuniform lattice, the complicated nature of precursor materials, and the method of their formation¹⁴¹. Computational simulations of various polyaromatic hydrocarbons have provided an insight into the lattice features which give rise to these

shoulders¹⁴² which can be seen in the deconvolution in Figure 5.11(b)-(f). Smith et al identify ten distinct peaks within the Raman spectra of amorphous chars. A summary of their findings can be seen in Table 5.3.

Table 5.3: Summary of peak assignments for amorphous carbon chars¹⁴².

Position (cm ⁻¹)	Peak Label	Shape	Assignment
975– 1075	S _L	Gaussian	Breathing modes for small aromatic regions, secondary breathing mode for 7+ membered ring
1150– 1200	S	Gaussian	Breathing mode for rings containing 7+ carbons with Kekulé modes in adjacent benzene rings, benzene ring breathing modes adjacent to heteroatom defects
1250– 1300	D _S	Gaussian	Assorted breathing modes for most PAHs
1340– 1380	D	Gaussian	Combined breathing/Kekulé vibrations for PAHs. Larger more symmetric systems show peaks near 1350 cm ⁻¹ , while peaks for smaller systems move towards 1400 cm ⁻¹
1400– 1460	A ₁	Gaussian	Breathing mode for 5-membered rings with Kekulé vibrations in adjacent 6-membered rings and near pure Kekulé in small ring systems and moieties
1480– 1550	A ₂	Gaussian	Mixed breathing and asymmetric stretch vibrational modes for sp ² carbons near defects causing out of plane deformation. Heteroatom defects tend to cause greater red shift
1570– 1600	G _G	Gaussian	Distributed asymmetric vibrations for distribution of small PAHs
1570– 1600	G _L	Lorentzian	Standard E _{2g} mode for large PAHs
1605– 1650	D'	Gaussian	Double resonance activated breathing mode
1750– 1800	C	Gaussian	Carbonyl stretching mode, very weak

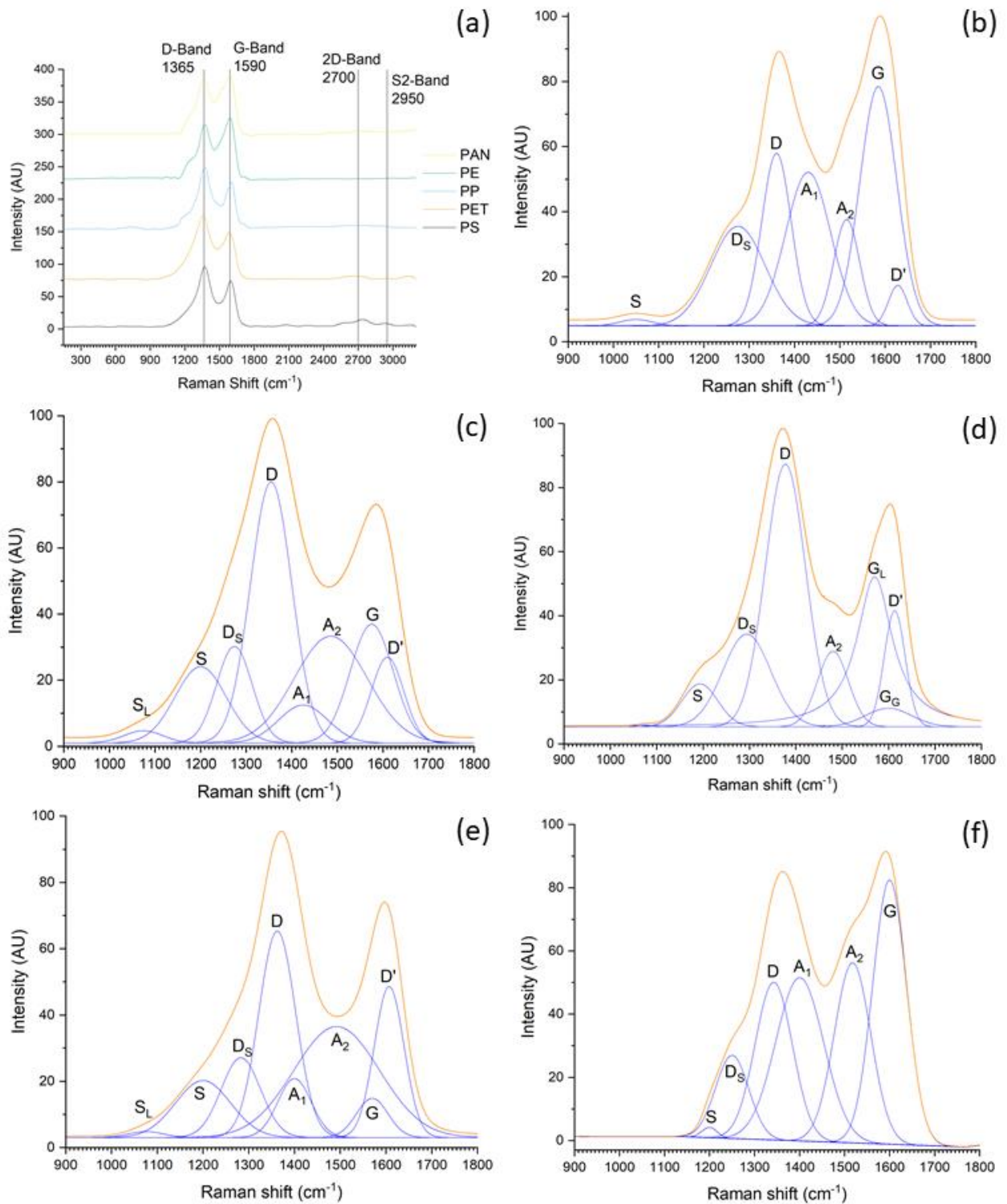


Figure 5.11: (a) Raman spectra of carbonaceous samples produced from several waste polymers. An example of Smith et al. deconvolution method¹⁴² applied to (b) polyethylene, (c) polyethylene terephthalate, (d) polypropylene, (e) polystyrene, and (f) polyacrylonitrile derived carbon respectively.

Raman spectra from this work exhibit examples of many of these assignments. Representative examples of deconvolution can be seen in Figure 5.11(b)-(f) which were performed on the spectra of polyethylene, polyethylene terephthalate, polypropylene, polystyrene, and polyacrylonitrile derived carbons. Deconvolution was performed using the Levenberg Marquardt algorithm with a gaussian model and the resulting coefficients of determination (R^2) can be seen in Table 5.4. Deconvolutions were chosen based on the highest R^2 values obtained.

Table 5.4: A summary of R^2 values of Raman curve fitting from Figure 5.11.

Polymer precursor	Coefficient of determination (R^2)	Number of peaks identified
Polyethylene (PE)	0.99779	7
Polyethylene terephthalate (PET)	0.99638	8
Polypropylene (PP)	0.99904	7
Polystyrene (PS)	0.99993	8
Polyacrylonitrile (PAN)	0.99981	6

Shoulder band, low (S_L) is the product of weak breathing modes for small aromatic regions. These are ascribed to hydrogen motion along the carbon edge and are typically weak compared to other vibrations in the spectrum¹⁴². S_L is also associated with a secondary breathing mode for 7+ membered rings¹⁴³, as well as specifically with naphthalene. However, these vibrations are described as being stronger relative to the rest of the spectrum¹⁴². As such, it is unlikely that the S_L peaks in polyethylene derived carbon (PEDC), polyethylene terephthalate derived carbon (PETDC), or polystyrene derived carbon (PSDC) spectra are the result of any significant presence of 7+ member rings, or naphthalene species. They are likely to arise from small aromatic regions in the samples. Polypropylene derived carbon (PPDC), and polyacrylonitrile derived carbon (PANDC) samples did not yield any significant S_L peaks. This indicates that not only do these samples not contain 7+ member ring systems or naphthalene species, but are also lacking in small aromatic regions, suggesting a larger degree of graphitisation. This is corroborated by the relatively high G:D band ratios of these samples seen in Figure 5.13.

Shoulder band (S) is described as the product of primary breathing modes for 7+ member rings¹⁴³ and benzene rings adjacent to heteroatom defects¹⁴². This band is not present in the PEDC spectrum. The absence of primary breathing modes for 7+ member rings reinforces the

above conclusions that S_L is the product of breathing modes for small aromatic regions in the PEDC sample. Furthermore, the lack of heteroatoms in the PEDC system would not allow for the formation of heteroatom defects in the carbon product. The S band is present alongside the S_L band in both PETDC and PSDC. Given that both PET and PS as precursors contain aromatic rings in their structure, it is theorised that the presence of these bands in their carbon products are related to this precursor structure. Their presence in PETDC may be the result of heteroatom defects as a result of the oxygen present in the system, however no such explanation exists for PSDC. Therefore, it is more likely that these two bands indicate the presence of 7+ member rings in these two samples.

PPDC and PANDC both exhibit S bands without the presence of S_L bands. In the PANDC sample, this S band is small relative to other bands and likely indicates a small amount of nitrogen in the carbon structure which is carried over from the structure of the PAN precursor. However, an S band without the presence of an S_L band is unexpected in the PPDC sample. It is hypothesised that this is related to issues taking spectra with such low sample yields. The deconvolution of PPDC shows an anomaly in the baseline below 1075 cm^{-1} Raman shift. The small amounts of sample from which these spectra were taken, baselining of the data, and the subsequent Savitzky-Golay smoothing necessary for deconvolution likely played a part in masking the already weak S_L peak in the sample. It is therefore likely that this peak is present, but not visible in the spectrum.

Defect band, shoulder and defect band (D_S and D respectively) are both present in all samples. The defect bands are of primary interest in the Raman characterisation of carbons, alongside the graphitic bands discussed later. D_S is the result of assorted breathing modes for polyaromatic hydrocarbons (PAHs), while D is the combined breathing and Kekulé vibrations for PAHs. In highly ordered systems, a double resonance effect, coupled with degeneracy intensifies the D band peak¹⁴⁴. In less ordered systems, coupling of breathing and Kekulé modes results in the D band being blue shifted from the expected 1350 cm^{-1} ¹⁴². This further differentiates the D and D_S bands, resulting in a more pronounced shoulder. As such, particularly prominent shoulders are seen in PEDC and PANDC, while PETDC, PPDC, and PSDC give less prominent shoulders. This suggests a higher degree of order is produced in the carbon lattice when derived from polyethylene terephthalate, polypropylene, and polystyrene when compared with that of polyethylene or polyacrylonitrile precursors.

Literature on the origin of the amorphous bands (A_1 and A_2) is lacking in consensus. However, agreement exists suggesting they originate from the presence of irregular structures^{145, 146}. Smith et al.¹⁴² identified two distinct amorphous bands with origins in different sources. A_1 , found between 1400 and 1460 cm^{-1} , is ascribed to the Kekulé vibrations coupled to symmetric breathing of adjacent cyclopentane rings and is strongly associated with out of plane deformation around these defects.

A_2 is found between 1500 and 1550 cm^{-1} and is primarily the result of point defects which give rise to asymmetric stretching and breathing modes in nearby ring systems. Secondarily, A_2 may also arise from nearby oxygen defects which restrict the asymmetric stretch modes and result in the A_2 peak being red shifted¹⁴². In all spectra, both A_1 and A_2 are present. This suggests the presence of cyclopentane rings in the carbon structures, as well as point defects with surrounding sp^2 carbons. The origin of these point defects making up the A_2 bands however is likely to fall into two categories based on the sample's precursors. Endogenous heteroatom defects are likely present in samples whose precursors contained oxygen or nitrogen species which may be incorporated into the final structure of the product. Alternatively, point defects may occur from the desultory assembly of precursor material giving rise to homoatom defects where the lattice uniformity is degraded due to uncharacteristic bonding. This explains the observation that precursor materials containing oxygen or nitrogen species yield carbon samples with higher area A_2 bands than those produced from pure hydrocarbons.

The G-bands, like the D-bands, are peaks of primary interest in the Raman characterisation of carbons. They are well studied, and strongly associated with the asymmetric stretch of sp^2 carbons, particularly E_{2g} stretching in aromatic rings. While E_{2g} stretching is present in an array of molecules, the overall system symmetry has a large effect on the area and intensity of the G-band peaks. As a result of the complexity of the makeup of the G-band region, it can be theoretically broken up into a Gaussian and Lorentzian model to describe PAH cluster sizes, system symmetry, and the effects of defects¹⁴². The Gaussian model is assigned to the distribution of small PAH structures, while the Lorentzian model is assigned to large PAH structures. However, in all the spectra, attempts at separating these G-band components consistently yielded a lower coefficient of determination. As such, differentiation could not be achieved, and the G-band was left as a single peak. This is likely a result of working with

low yields as signal to noise ratios were quite high and the Savitzky-Golay smoothing necessary for deconvolution likely masked the ability to differentiate these peaks. However, the generally high areas and relatively low intensities of all samples does suggest that they consist primarily of small PAH structures, rather than being a larger, symmetric system which would give a more intense, but lower area peak. This is discussed further later in this Chapter.

In Smith et al.'s¹⁴² study, a D' band was proposed. It is assigned to the weak breathing mode of a central ring surrounded by asymmetric stretching behaviour. This band was only shown to be significant in coronene and cycloheptene centred ring systems. The D' band was extracted from all samples except PANDC. For the PEDC and PPDC samples the band was as expected and weak relative to other bands. PETDC and PSDC samples however yielded significantly stronger D' peaks.

Finally, the presence of carbonyl stretching can lead to a very weak band appearing in between 1750 and 1800 cm^{-1} ¹⁴². In the plastic derived carbon samples, no such band was observed. This is to be expected in PEDC, PPDC, and PANDC as they do not contain oxygen atoms, preventing the formation of carbonyl groups. The lack of carbonyl stretching in PETDC and PSDC samples is likely indicative of their being too weak to detect.

Based on the above analysis of plastic derived carbon samples, proposed structures are presented in Figure 5.12. For systems with no endogenous heteroatoms, the structure in Figure 5.12(a) is proposed. It consists of small groups of PAHs, connected by carbon chains to create a greater superstructure. The presence of various types of cycloheptane rings are also shown, both as carbon edges, and centre groups which give rise to out of plane deformations. It is believed that this is representative of carbonaceous products formed at low temperatures in liquid metal reaction environments from waste plastic precursors. Figure 5.12(b) is proposed as representing systems containing endogenous heteroatoms. Many of the same features are shared between (a) and (b), however (b) also contains heteroatom defects as described by the above deconvoluted peaks assignment.

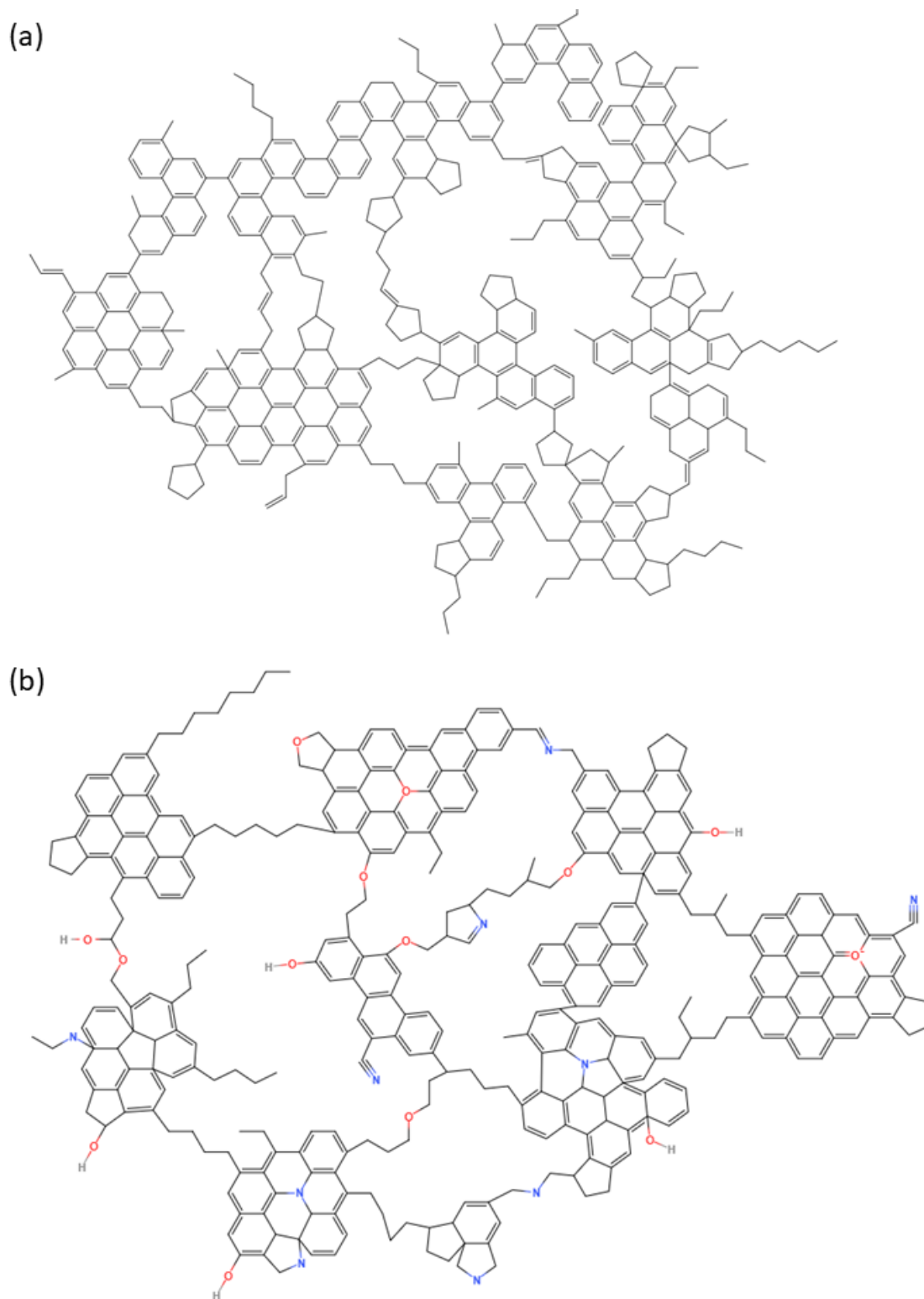


Figure 5.12: A proposed structural example of plastic derived carbon from systems (a) with pure hydrocarbon precursors & (b) precursors with endogenous heteroatoms.

The ratios of intensity between G and D bands give insight into the degree of defects of a graphitic lattice¹⁴⁰. Intensity is chosen over area or width as the desired outcome is to show the degree of graphitisation. Due to the nature and origin of the D band, namely being related

to defects produced by the combined breathing and Kekulé vibrations for polyaromatic hydrocarbons, it has a quite broad shape. This is antithetical to the nature of the G band which is narrower due to its origin in the distributed asymmetric vibrations and E_{2g} modes of polyaromatic hydrocarbons. As such, areas of the G band are significantly decreased in more graphitized samples due to the narrowing of the band, while the D band will remain broad. As a result, area ratios between the two do not represent the degree of graphitization that is trying to be shown.

The resulting averaged $I_G:I_D$ ratios for samples are displayed in Figure 5.13. It was determined that PEDC and PANDC produced the highest G:D band ratios, indicating lowest degree of defects compared to their degree of graphitization. PETDC and PPDC yielded similar ratios, being around 0.5 and 0.6 respectively. PSDC demonstrated the lowest degree of graphitization, with a G:D ratio of 0.2.

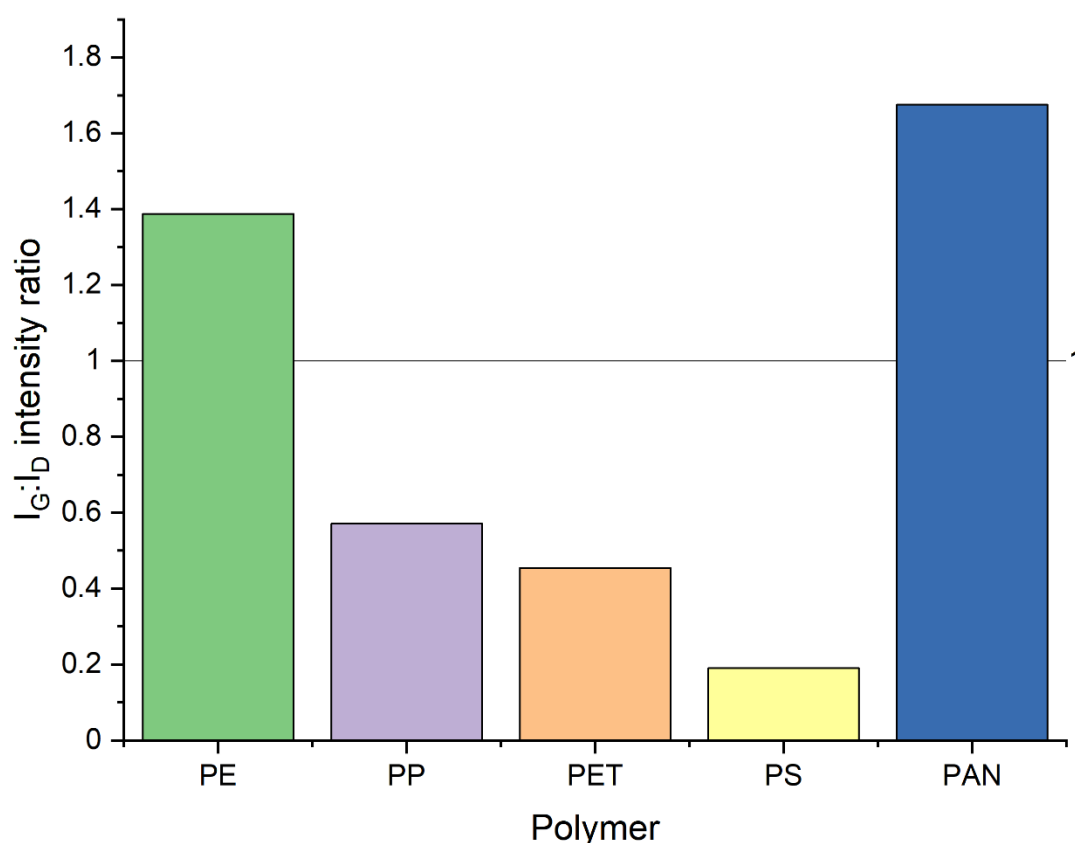


Figure 5.13: A chart of deconvoluted intensity ratios between G and D bands for various polymer precursors.

5.4.5: X-ray photoelectron spectroscopy

X-Ray photoelectron spectroscopy (XPS) was employed to analyse the surface components of the synthesised carbons as well as the nature of the chemical bonds present. The samples exhibited broadening and asymmetry of the singular C1s peak which cannot be ascribed to the core hole effect, or gaussian broadening¹⁶⁶. As such, other components must be responsible for this feature of the spectra. The figures reported have been deconvoluted according to peak assignments by Levi et al.¹⁶⁶.

General trends show that the samples consist of similar components (carbon and oxygen) and bonds, but in varying proportions. It should be noted however that carbon chars tend to chemisorb surface oxygens at low temperatures¹⁶⁶. However, at room temperature, these effects are minimal. As such, a small degree of surface oxygen species may not be indicative of the plastics interaction with the liquid metal, or oxygen impurities in the system, but rather from atmospheric chemisorption post-carbonisation.

Table 5.5 shows the wide scan results for representative spectra of the various plastic derived carbon samples. Results are as expected if oxygen which is endogenous to the plastic precursor is being incorporated into the POGC structure, with the only oxygen containing plastic, PET, demonstrating significantly more oxygen content than other samples. However, given the system was purged with argon before carbonisation, and was operating under constant positive pressure, the presence of oxygen in POGC from plastic samples without endogenous oxygen is unexpected. This is likely the result of a combination of factors.

Table 5.5: Atomic percentages of surface oxygen from various plastic derived carbons as determined by XPS wide scan.

Plastic precursor	Carbon (at.%)	Oxygen (at.%)
Polyethylene	93.46	6.54
Polypropylene	90.91	9.09
Polyethylene Terephthalate	76.28	23.72
Polystyrene	86.11	13.89
Polyacrylonitrile	83.37	16.63

Firstly, as mentioned above, carbon chars tend to chemisorb small amounts of surface oxygen under atmospheric conditions. Given XPS is a surface analysis technique, the surface oxidation may not be entirely representative of the bulk oxidation because of chemisorption. Secondly,

due to the custom nature of the reactor, it could not be purged from the highest point in the quartz tube. As such, heavier argon gas may have simply displaced the atmosphere in the quartz tube up until the level of the outlet port leaving an amount of oxygen in the top half of the tube. At the higher reaction temperatures during carbonisation, partial oxidation may have occurred to the plastic vapours before interaction with the liquid metal. Lastly, while the reactor is under positive pressure up until the liquid metal, a neutral pressure exists after the liquid metal bubble column. Some oxidation may occur at this point as it is sat at a high temperature under atmospheric pressure with only a flow of argon to keep the system inert. Oxygen may enter the system to some extent at this point. Intrinsically, the current reactor design cannot be entirely sealed to oxygen contamination. However, oxygen endogenous to the precursor seems to have more of an effect on the POGC product than oxygen contaminants within the system, as demonstrated by the PET sample.

Figure 5.14, Figure 5.15, Figure 5.16, Figure 5.17, and Figure 5.18 show the high resolution C1s and O1s spectra and peak assignments of PEDC, PPDC, PETDC, PSDC, and PANDC respectively. The red and black lines represent the experimental curves, and deconvolution best fit respectively. The primary peak at 284.5 eV represents aliphatic and aromatic sp^2 bonded carbon species, and corroborates the Raman analysis confirming the presence of aromatic regions of the POGC. The asymmetry and broadening of the experimental curve could not be deconvoluted using only one peak, and so peak assignments and deconvolution were performed in such a way as to achieve the lowest possible coefficient of determination between the line of best fit and the experimental curve.

In Figure 5.14, PEDC exhibited three types of carbon species, as well as a small degree of oxidation. An atomic ratio of $\sim 2:1$ existed between the sp^2 and sp^3 carbons respectively, suggesting a higher degree of carbon double bonds when compared to carbon single bonds. This again is in agreement with the Raman results, as the spectra suggest small aromatic regions, connected by aliphatic chains which would necessitate a higher atomic percentage of sp^2 carbons compared to sp^3 carbons. Furthermore, a small degree of carbon vacancies exists within the POGC, likely relating to unoccupied carbons within out of plane deformations. This is theorised to be due to the deformations creating steric effects surrounding carbon vacancy, making them thermodynamically unfavourable to occupy.

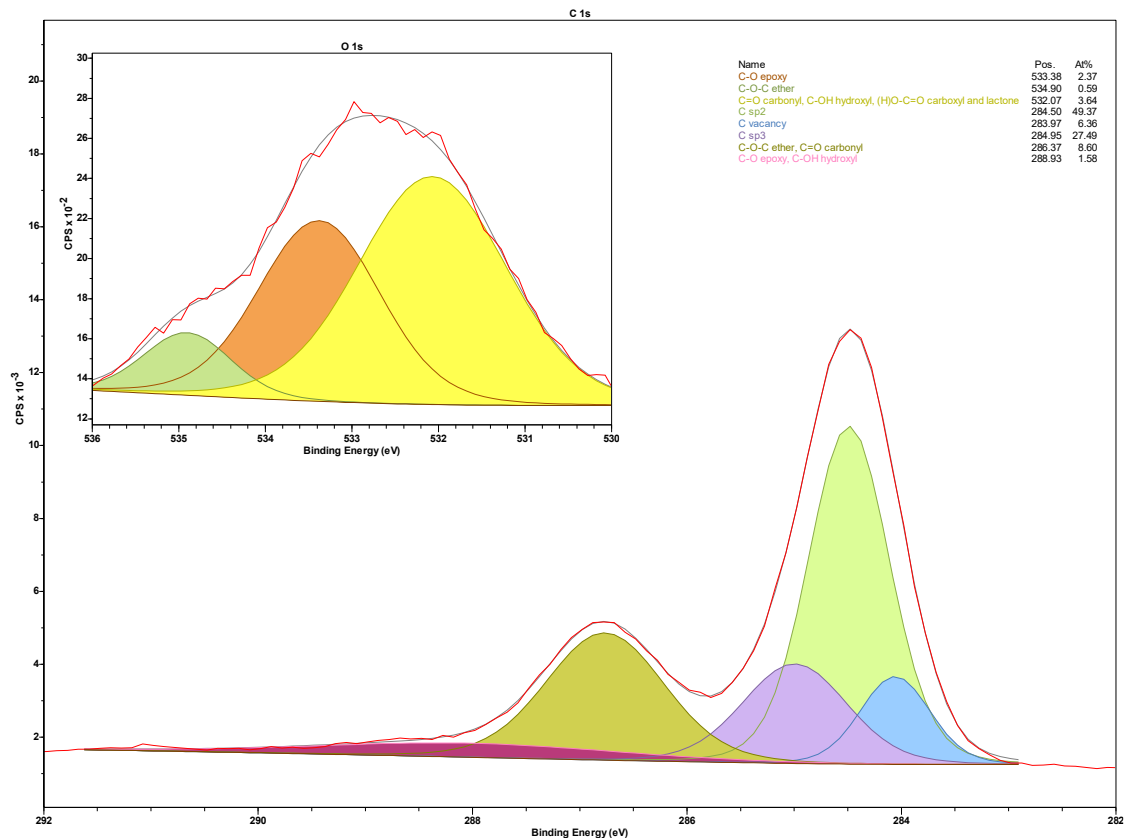


Figure 5.14: High resolution C1s and O1s spectra of polyethylene derived carbon.

Spectra were calibrated around the sp^2 carbon at 284.5 eV and all other peaks were shifted accordingly. The O1s spectra was broad, with a small shoulder. The primary peak at 532.07 eV is associated with photoelectrons from an carbon-oxygen sources (carbonyl, hydroxyl, carboxyl, and lactone)^{167, 168}. Additionally, a smaller epoxy peak exists at 533.38 eV, as well as a shoulder representing ether bonds at 534.90 eV¹⁶⁶. The O1s spectra of the sample primarily differentiates between the ether and carbonyl bonds present in the C1s spectra. The results suggest a primary favouring towards carbonyl bonds in the structure, with a minor ether component.

Figure 5.15 shows the C1s and O1s spectra of PPDC. It exhibits a higher degree of sp^2 bonding compared to that of PEDC. An atomic ratio of $\sim 3:1$ exists between sp^2 and sp^3 carbons respectively. However, the overall at% of sp^2 bonds remain similar. This indicates a lower proportion of sp^3 carbon bonds, rather than a higher proportion of sp^2 carbon bonds when compared to PEDC. These bonds are instead replaced by a higher proportion of various carbon oxygen bonds. Carbon vacancies remain comparable by at%. This suggests that sp^2 bond formation is the preferable modality of charring of the plastic in the liquid metal, while sp^3

bond formation may be substituted with other the formation of other bonds, depending on factors such as oxygen content, or the polymer fractions present from the cracking of the plastic precursor. Carbon vacancies remaining comparable suggests a similar degree of out of plane deformations. The O1s spectrum shows similar trends to PEDC samples. There is a similar favour towards carbonyl bonds over ether bonds, as well as the strong presence of epoxy bond formation.

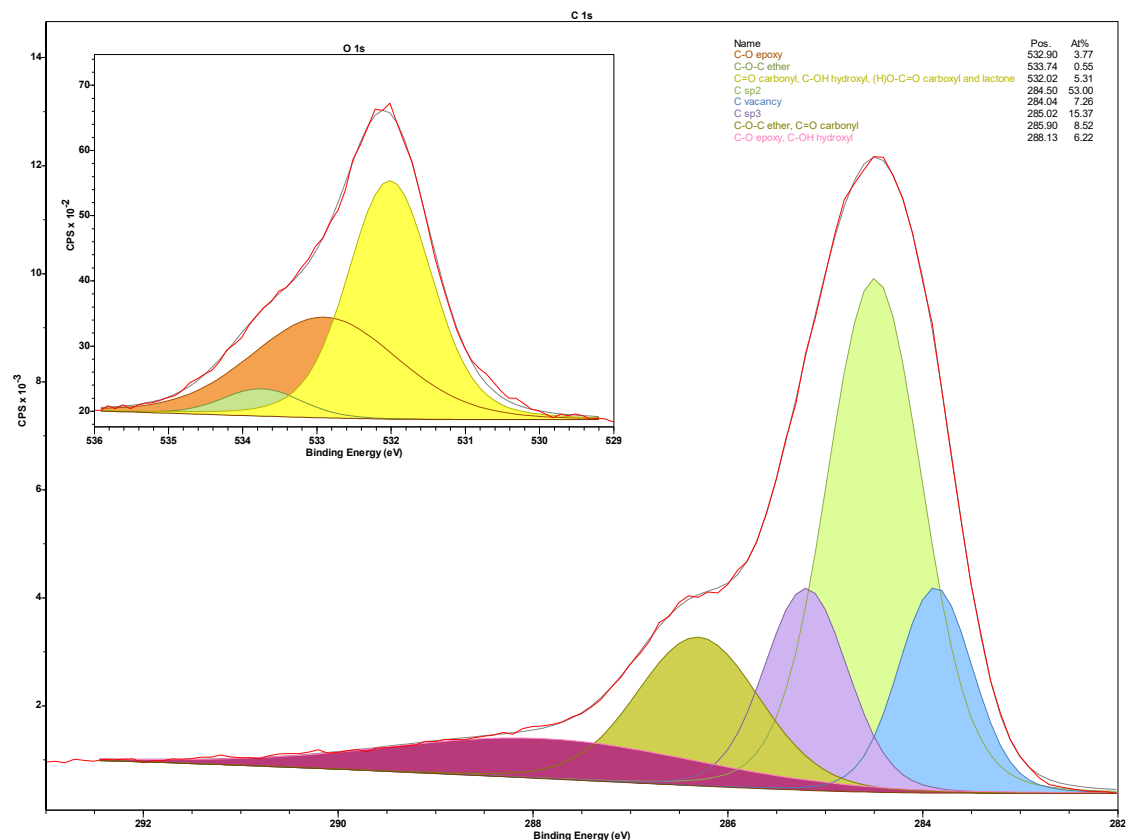


Figure 5.15: High resolution C1s and O1s spectra of polypropylene derived carbon.

Figure 5.16 follows the same trend with a strong preference for sp^2 carbon formation. Despite a much higher degree of oxidation as a result of endogenous oxygen in the polyethylene terephthalate precursor material, sp^2 bonded carbon still makes up ~ 50 at% of the bonds and remains comparable with other samples. The ratio of sp^2 to sp^3 carbons is $\sim 3:1$. Again, this follows the trend of sp^2 being the preferable modality of carbonisation with sp^3 being diminished in favour of other bonding. Carbon vacancies increased significantly, from ~ 6 at% in PEDC and PPDC to ~ 12 at% in PETDC. This is in line with the Raman results where we see a much larger A_2 peak compared to PEDC and PPDC, representing a significant degree of out of plane deformations in the POGC structure. As a further consequence of the endogenous

oxygen, PETDC samples show the most deviation from their O1s spectra. Samples give a strong peak at 532.85 eV, indicating a favour towards the formation of epoxy species (17.37 at%). Ether and carbonyl peaks remain relatively comparable to other samples at 2.89 and 3.48 at% respectively. This suggests that there is a limiting factor in the formation of these types of bonds that epoxy bond formation does not have.

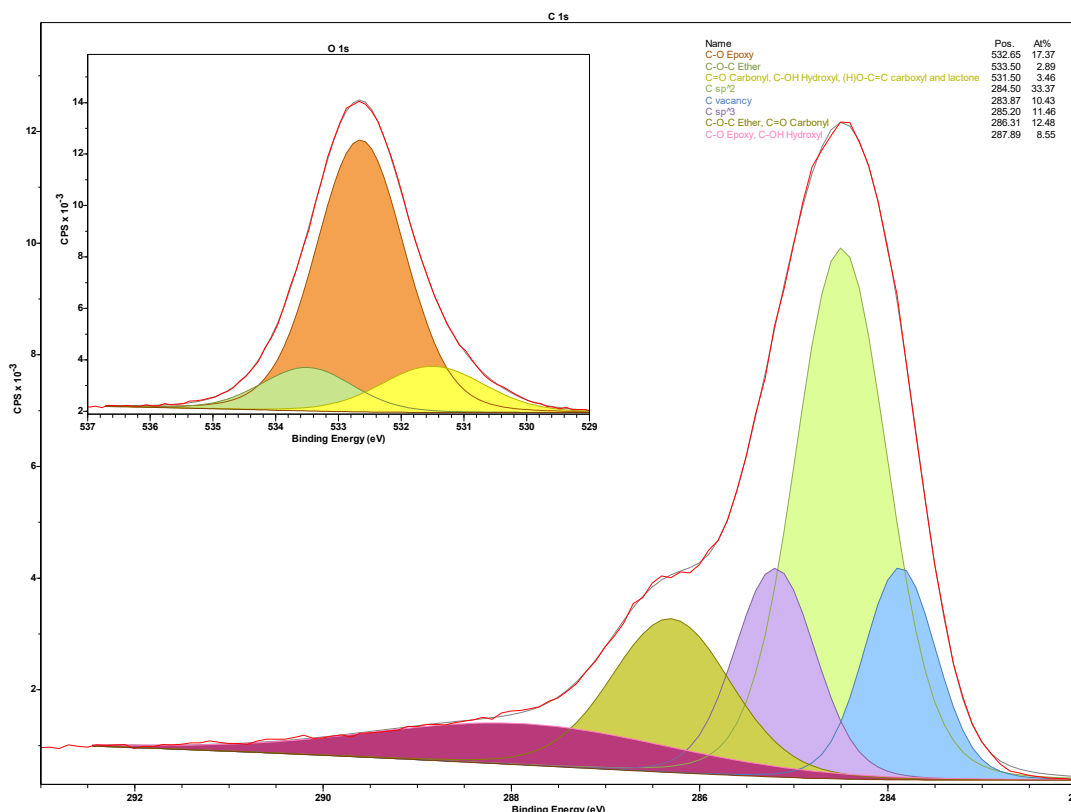


Figure 5.16: High resolution C1s and O1s spectra of polyethylene terephthalate derived carbon.

Figure 5.17 demonstrates a similar ratio between sp^2 and sp^3 carbon bonds to PEDC (~2:1 at% respectively). Figure 5.5 shows that the thermal decomposition pathways of polystyrene largely favour depolymerisation, and breakdown into monomers, dimers and trimers of styrene. This results in the presence of aromatics in the cracked vapours as precursors for carbonisation. When carbonisation of these products occurs, the lack of long aliphatic chains would prevent additional cyclisation without the scission of the already existing aromatic ring. As such, carbonisation would favour short aliphatic sections connecting aromatic regions, resulting in a higher degree of sp^3 carbon speciation. This is in contrast to PETDC, where thermal decomposition pathways are significantly more complex, offering a wider variety of cracked products for carbonisation, as well as the presence of a longer endogenous aliphatic

chain in which cyclisation may occur. Carbon vacancies for PSDC also increase somewhat when compared to PEDC and PPDC, suggesting further out of plane deformations. When contrasted with the Raman spectrum, this is likely due to out of plane deformations resulting from the presence of 5-member rings, rather than 7-member rings, given both the large A_2 peak, as well as the S_L peak. This is also supported by the thermal decomposition pathways, as there would be a decreased likelihood of forming long enough aliphatic chains to cyclise into 7-member rings.

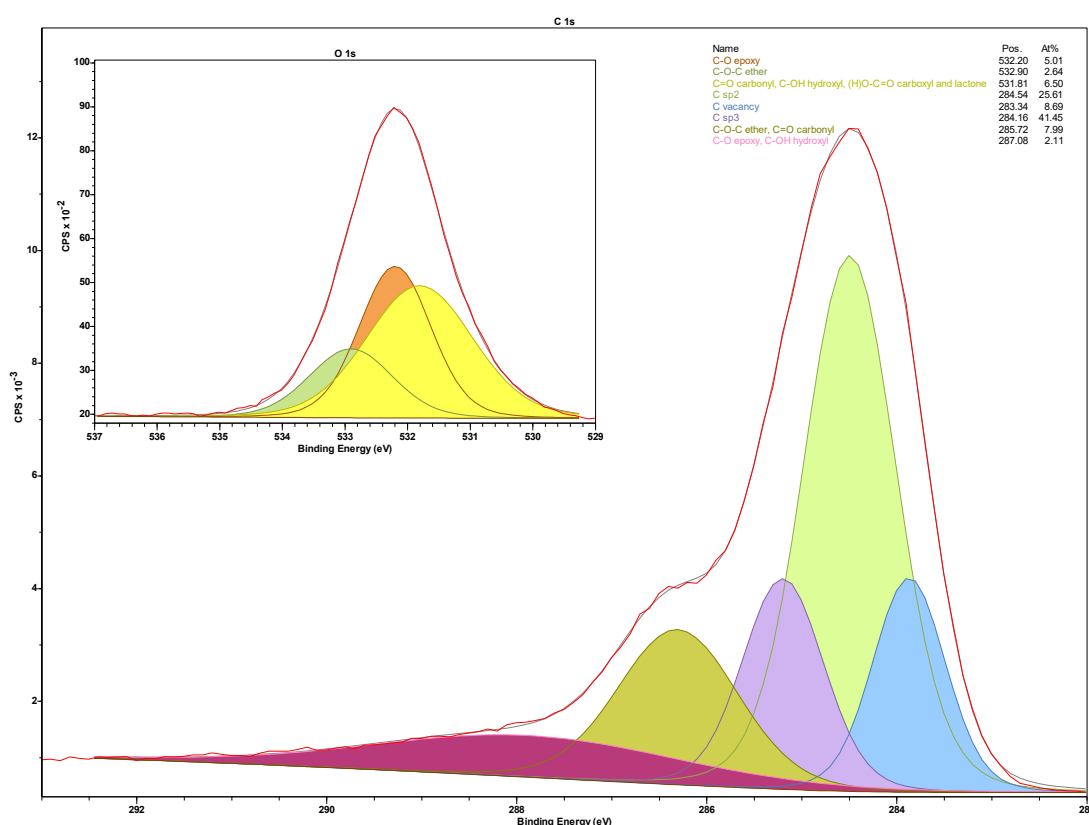


Figure 5.17: High resolution C1s and O1s spectra of polystyrene derived carbon.

Analysis of the O 1s spectra shows the most diverse breakdown of substituent components. Measurement shows an asymmetric peak with a small shoulder. Deconvolution shows that similar trends to previous samples still exist, with the primary formation of carbonyl bonds at 6.5 at%. However, the sample showed a substantial presence of both epoxy bonds (5.01 at%), as well as other bonds, primarily ether bonds, at 2.64%. Figure 5.18 shows the most significant differences to any of the XPS spectra.

Figure 5.18 follows the established trend of sp^2 carbon formation being the primary modality in the carbonisation process. A $sp^2:sp^3$ ratio of $\sim 3:1$ exists for this sample, in line with other plastic precursors. Similar degrees of carbon vacancies are also demonstrated in this sample in line with Raman results showing a prominent A_2 band. Speciation of oxygen bonds shown in the O1s spectrum show the most significant difference to other samples, with a strong preference for the formation of ether bonds over epoxy, carbonyl, hydroxyl, carboxyl, or lactone bonds. This suggests that oxygen bonding is primarily occurring in the aliphatic regions of the POGC, rather than aromatic regions, which would be the case if epoxy groups were more prevalent.

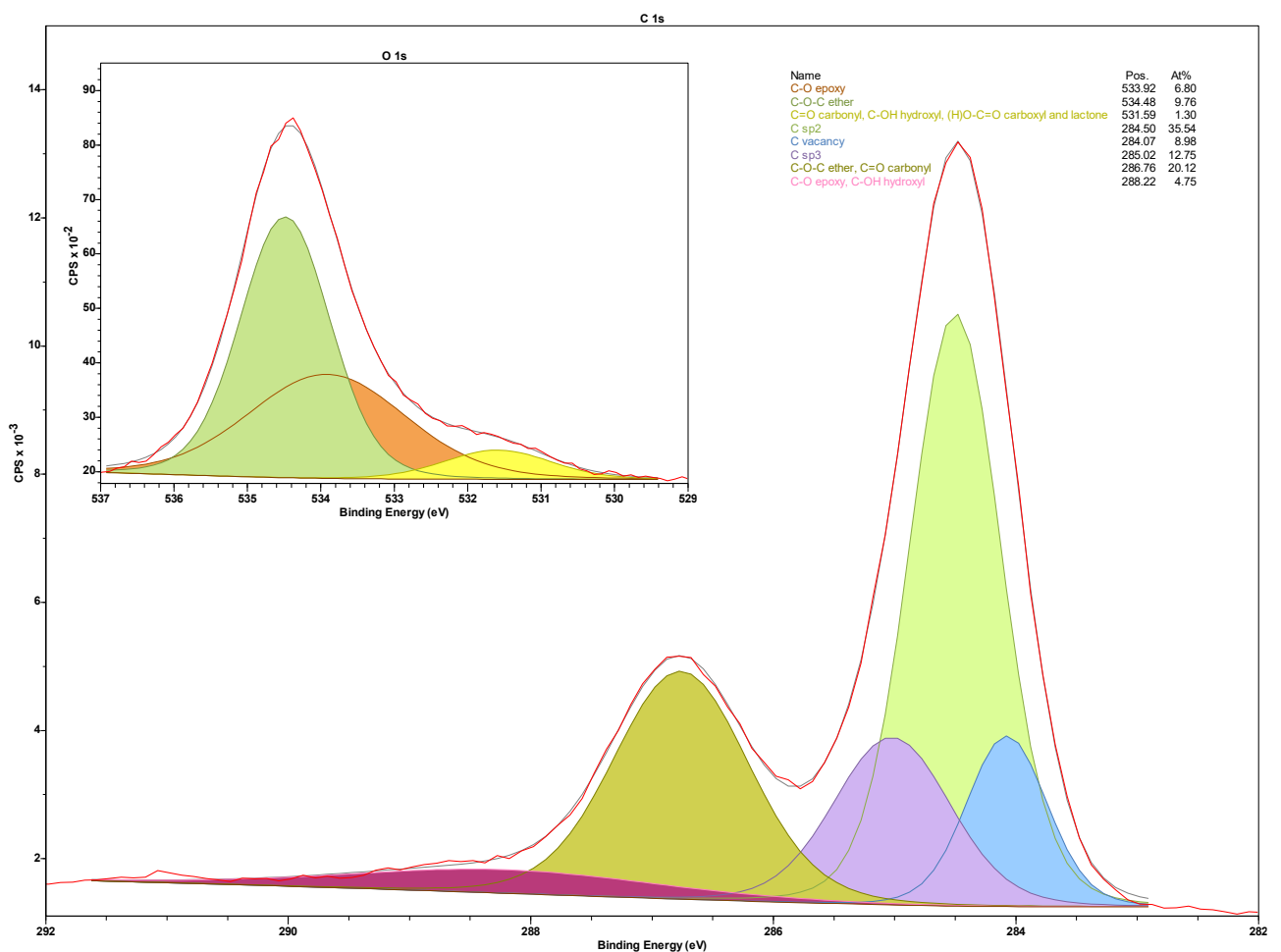


Figure 5.18: High resolution C1s and O1s spectra of polyacrylonitrile derived carbon.

5.5: Summary of findings

- Waste plastics were successfully carbonised with the use of a galvanic reaction environment.
- Characterisation of the products using Raman spectroscopy suggests that the produced carbons most resemble partially oxidised graphitic carbon, with aromatic regions connected by aliphatic chains.
- The structure of the precursor plastic materials and their thermal decomposition pathways were shown to have effects on the types of carbon produced based on the ability to form intermediaries that are capable of cyclisation.
- Formation of sp^2 bonded carbons were shown to be preferred over sp^3 bonded carbons.
- Formation of carbonyl bonds were the preferential modality of oxygen incorporation into the carbon structure.
- XPS results indicated that endogenous oxygen of the precursor material was able to be incorporated into the structure of carbon products.

Chapter 6: Modification of plastic precursor materials

6.1: Introduction

When considering the application of LM carbonisation of waste plastics for recycling purposes, it is important to consider the energy requirements of the process. The reasons for this are twofold: firstly, decreasing the energy requirements lowers the cost of the process, allowing the product to be marketed at a more competitive rate when compared to traditional sources, and, secondly, it lowers pollution caused by the process when powered by non-renewable energy.

As outlined in chapters 2-4, the methodology used requires reaction between a gaseous plastic fraction, and the heated liquid galinstan. These can be achieved simultaneously by the addition of cracking catalysts to the waste plastic before its gasification. Cracking is the process of breaking carbon-carbon bonds in long chain hydrocarbons to form lighter hydrocarbons. The parameters of cracking are largely dictated by temperature, and the presence of a catalyst¹⁶⁹. Cracking occurs by the process of homolytic fission, where intramolecular bonds disassociate and each of the resulting fragments retain one of the electrons from the original electron pair and results in the formation of radicals¹⁷⁰. The introduction of catalysts to this process promote the formation of carbocations, which force rearrangements in the molecule and result in the scission of carbon-carbon bonds by accepting the radical formed by the homolytic fission process¹⁷⁰. A schematic of this can be seen in Figure 6.1. Commonly applied catalysts are alumina based, such as zeolites¹⁷¹.

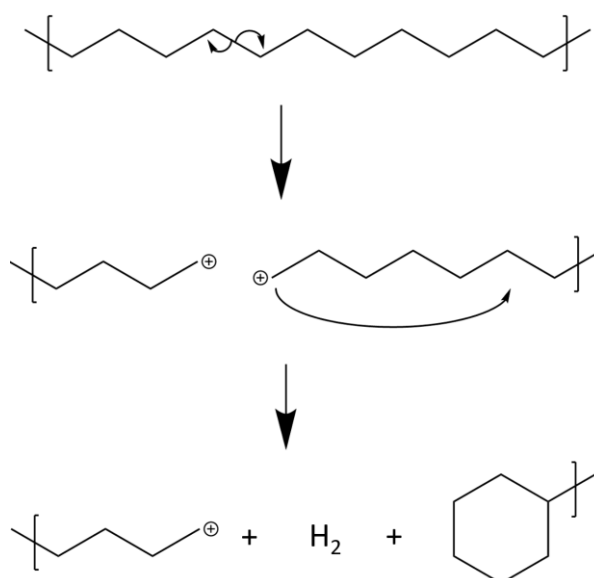


Figure 6.1: An example of homolytic fission followed by carbocation rearrangement forming cyclic rings.

LMs have been demonstrated to have higher catalytic activity with lighter hydrocarbons^{104, 117}. As a result, the modification of the waste plastic precursors with cracking catalysts is likely to be advantageous in their carbonisation, and dehydrogenisation. In this chapter, catalysts were investigated for their effect on carbon yield of the reactor. The rationale behind this approach is that lighter polymer fractions have a lower boiling point, and as such, lower the amount of polymer condensation on the exhaust of the horizontal furnace seen in Figure 6.2.

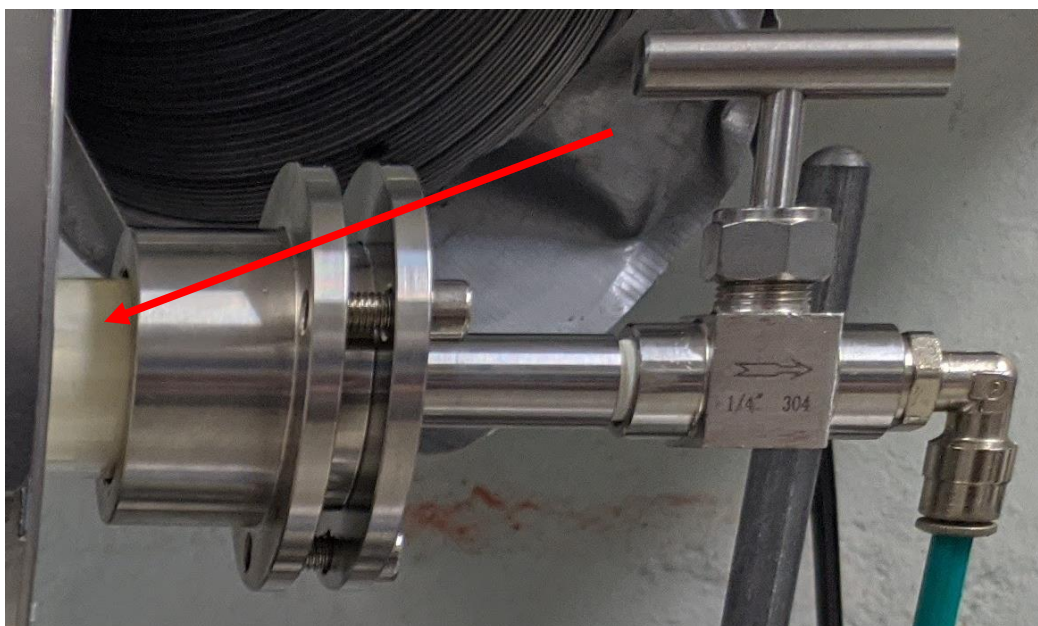


Figure 6.2: A photo of polymer condensation in the furnace exhaust (part number 2 in Figure 4.1)

6.2: Modification of plastic precursors

An area of key concern outlined in Chapter 4 is the yield of the process. Limitations in reactor design were the significant cause of these low yields as keeping the plastic fragments gaseous between the two furnace components proved difficult. In this chapter, the effects of a cracking catalyst (alumina, silica, or zeolite) added to plastic waste were assessed based on the characteristics of the carbon product, as well as the yields achieved. The methodology to produce waste plastic/metal oxide composites is outlined in Chapter 3.

Upon the modification, various colour changes were noted when compared to the unmodified material, which was either white or transparent and colourless. This is shown in Figure 6.3.



Figure 6.3: Colours of various metal oxide/waste plastic composites.

Additionally, changes in the feel of the materials were also observed ranging from increased brittleness to a reduction in malleability and an increase in strength. These observations suggest that the chemical structure of the plastics has been altered and is discussed further in the next Chapter with support from FTIR characterisation.

6.2.1: Fourier transform infrared spectroscopy of the modified plastic precursors

FTIR of the plastic composites was run and compared with that of the unmodified plastics. Polyethylene showed the least structural change in the modification process. This is seen in Figure 6.4. Major features of polyethylene such as C-H alkane stretching between 3000 and 2840 cm^{-1} , and C-H alkane bending around 1450 cm^{-1} persist between the unmodified and modified samples¹⁷².

This is consistent with observations of the modified and unmodified materials. After melting and resolidifying, both unmodified and modified polyethylene becomes brittle and has a waxy feel to it. This is likely the result of a lower molecular weight after the melting process when compared to the original as well as a small degree of carbonisation. The unmodified PE sample was white, like the PE/Si composite. However, colour changes were observed in the PE/Al, and PE/Ze composites. Alumina powder was also white, while the zeolite was a dull yellow. As such, the colour change is not related to the colour of the metal oxide additives, but rather some interaction with the polymer itself during the melting process. However, the exact nature of this colour change is undetermined. It is possible that a structural change has occurred, but the nature of the structural feature scatters light inelastically. Thus, no observable difference would be seen in FTIR.

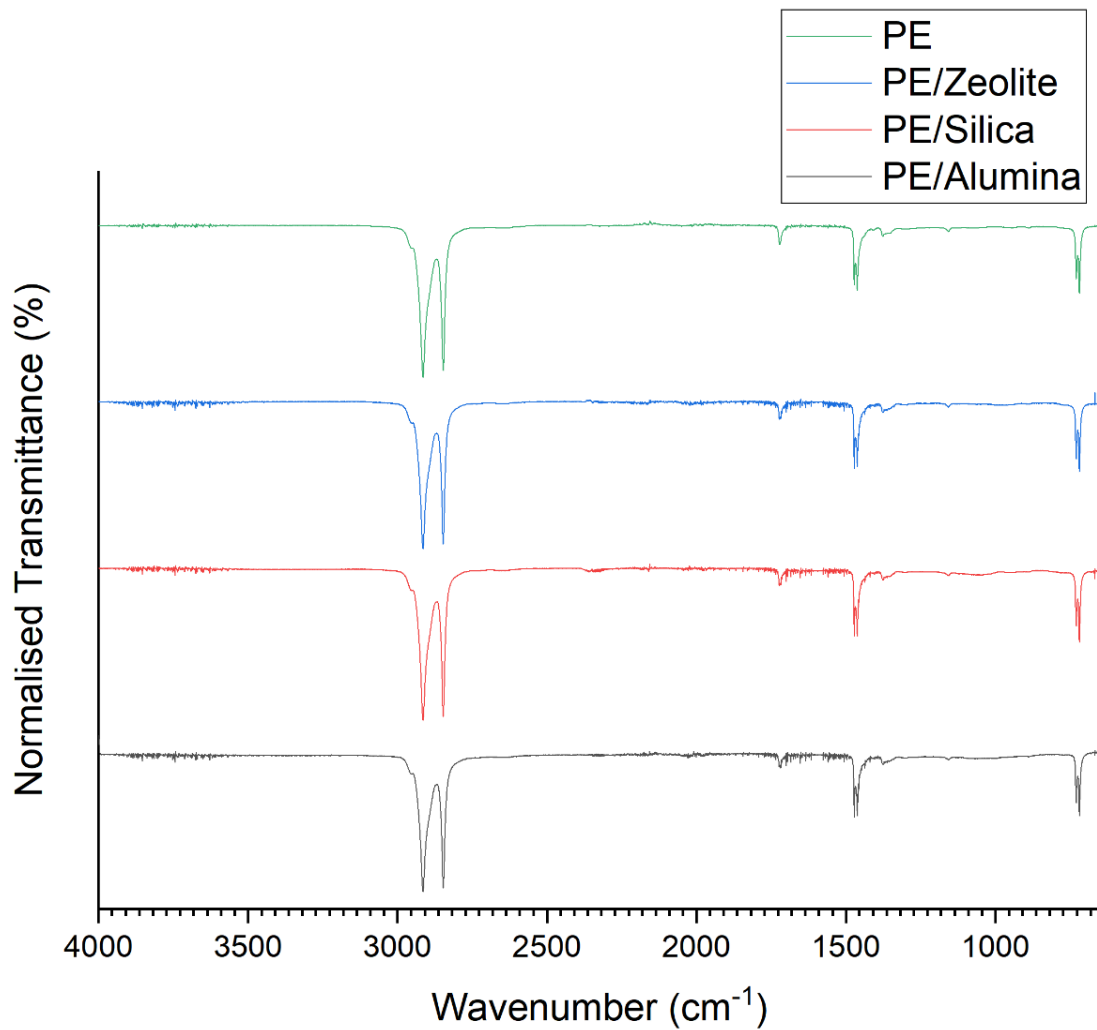


Figure 6.4: FTIR of polyethylene waste plastic, and its zeolite composite, silica composite, and alumina composite (top to bottom).

Polyethylene Terephthalate samples show some degree of structural change in their FTIR spectra in Figure 6.5. Weak features between 3000 and 2800 cm^{-1} become more pronounced in the metal oxide composites compared to the unmodified sample. The feature between 3000 and 2800 cm^{-1} is likely C-H stretching. It is theorised that this is the result of the reduction of the polymer to a more saturated state because of heating in the presence of a metal oxide.

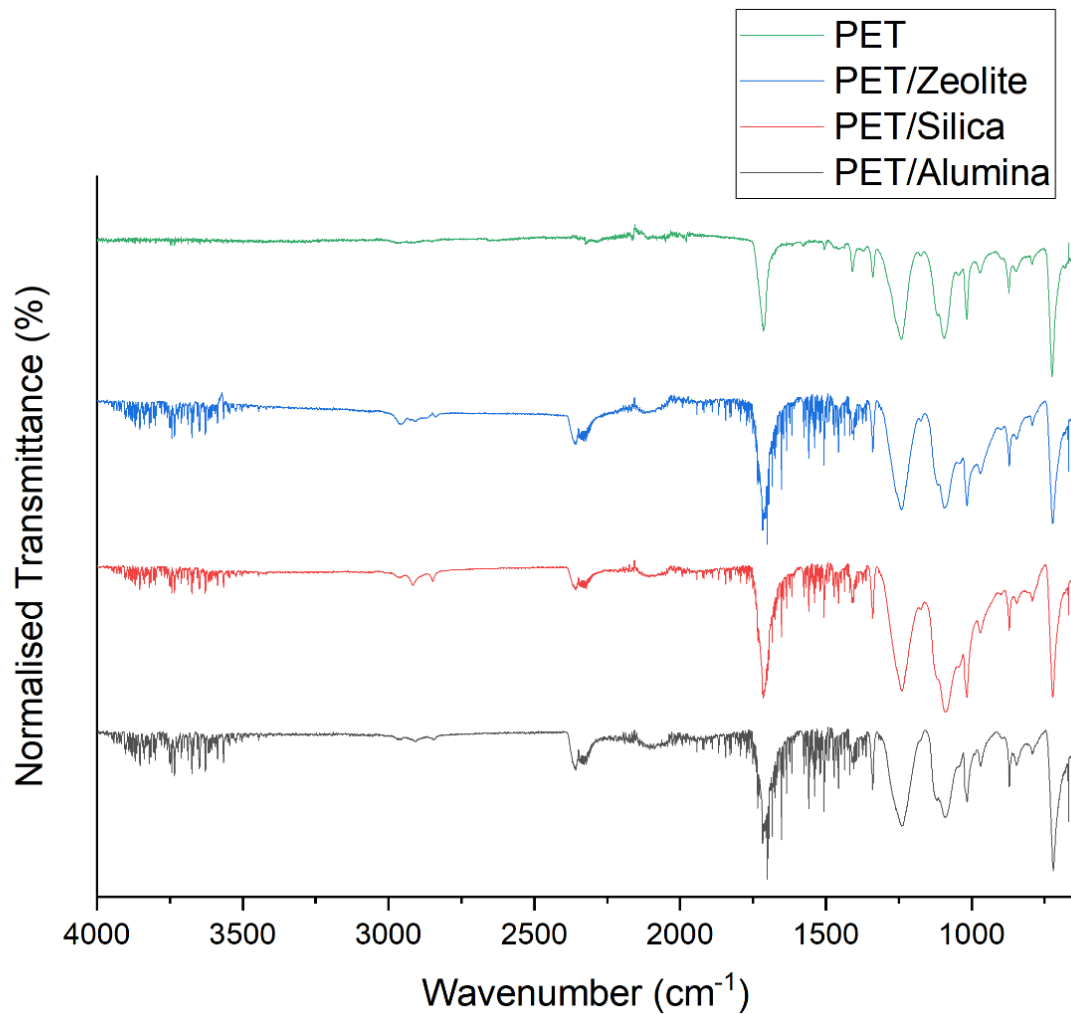


Figure 6.5: FTIR of polyethylene terephthalate waste plastic, and its zeolite composite, silica composite, and alumina composite (top to bottom).

Unlike PE, PET was observed to have significantly different feel between modified and unmodified samples. Unmodified samples retained much of their malleability and remained colourless and mostly transparent. The addition of metal oxides made all samples brittle, as well as opaque and coloured. The colour of samples did not align with the colour of the metal oxide additive, and so, a structural change must be occurring.

The polypropylene spectra (Figure 6.6) remain largely the same before and after modification. This aligns with minimal observed change in their feel. PP remained strong, rather than becoming brittle as other materials did. However, once again a significant colour change was observed, seen in Figure 6.3.

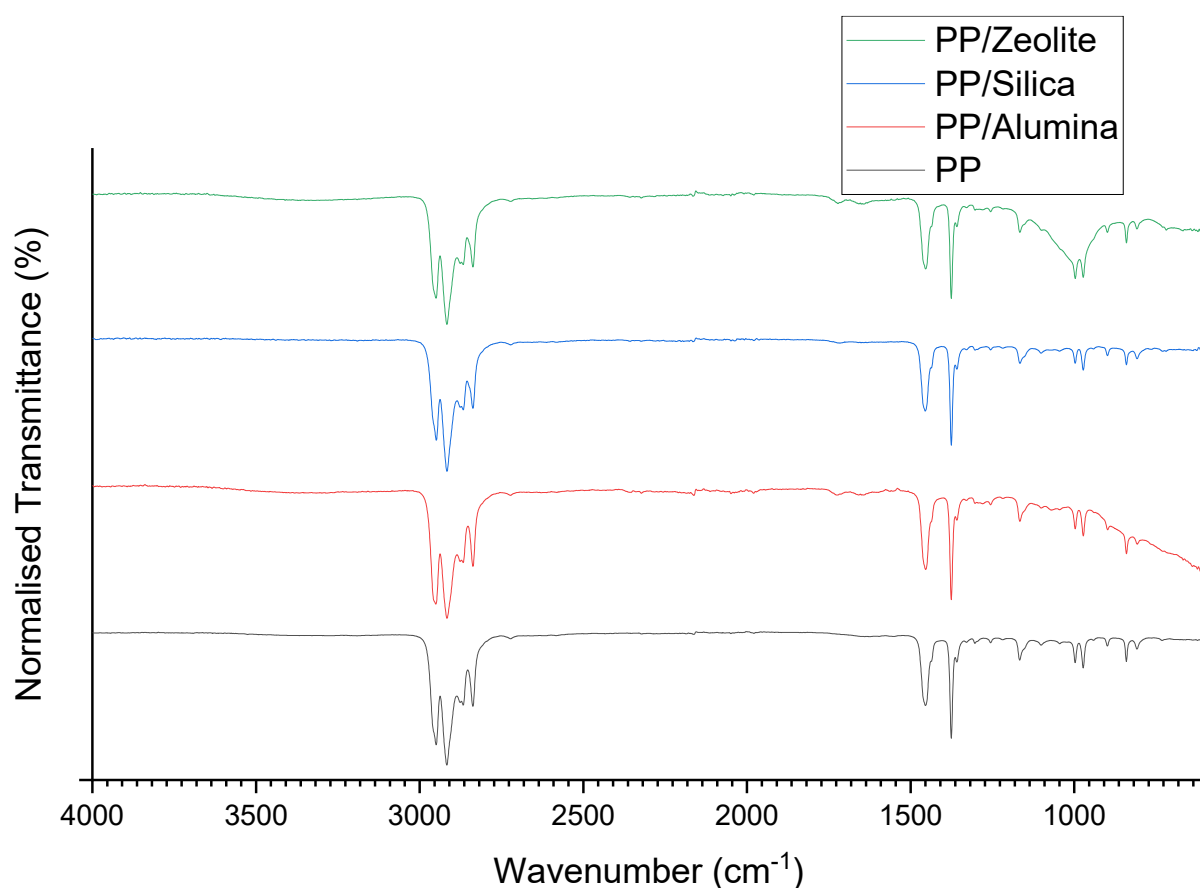


Figure 6.6: FTIR of polypropylene zeolite composite, silica composite, alumina composite, and waste plastic (top to bottom).

6.3: Properties of metal oxides

Metal oxides are commonly used as catalysts in various applications. Their catalytic effects can be attributed to various chemical and physical aspects including but not limited to their specific heat capacity, surface area, pore volume, pore size, and acidity. For this work, silica, alumina, and zeolite 5A were chosen to represent various combinations of these properties.

XRD was used to characterise the structure of each of the metal oxides, which varied in their degree of crystallinity. Silica represented a largely amorphous metal oxide, as seen in Figure 6.8. Its surface area was the highest of the tested samples at $364.08 \text{ m}^2\text{g}^{-1}$, and its pore volume and pore size were intermediate at $0.09611 \text{ cm}^3\text{g}^{-1}$ and 25.917 \AA respectively, as seen in Table 6.1. Alumina shows some degree of crystallinity, while still presenting an underlying amorphous curve in the XRD (Figure 6.8) and has the lowest surface area ($315.89 \text{ m}^2\text{g}^{-1}$), pore volume ($0.07778 \text{ cm}^3\text{g}^{-1}$), and pore size (18.046 \AA) as measured by BET (Table 6.1). Finally, zeolite 5A shows a highly ordered structure in XRD (Figure 6.8) with defined peaks, and lacks

the underlying amorphous curve shown by alumina. Its surface area was comparable to, though slightly lower than the silica sample at $357.18 \text{ m}^2\text{g}^{-1}$ and its pore volume and pore size were significantly larger than the other metal oxides are $0.16271 \text{ cm}^3\text{g}^{-1}$ and 52.591 \AA respectively.

Table 6.1: Summary of BET results of metal oxides.

	Surface Area (m^2g^{-1})	Pore Volume (cm^3g^{-1})	Pore Size (\AA)
Silica	364.1	0.09611	25.92
Alumina	315.9	0.07778	18.05
Zeolite	357.2	0.16271	52.49

Hysteresis loops of the BET isotherms, seen in Figure 6.7, show that the degree of microporosity also varies between samples, with alumina being the most mesoporous, and zeolite being the most microporous. Silica falls in between.

Literature values at 300°K show that the specific heat capacity of silica and alumina is 0.7451 and $0.7943 \text{ Jg}^{-1}\text{K}^{-1}$ respectively¹⁷³. A value for the specific heat capacity of zeolite 5A was unable to be found in literature, however zeolite 4A has a specific heat capacity of $0.9210 \text{ Jg}^{-1}\text{K}^{-1}$ and can be considered roughly equivalent to demonstrate the trend¹⁷⁴. In the amounts used in the plastic-metal oxide composite samples silica and alumina have roughly equivalent specific heat capacities. Thus, any differences in their performance are likely attributable to other aspects of their morphology. On the other hand, zeolites in general offer a comparably higher specific heat capacity. As such, decomposition performance of zeolites is likely higher in comparison with silica and alumina.

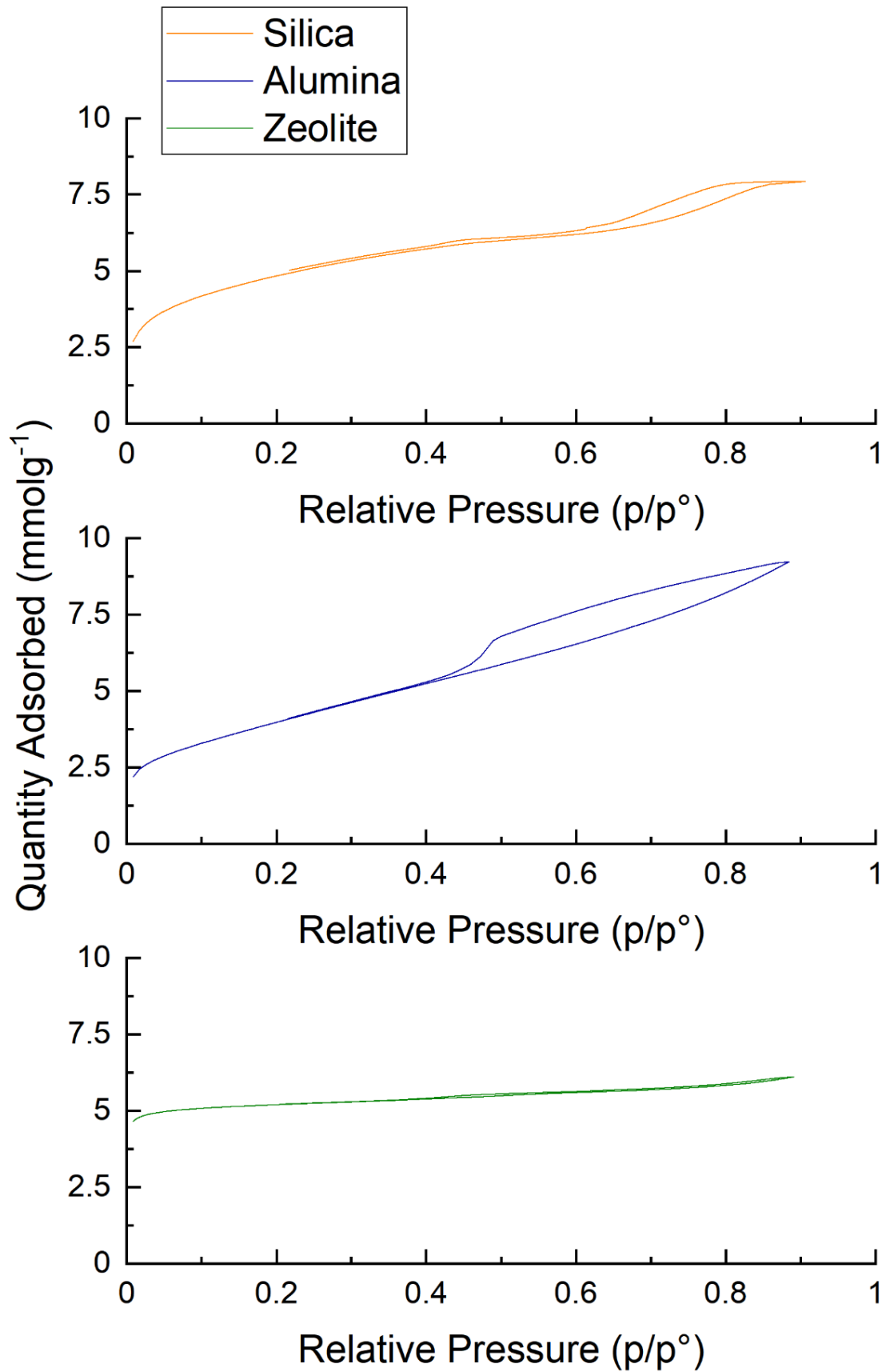


Figure 6.7: BET isotherm plots of metal oxide additives.

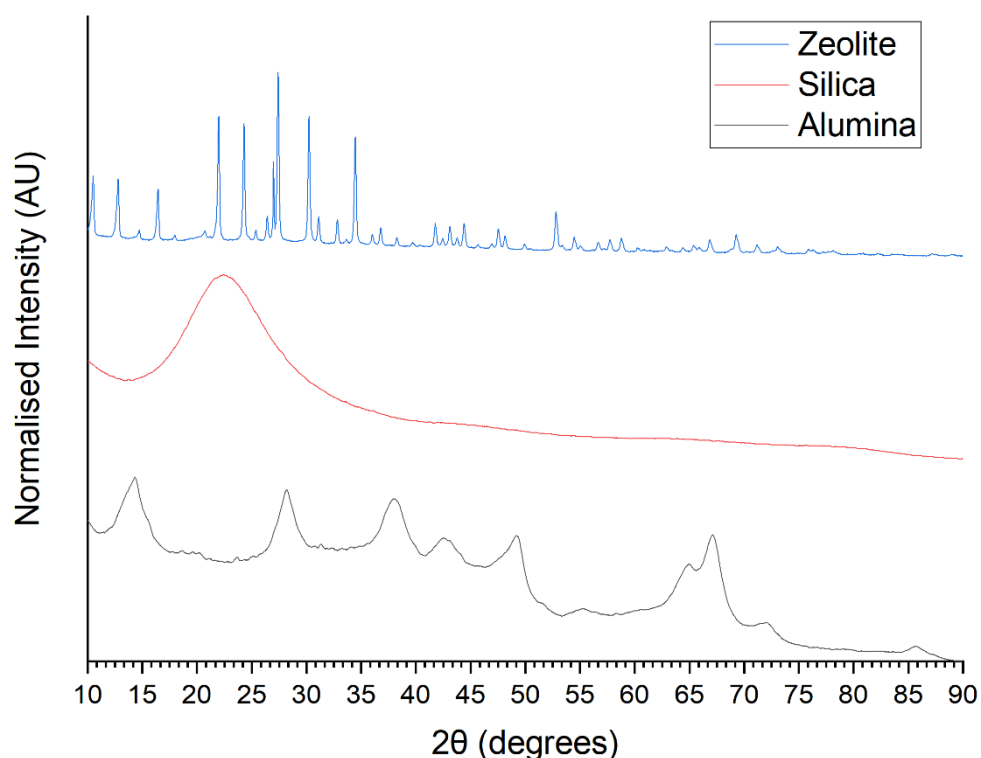


Figure 6.8: XRD of metal oxide additives.

Acidity of metal oxides relates to their ability to act as an electron pair acceptor in the case of Lewis acids¹⁷⁵. The degree of their acidity is largely a function of the electronegativity of the oxides accompanying metal ion with more electronegative metals tending to produce acidic oxides¹⁷⁶. As a sample in this work, Alumina falls into an amphoteric classification as it may act as either an electron donor or acceptor. Silica is an acidic oxide and functions as an electron acceptor. Finally, zeolite 5A ($\text{Ca}_n\text{Na}_{12-2n}[(\text{AlO}_2)_{12}(\text{SiO}_2)_{12}]x\text{H}_2\text{O}$) is composed of four metal oxides; sodium, calcium, aluminium, and silicon oxide structured in octagonal three dimensional octagonal rings forming cages¹⁷⁷. This forms a silica-aluminide bulk with electron acceptor properties, with electron donator nodes formed in the calcium and sodium point groups.

Oxidation of petroleum derived chemicals is a common use for Lewis acid catalysts, and metal oxides are commonly used in this role as they are far more tolerant to decomposition in water than other metal based Lewis acids, such as metal chlorides¹⁷⁸. As discussed in Chapter 5, it is theorised that partial oxidation of the precursor material due to the presence of oxygen which could not be purged from the reactor is beneficial to the cracking of the plastic precursors. Thus, the Lewis acidity of the chosen metal oxide catalysts is theorised to form beneficial

intermediaries before contact with the liquid metal and benefit the overall carbonisation process¹⁷⁸.

6.4: TGA of plastic composites

Thermogravimetric analysis was conducted to compare the degradation properties of modified plastic precursors to that of the unmodified plastics. As seen in Figure 6.9, unmodified polyethylene waste would begin to decompose at approximately the same temperature as the metal oxide modified equivalents.

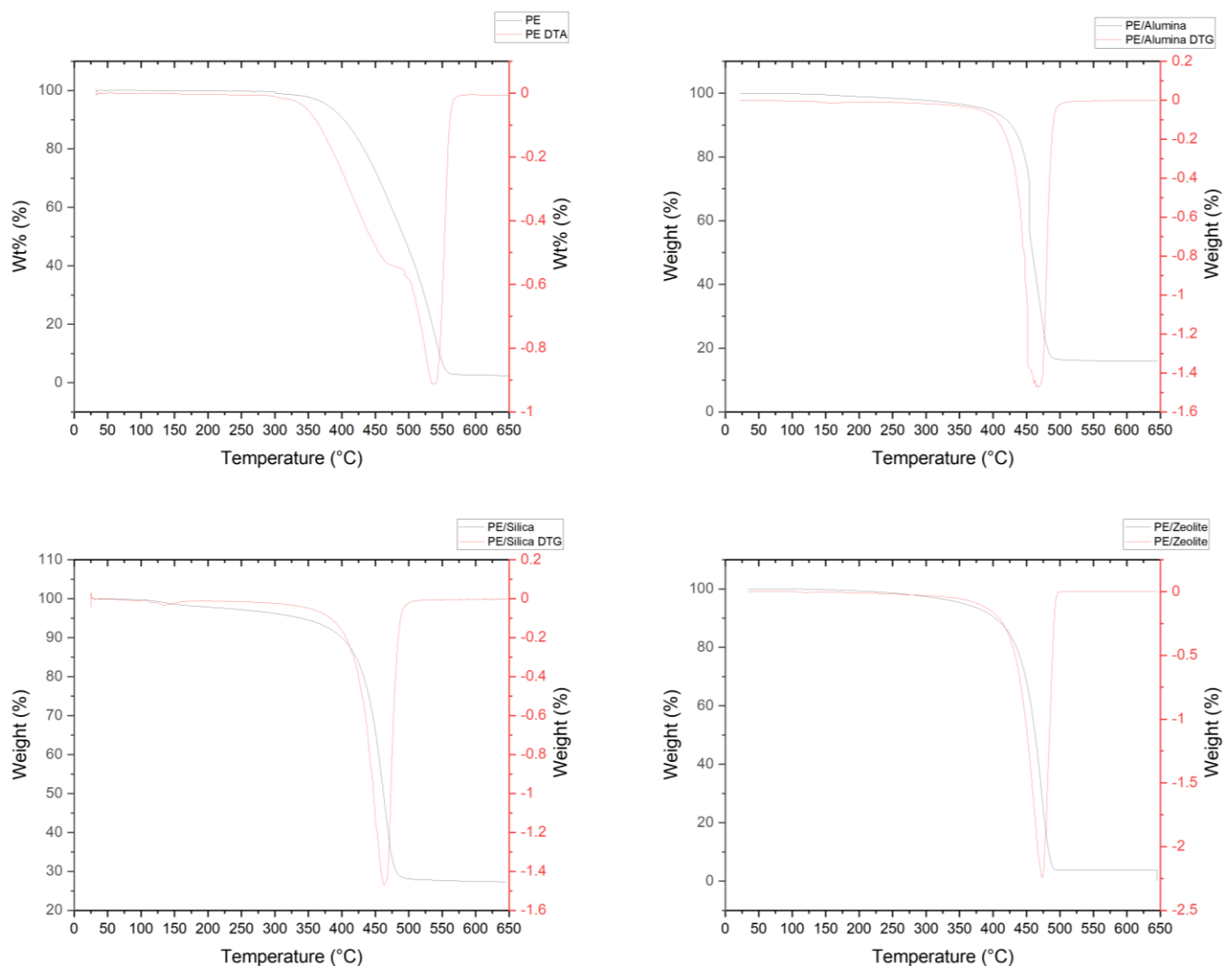


Figure 6.9: Nitrogen TGA of polyethylene and its metal oxide composites.

However, modified equivalents experienced a much sharper decline in mass compared to unmodified PE. This is likely the result of the metal oxide additives acting as both thermal mass to increase thermal transfer to the PE and thus increase the thermal flux of the

composite¹⁷⁹. However, metal oxides may act as cracking agents to promote thermal cracking into lower molecular weight fragments. As such, decomposition rates would increase.

The shape of the curve of unmodified polypropylene decomposition, seen in Figure 6.10, is roughly equivalent to that of its metal oxide modified counterparts. However, decomposition temperature begins approximately 50°C sooner. This is likely the result of cracking occurring between the metal oxide and the PP. While increased thermal flux would primarily effect the slope of the thermogram, shifts in the first derivative are related to changes in decomposition pathways¹⁷⁹. This suggests that the addition of metal oxides is producing the desired effect by lowering the energy requirements of the reaction, while producing lower molecular weight fractions for the galinstan to react with.

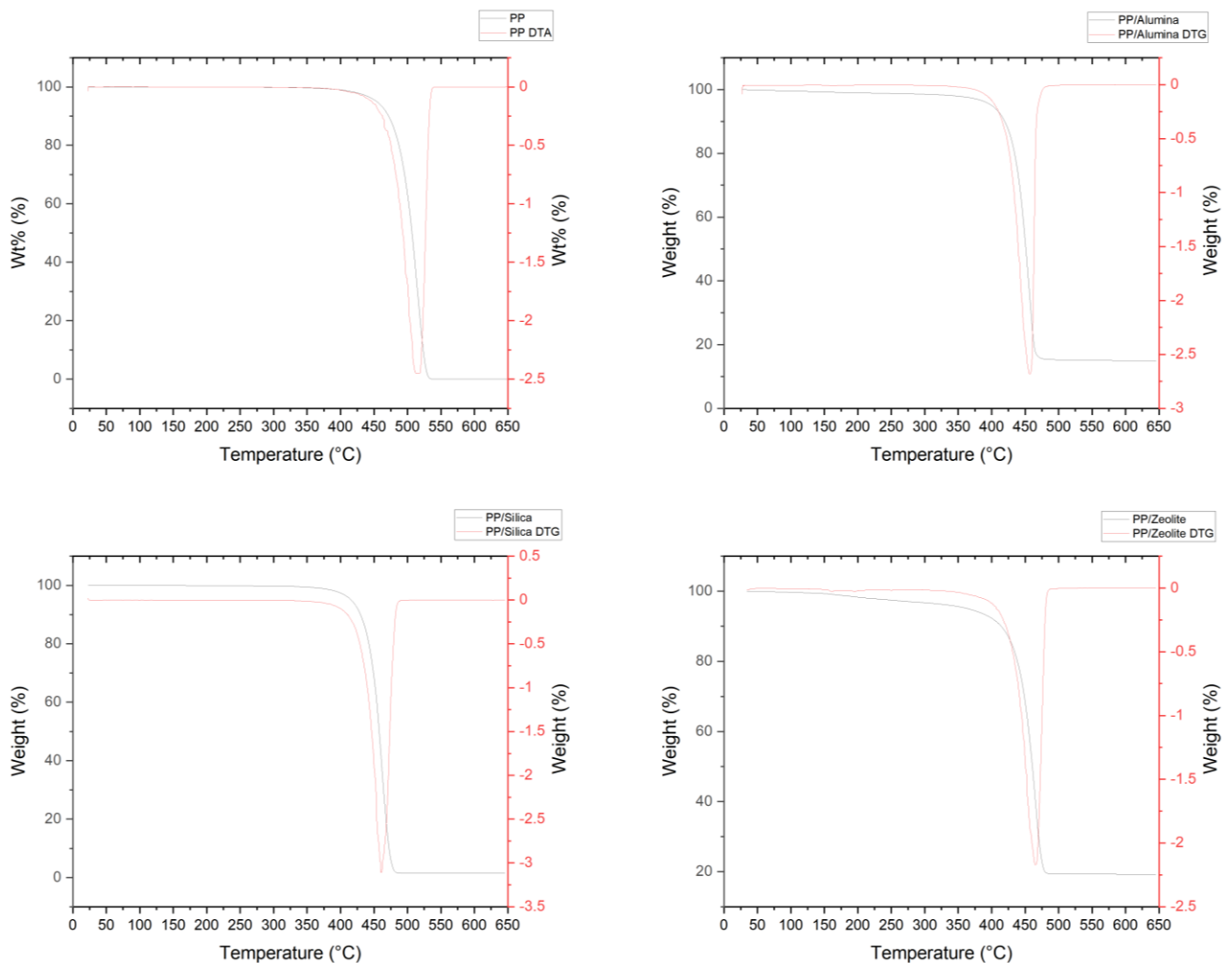


Figure 6.10: Nitrogen TGA of polypropylene and its metal oxide composites.

Finally, polyethylene terephthalate, seen in Figure 6.11, shows similar trends to that of polypropylene. The shape of the curve of the thermogram remains somewhat consistent, while the beginning of decomposition is shifted approximately 50°C lower. This again is likely attributable to thermal cracking for the same reasons outlined above. Another trend seen in the PET samples is the difference in ash content of the thermogram. PET produces a relatively large degree of ash from the reaction (~45%), however this is reduced with the addition of the metal oxides significantly. As per Chapter 3.5, the polymer-metal oxide composites are mixed in a 3:1 ratio by mass, meaning that a perfectly representative sample would leave 25% mass in metal oxide behind. Perfect distribution of metal oxide was not possible given the composition methods used, so the mass of metal oxide in a given composite sample may vary. However, with the assumption that some of the remaining mass in the composite samples is metal oxide, that leaves very little ash content after decomposition. This suggests that the decomposition pathways vary significantly to where little ash content remains.

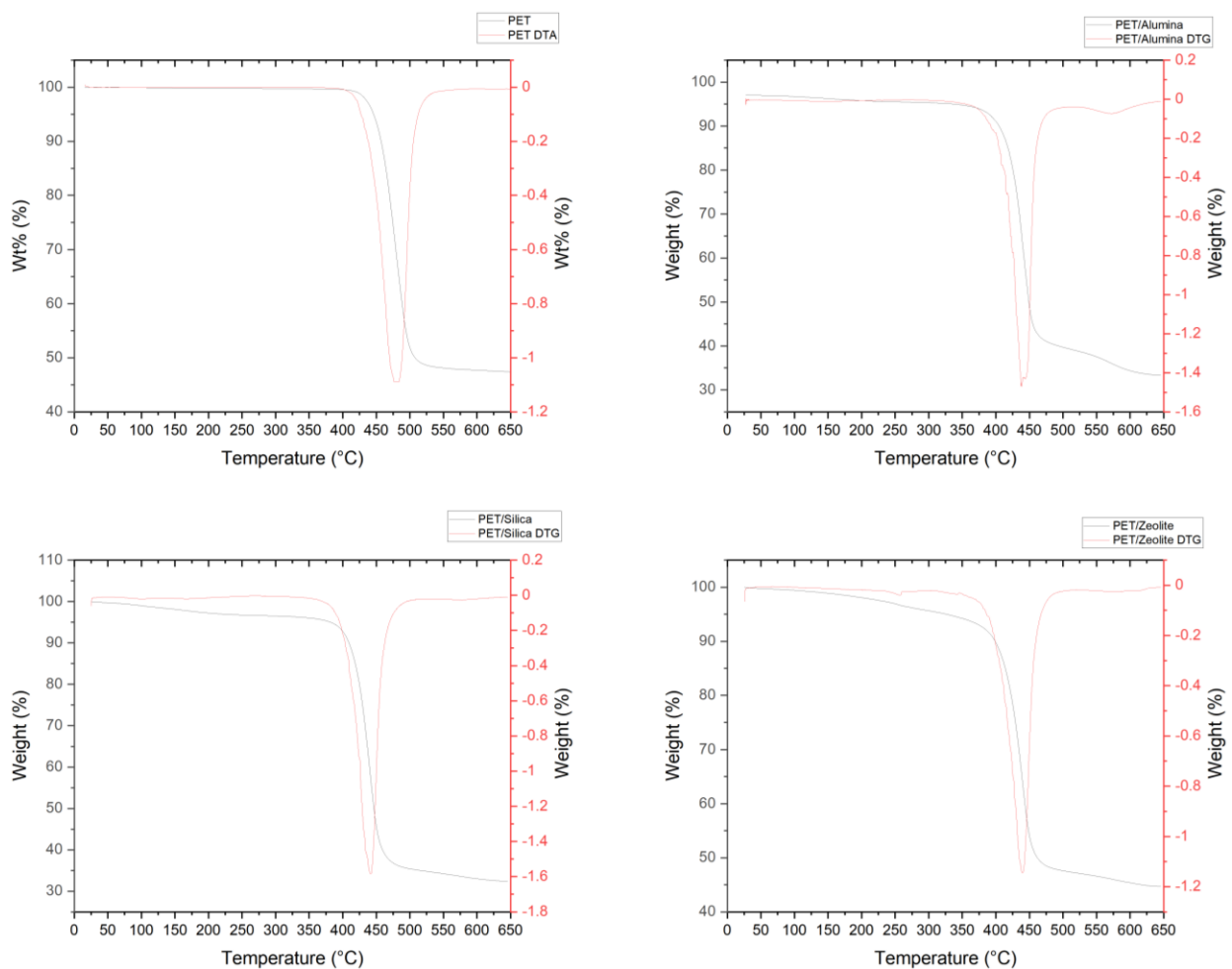


Figure 6.11: Nitrogen TGA of polyethylene terephthalate and its metal oxide composites.

Yields notably increased from the addition of metal oxides to the precursor plastic wastes. However, due to the low density of the produced material wt.% numbers were difficult to distinguish between modified and unmodified precursor samples, with recovered material generally being on the order of milligrams. Based on observed volumes produced however, yields were substantially improved with only three repeats of each sample required to obtain enough product for analysis. The TGA results above support this observation with the mechanism of action being that the addition of metal oxides induces lower temperature cracking into lower molecular weight fractions which are more easily reacted with the galinstan.

6.5: Properties of carbon derived from modified precursors

6.5.1: X-Ray diffraction

XRD was used to characterise the crystal structure of the produced carbon. To an extent, all samples show a similar overall feature with a large amorphous peak generally centred around 22° (2θ) and a smaller amorphous peak generally centring around $44^\circ 2\theta$. Generally, this trend is representative of several carbon varieties, however the broadness of the peaks hints at a largely amorphous crystal structure. This most likely hints at the char being some form of partially oxidised graphitic carbon (POGC) as the degree to which microstructures such as short range polyaromatic hydrocarbons, and graphite-like quasi-crystalline domains can affect the sharpness of the characteristic peaks¹⁸⁰. Less defined, broader peaks hint at low crystallinity in the microstructure of the carbonaceous material¹⁸¹. As such, it is suggested that the produced materials are a type of POGC. However, some samples show more defined peaks which stand out from the amorphous background. This is likely related to the presence of defined regions of crystallinity in an otherwise amorphous bulk.

Modified polyethylene carbon samples produced a similar trend to one another with a large amorphous curve peaking around $22^\circ 2\theta$ and a smaller peak at $44^\circ 2\theta$. This can be seen in Figure 6.12. Notably, the peak centre of the first amorphous peak is shifted slightly left in the polyethylene-silica derived carbon (PE-SiDC) when compared to the polyethylene-alumina derived carbon (PE-AlDC), and polyethylene-zeolite derived carbon (PE-ZeDC). PE-SiDC falls at

$22^{\circ}2\theta$, while both PP-SiDC and PET-SiDC are at $25^{\circ}2\theta$. This trend does not seem to carry on to the second amorphous peak.

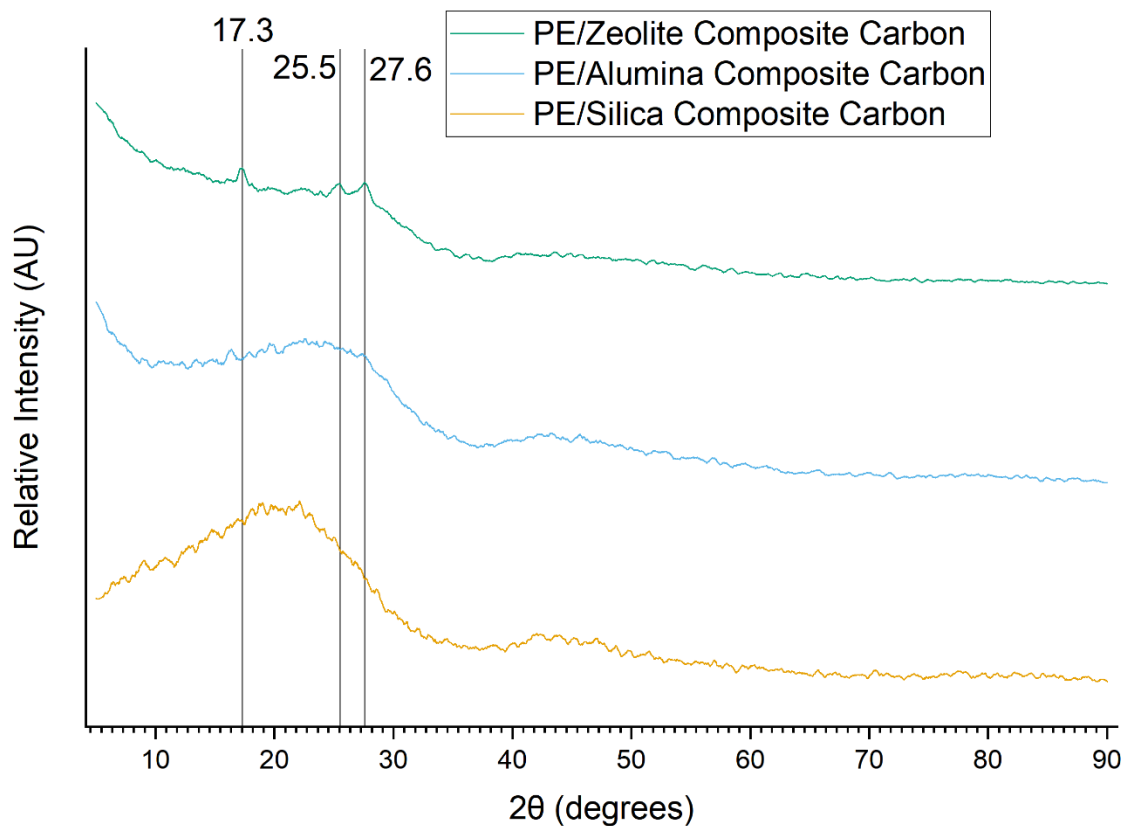


Figure 6.12: XRD of carbonaceous products derived from modified polyethylene precursors. A further difference is shown in the presence of small but prominent regions of crystallinity in the PE-ZeDC sample, which stand out above background noise at 17.3 , 25.5 , and $27.6^{\circ}2\theta$. These peaks were not able to be resolved in the PE-SiDC and PE-AIDC samples, however they are more prominent in other silica and alumina modified polymer derived carbon samples. This suggests that, rather than being a feature specific to zeolite modified samples, they arise due to the oxidation potential of metal oxides in general but are more prominent in zeolite samples. This is likely due to the production of favourable cracking products in the initial gasification of the plastic precursors. In Chapter 5, it was theorised that the gasification of the polymer precursors in a limiting oxygen environment was beneficial to the reaction as it facilitated the partial oxidation of the gaseous polymer fractions. This oxidation facilitated dipole charges in the cracked molecules which act as a reaction sight for the galinstan to reduce the short chain hydrocarbons.

Modified polypropylene samples best demonstrate the presence of these crystalline regions, as seen in Figure 6.13. They follow a similar trend to the modified polyethylene samples with an underlying amorphous peak centred around $25^{\circ}2\theta$ and a further amorphous peak centred around $44^{\circ}2\theta$. Notably however, the same peaks at 17.2 , 25.3 , and $27.6^{\circ}2\theta$ stand out far more prominently in all samples when compared to the background.

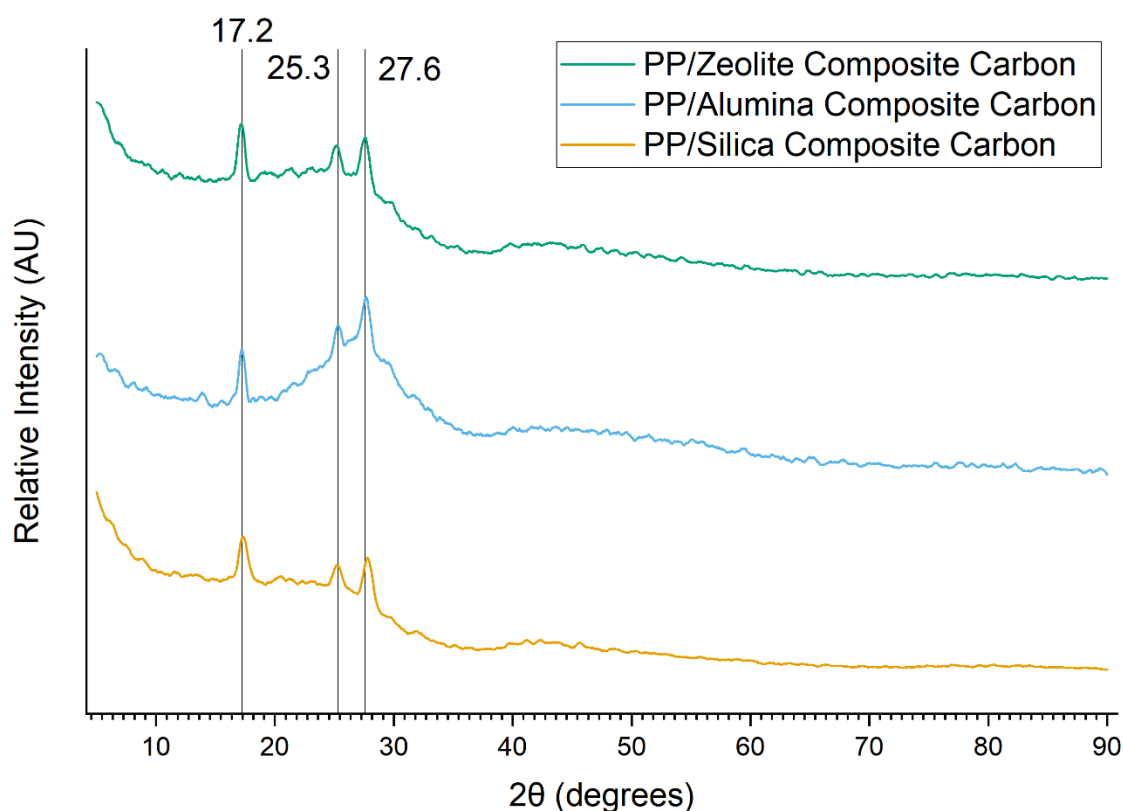


Figure 6.13: XRD of carbonaceous products derived from modified polypropylene precursors.

Based on the previously outlined theory of oxidation occurring at the cracking phase of the reaction, it would follow that the structure of the polypropylene is beneficial to this process. This is likely the result of the presence of branched methyl groups on the polymer chain, which can easily be oxidised to various products such as hydroxymethyl groups, aldehyde groups, and carboxylic acid groups¹⁸². However, given the relatively low oxidation potential of the metal oxides¹⁷⁸, hydroxymethyl and aldehydes are the most likely product¹⁸².

Modified polyethylene terephthalate samples shown in Figure 6.14 continue the general trend seen with a large amorphous peak centred around $25^{\circ}2\theta$ and a smaller amorphous peak centred around $44^{\circ}2\theta$. However, the presence of crystallinity is once again significantly

diminished in all but the zeolite modified sample. Following from the oxidation theory, this would be expected, as the PET structure is quite chemically resistant and exists in a high oxidation state. It doesn't contain sights which could be easily oxidised and so the presence of an oxidative catalyst would have little effect. However, it was still observed that yields were higher in modified PET samples. This is likely due to the metal oxides acting as a simple cracking catalyst producing lighter molecular weight fragments from the polymer chain. These lighter fragments would more easily remain gaseous as they pass through the system, simply allowing for more carbonaceous gas to interact with the galinstan.

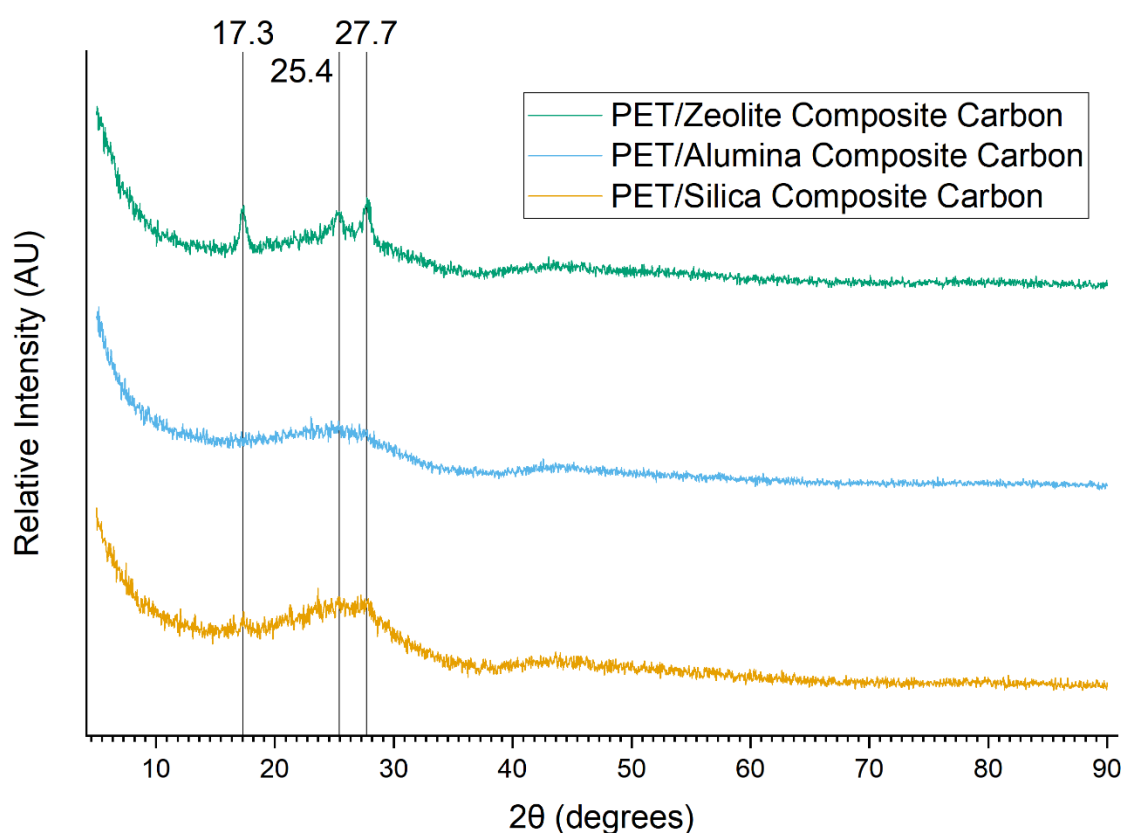


Figure 6.14: XRD of carbonaceous products derived from modified polyethylene terephthalate precursors.

6.5.2: Raman spectroscopy

Raman spectroscopy was employed to investigate the molecular structural features of the synthesised carbon. Similar trends can be seen in comparison to the Raman spectra for the unmodified polymer derived carbon samples presented in Chapter 5 with broad D band peaks around 1365 cm^{-1} , and G band peaks around 1590 cm^{-1} . As such, these follow the same explanation presented previously. However, it is notable that the G:D band intensity ratios of

all carbonaceous samples produced from metal oxide modified precursors is significantly higher and more consistent than those produced from unmodified precursors as seen in Figure 6.15.

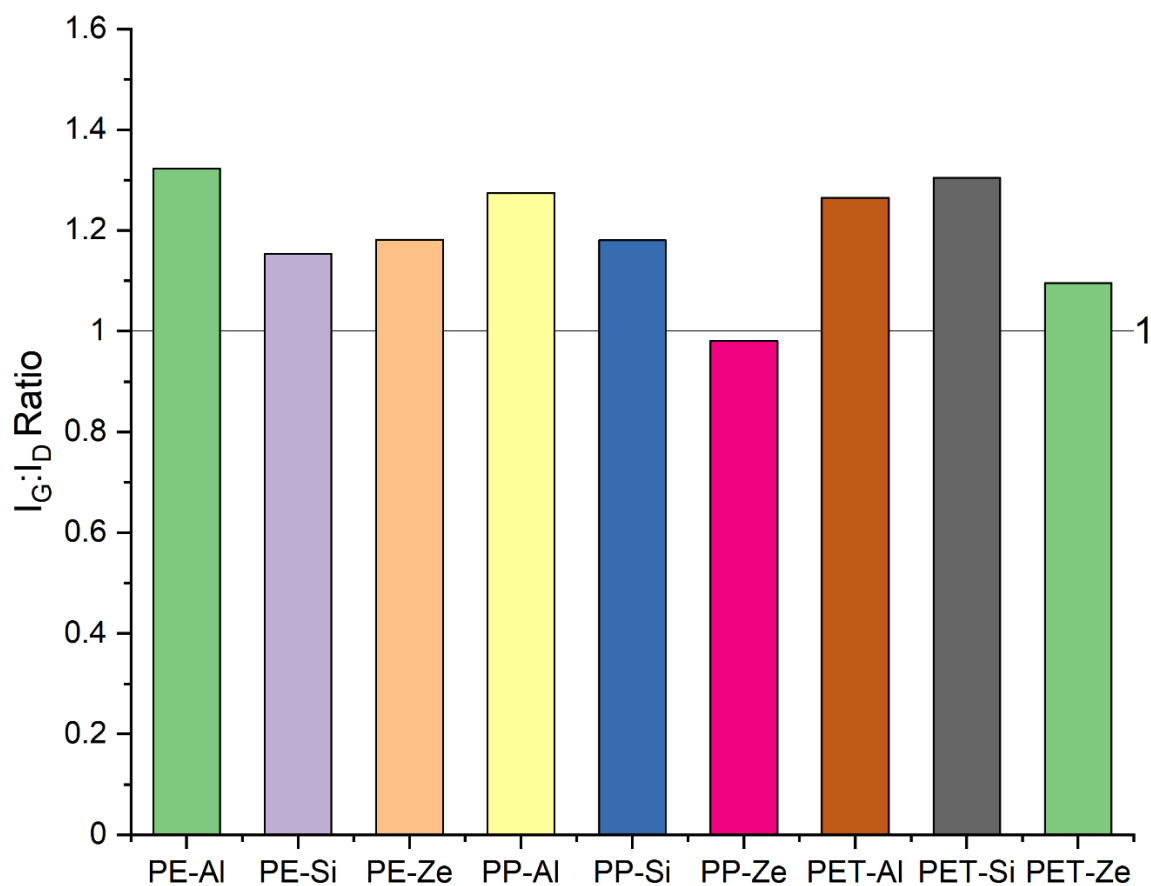


Figure 6.15: A chart of deconvoluted intensity ratios between G and D bands for various polymer precursors.

Once again, amorphous carbons and chars typically exhibit a particularly complex Raman spectra as a result of their nonuniform lattice, the complicated nature of precursor materials, and the method of their formation¹⁴¹. Computational simulations of various polyaromatic hydrocarbons have provided an insight into the lattice features which give rise to these shoulders¹⁴² which can be seen in the deconvolutions presented ahead. Smith et al identify ten distinct peaks within the Raman spectra of amorphous chars. A summary of their findings can be seen in Table 5.3.

Raman spectra collected from metal oxide modified precursors continue to exhibit many of these features outlined previously. Representative examples of deconvolution can be seen in the following figures. Deconvolution was performed using the Levenberg Marquardt

algorithm with a gaussian model and the resulting coefficients of determination (R^2) can be seen in Table 6.2. Deconvolutions were chosen based on the highest R^2 values obtained.

Table 6.2: A summary of R^2 values of Raman curve fitting from metal oxide modified carbon samples.

Polymer precursor and modification	Coefficient of determination (R^2)	Number of peaks identified
Polyethylene-Alumina (PE-Al)	0.99862	8
Polyethylene-Silica (PE-Si)	0.99908	8
Polyethylene-Zeolite (PE-Ze)	0.99781	7
Polypropylene-Alumina (PP-Al)	0.99950	8
Polypropylene-Silica (PP-Si)	0.99956	8
Polypropylene-Zeolite (PP-Ze)	0.99928	8
Polyethylene Terephthalate-Alumina (PET-Al)	0.99328	7
Polyethylene Terephthalate-Silica (PET-Silica)	0.99933	9
Polyethylene Terephthalate-Zeolite (PET-Ze)	0.99777	9

Shoulder band, low (S_L) is the product of weak breathing modes for small aromatic regions. These are ascribed to hydrogen motion along the carbon edge and are typically weak compared to other vibrations in the spectrum¹⁴². S_L is also associated with a secondary breathing mode for 7+ membered rings¹⁴³, as well as specifically with naphthalene. However, these vibrations are described as being stronger relative to the rest of the spectrum¹⁴². Weak S_L bands were found in all the carbonaceous samples derived from metal-oxide modified polymer precursors. Given their relatively low intensities, it is theorised that they arise from the presence small aromatic regions, rather than naphthalene or 7+ member rings as the latter would be expected to produce a more intense peak. This follows from assertions made in Chapter 5 regarding the nature of the carbonaceous material being produced. However, this band is more commonly resolvable in samples derived from metal oxide modified precursors, likely due to the higher yields being worked with. Furthermore, the S_L band is present at consistent intensities across all samples, suggesting that the inclusion of metal oxides somewhat acts to standardise the products.

Shoulder band (S) is described as the product of primary breathing modes for 7+ member rings¹⁴³ and benzene rings adjacent to heteroatom defects¹⁴². Again, this band is present in all samples derived from metal oxide modified precursors and to similar intensities. In Chapter 5, it was theorised that this band would arise in samples derived from particular polymer precursors (PET, PP, SP, and PAN) based on the products of thermal cracking in the first phase of the reactor. As discussed previously in this chapter, the inclusion of metal oxides as cracking catalysts may act to aid in the partial oxidation of the gaseous products before interaction with galinstan. This would give the liquid metal uniform sights on which to act, and thus standardise the product somewhat. This is theorised to explain the similarities in the POGC produced from metal oxide modified precursors.

Defect band, shoulder and defect band (D_s and D respectively) are both present in all sample. A schematic can be seen in Figure 6.16. However, it is here that we start to see some differentiation in samples based on the intensity of these bands. The defect bands are of primary interest in the Raman characterisation of carbons, alongside the graphitic bands discussed later. D_s is the result of assorted breathing modes for polyaromatic hydrocarbons (PAHs), while D is the combined breathing and Kekulé vibrations for PAHs. In highly ordered systems, a double resonance effect, coupled with degeneracy intensifies the D band peak¹⁴⁴. In less ordered systems, coupling of breathing and Kekulé modes results in the D band being blue shifted away from the expected 1350 cm^{-1} ¹⁴².

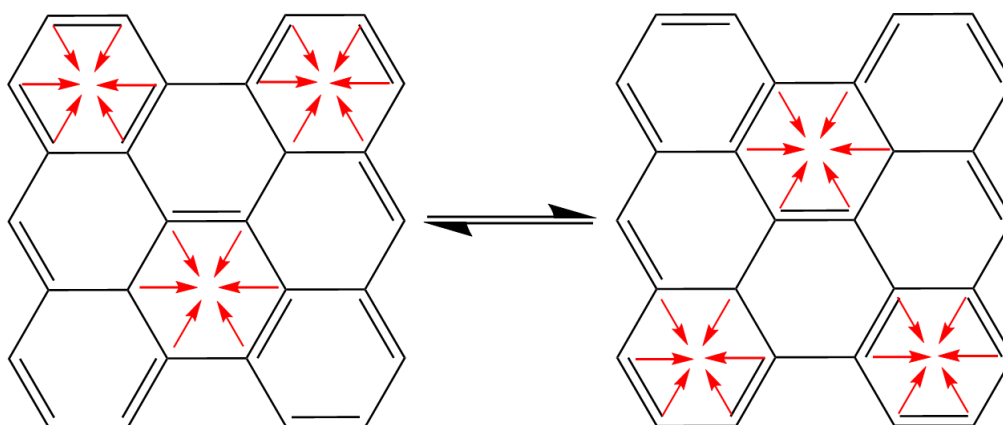


Figure 6.16: A schematic of Raman vibrational modes of graphene responsible for the D band.

This further differentiates the D and D_s bands, resulting in a more pronounced shoulder. Figure 6.17 shows the deconvoluted spectra for polyethylene derived carbon samples,

modified with alumina, silica, and zeolite (PE-AIDC, PE-SiDC, & PE-ZeDC respectively). It can be seen that amongst these samples, the intensities of both the D_5 and D bands are relatively consistent with one another.

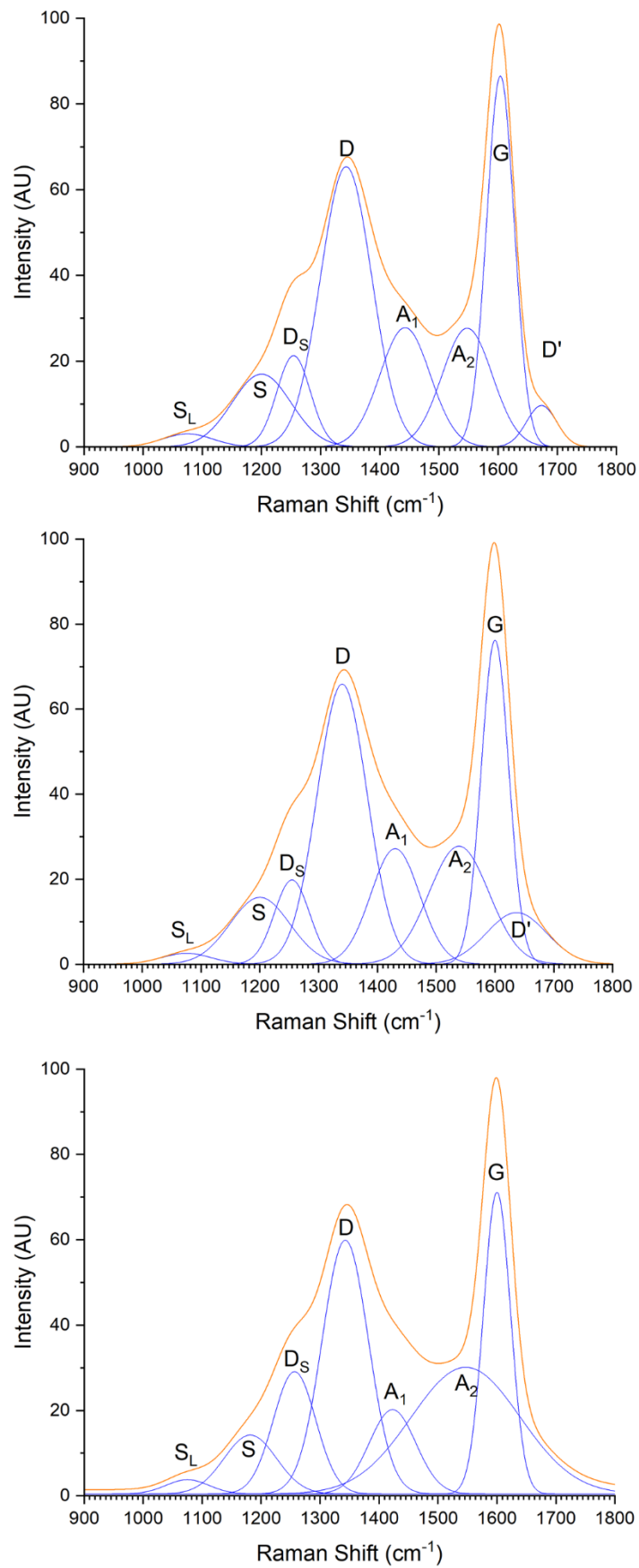


Figure 6.17: Raman spectra for polyethylene derived POGC modified with (top to bottom) alumina, silica, and zeolite.

Figure 6.18 shows the deconvoluted spectra for polypropylene derived carbon samples, modified with alumina, silica, and zeolite (PP-AIDC, PP-SiDC, & PP-ZeDC respectively). Here, a difference in relative intensities of these bands start to become notable with PP-AIDC presenting a high $D_5:D$ band intensity ratio, PP-SiDC falling more in line with the metal oxide modified polyethylene samples, and PET-Ze presenting a low $D_5:D$ band intensity ratio. The decrease in $D_5:D$ band ratio represents the sample becoming more ordered, and as such we can conclude that zeolite modified carbon produces more of an effect on the carbon lattice compared to alumina or silica modified samples. As discussed previously in this chapter, the methyl group present in the PP polymer chain represents an easy sight for oxidation to hydroxymethyl or aldehyde groups. Based on XRD analysis of the products, it suggests that zeolite modification did result in a product with a more ordered lattice, and that PP samples were a more susceptible to this effect. As such, this Raman result further supports this hypothesis. Finally, Figure 6.20 shows consistently low $D_5:D$ band ratios relative to other metal oxide modified samples. Based on the working theory of the galinstan acting on electronegative regions of organic molecules in contact with it, it follows that PET samples in general would produce low $D_5:D$ band ratios, as the structure is inherently oxygen rich, presenting many opportunities for the liquid metal to carbonise the samples.

Literature on the origin of the amorphous bands (A_1 and A_2) is lacking in consensus. However, agreement exists suggesting they originate from the presence of irregular structures^{145, 146}. Smith et al.¹⁴² identified two distinct amorphous bands with origins in different sources. A_1 is found between 1400 and 1460 cm^{-1} and is ascribed to the Kekulé vibrations coupled to symmetric breathing of adjacent cyclopentane rings and is strongly associated with out of plane deformation around these defects. A_2 is found between 1500 and 1550 cm^{-1} and is primarily the result of point defects which give rise to asymmetric stretching and breathing modes in nearby ring systems. Secondly, A_2 may also arise from nearby oxygen defects which restrict the asymmetric stretch modes and result in the A_2 peak being red shifted¹⁴². These amorphous bands are much more consistent in their intensities in the carbonaceous samples derived from metal oxide modified precursor materials compared to those derived from unmodified precursors presented in Chapter 5. Additionally, their intensities are also consistently lower. This suggests that, in general, carbonaceous samples derived from metal

oxide modified precursors produce fewer out of plane deformations, as well as defects that give rise to asymmetric stretching and breathing modes in ring systems, such as oxygen defects and dangling bonds¹⁴². There are three small exceptions to this however, as seen in PE-ZeDC (Figure 6.17), PET-SiDC, and PET-ZeDC (Figure 6.20). All of these samples demonstrate A_1 bands which are somewhat lower in intensity compared to other samples. This is attributed to a smaller degree of out of plane deformations resulting from 5 member ring structures in aromatic regions. This is possibly due to the presence of 6 member ring structures in the precursor, thus favourably forming more uniform polyaromatic regions and resulting in fewer out of plane deformations.

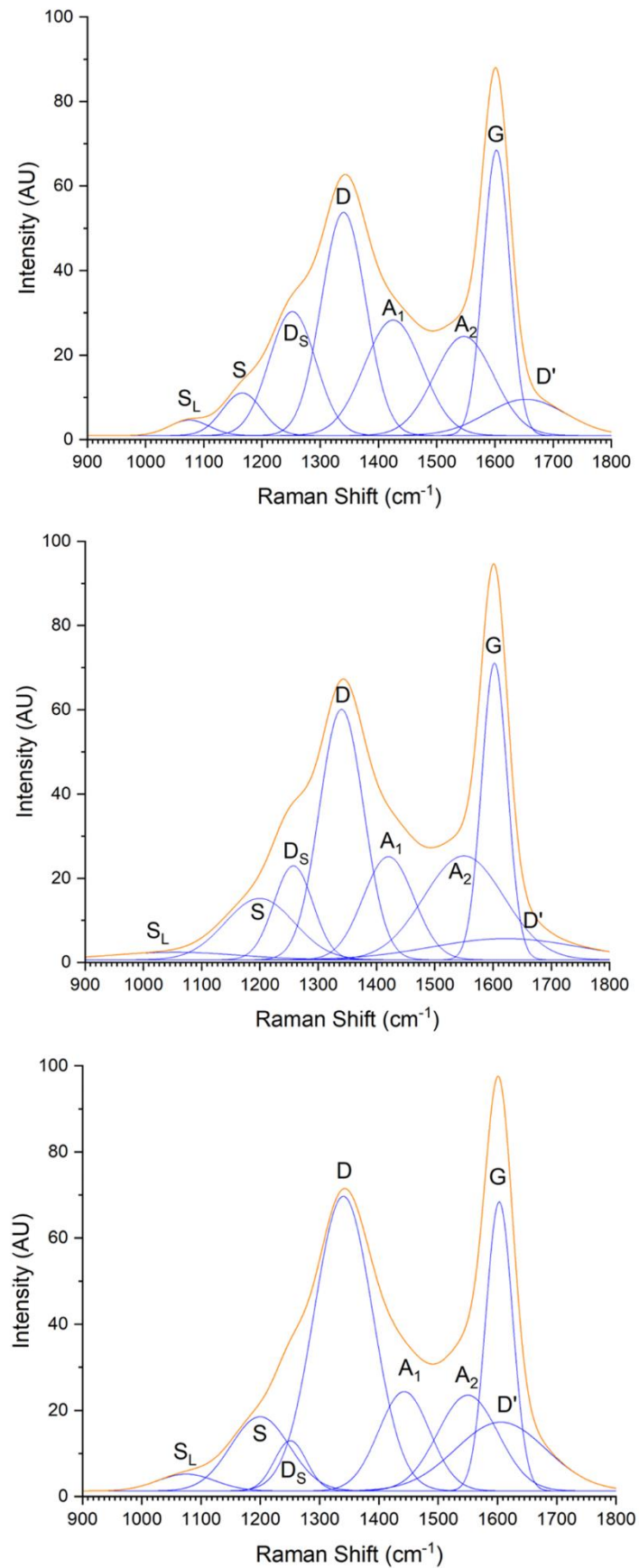


Figure 6.18: Raman spectra for polypropylene derived POGC modified with (top to bottom) alumina, silica, and zeolite.

The G-bands, like the D-bands, are peaks of primary interest in the Raman characterisation of carbons. They are well studied, and strongly associated with the asymmetric stretch of sp^2 carbons, particularly E_{2g} stretching in aromatic rings, shown in Figure 6.19. While E_{2g} stretching is present in an array of molecules, the overall system symmetry has a large effect on the area and intensity of the G-band peaks. As a result of the complexity of the makeup of the G-band region, it can be theoretically broken up into a Gaussian and Lorentzian model to describe PAH cluster sizes, system symmetry, and the effects of defects¹⁴². The Gaussian model is assigned to the distribution of small PAH structures, while the Lorentzian model is assigned to large PAH structures. However, in all the spectra, attempts at separating these G-band components consistently yielded a lower coefficient of determination. As such, differentiation could not be achieved, and the G-band was left as a single peak. Once again, this is thought to be the result of the Savitzky-Golay smoothing necessary for deconvolution likely masked the ability to differentiate these peaks.

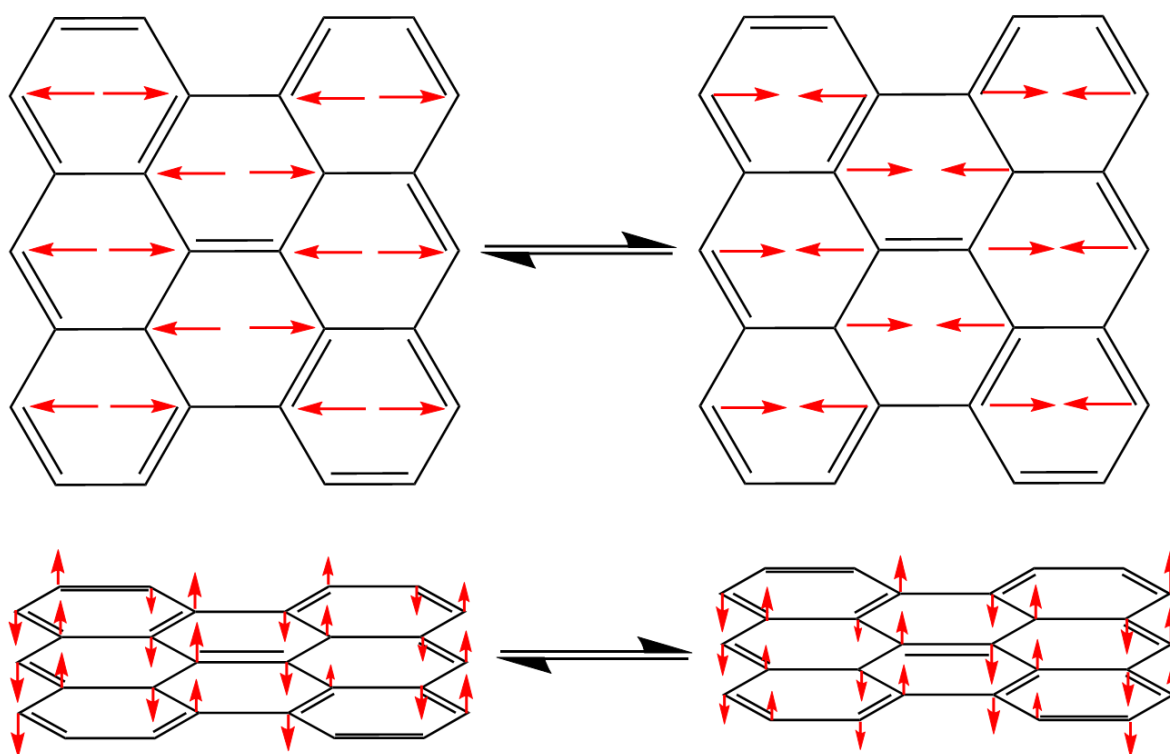


Figure 6.19: A schematic of Raman vibrational modes of graphene responsible for the G band.

G-bands in the carbonaceous samples derived from metal oxide modified precursors are significantly sharper and higher in intensity compared to those presented in Chapter 5. The

broadening of the G-band is generally associated with charge transfer, and lattice strain resulting from various forms of lattice defects. As such, the sharp and prominent G-band peaks present in these samples suggests that the addition of metal oxides to the precursor materials has the effect of producing more uniform lattices in the resulting carbon structure, based on the mechanisms outlined above. Structurally, this suggests that precursor modification results in larger aromatic regions in the POGC when compared to unmodified precursor samples.

In Smith et al.'s¹⁴² study, a D' band was proposed. It is assigned to the weak breathing mode of a central ring surrounded by asymmetric stretching behaviour. This band was only shown to be significant in coronene and cycloheptene centred ring systems. The D' band was present in all samples to similar extents apart from the PE-ZeDC and PET-AIDC. Where the D' band is present, it is generally far more consistent in intensity between samples in comparison to those presented in Chapter 5. The exception to this is in the PET-ZeDC sample, where the intensity was lower than others generally presented. This may be the result of a particularly prominent C band present in this sample, making the difference between the major G band peak and the prominent C band peak difficult to discern. Finally, of the two samples which did not demonstrate D' bands, PE-ZeDC is most easily explained by the full width half maximum of the A₂ band drowning out the presence of this band in the signal. The broadening of this band is typically associated with irregular oxygen defects in the lattice, causing the peak to be red shifted¹⁴². Lastly, PET-AIDC was the only sample to not demonstrate a prominent D' band which could also not be explained by interference with other peaks. This suggests that this sample had a lesser degree of coronene and cycloheptene centred rings. The A₁ band someone hints at the presence of cycloheptene centred ring systems in this sample, and so likely this is the result of a deficit in coronene centred rings. This suggests that the degree of polyaromaticity is lower in this sample than other. However, that does not seem to be entirely supported, as the G:D band ratio shown in Figure 6.15.

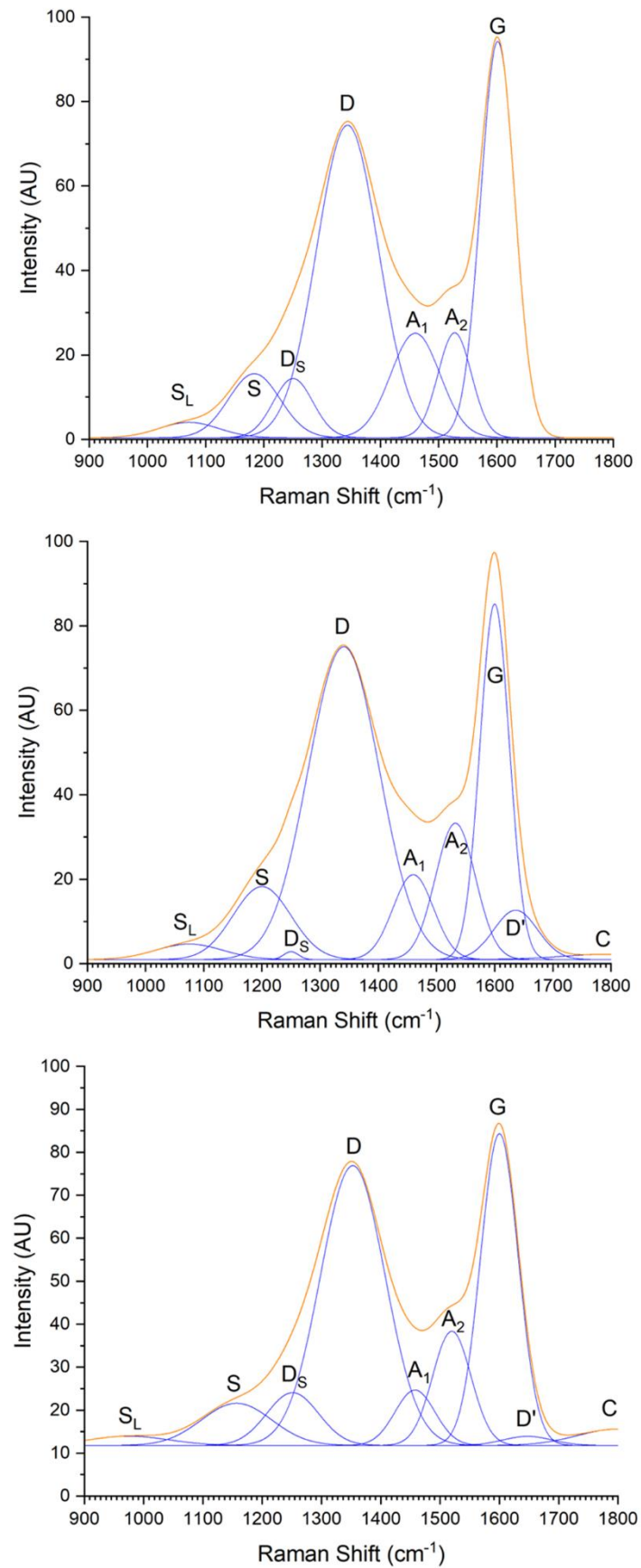


Figure 6.20: Raman spectra for polyethylene terephthalate derived POGC modified with (top to bottom) alumina, silica, and zeolite.

Finally, the presence of carbonyl stretching can lead to a very weak band appearing in between 1750 and 1800 cm^{-1} ¹⁴². This band would be expected to become more prominent in metal oxide modified carbon samples based on the prediction of the formation of hydroxymethyl and aldehyde groups in precursors before carbonisation in galinstan where they could easily form carbonyl groups. The C band was not observable in any samples from unmodified precursor materials. In contrast, two of the carbon samples from metal oxide modified precursors demonstrated this very weak band; PET-SiDC and PET-ZeDC. Additionally, while almost all carbon samples from unmodified precursors showed no signs of a signal beyond the range of the D' peak, four further carbon samples from modified metal oxide precursors have D' bands with high full width half maximums causing this peak to extend into the range of the C band. It is possible that this peak is present in these samples but cannot be deconvoluted from the D' peak. However, this is purely speculative.

6.5.3: X-ray photoelectron spectroscopy

X-Ray photoelectron spectroscopy (XPS) was employed to analyse the surface components of the synthesised carbons as well as the nature of the bonds present between species. The samples exhibited broadening and asymmetry of the singular $\text{C}1s$ peak which cannot be ascribed to the core hole effect, or gaussian broadening¹⁶⁶. As such, other components must be responsible for this feature of the spectra. The figures reported have been deconvoluted according to peak assignments by Levi et al.¹⁶⁶.

General trends remain consistent with observations made in Chapter 5 with the surface of samples consisting primarily of carbon, with a degree of oxygen in varying proportions. Once again, it is notable that carbon chars tend to chemisorb surface oxygens at low temperatures¹⁶⁶. However, at room temperature, these effects are minimal. As such, a small degree of surface oxygen species may not be indicative of the plastics interaction with the liquid metal, or oxygen impurities in the system, but rather from atmospheric chemisorption post-carbonisation.

Table 6.3 shows the atomic percentages of surface oxygen from various modified plastic derived carbons as determined by XPS wide scan. Chapter 5 shows that the oxygen content of representative unmodified plastic derived carbon samples is 6.54, 9.09, and 23.72 at.% for PE, PP, and PET respectively. Samples derived from modified plastic precursors follow similar trends, with oxygen content of modified PE, PP, and PET samples averaging 4.64,

8.86, and 10.93 at.% respectively. From this, a similar trend emerges of PE derived samples containing the least surface oxygen, PET derived samples containing the most, and PP falling in between. However, these averages fall consistently lower than those obtained from unmodified samples; particularly in the case of PET which falls considerably lower.

Carbon derived from PE with silica and zeolite modifications fall more in line with expected values from unmodified PE with 5.51 and 6.56 at.% surface oxygen respectively. Alumina modified samples however demonstrated significantly lower degrees of surface oxidation at 1.85 at. %. This difference will be further examined in the discussion of the high-resolution spectra.

Table 6.3: Atomic percentages of surface oxygen from various modified plastic derived carbons as determined by XPS wide scan.

Plastic precursor and modification	Carbon (at.%)	Oxygen (at.%)
Polyethylene-alumina	98.15	1.85
Polyethylene-silica	94.49	5.51
Polyethylene-zeolite	93.44	6.56
Polypropylene-alumina	90.57	9.43
Polypropylene-silica	90.61	9.39
Polypropylene-zeolite	92.24	7.76
Polyethylene Terephthalate-alumina	89.58	10.42
Polyethylene Terephthalate-silica	87.13	12.87
Polyethylene Terephthalate-zeolite	90.49	9.51

In analysing whether the oxygen content of samples in this chapter is endogenous to the interaction of the reactants, a comparison must be drawn with those samples of the previous chapter. Experimental setup remained unchanged besides the addition of metal oxides to the precursor plastics. Therefore, the degree of oxidation of the POGC is dependent on the presence of metal oxides. The most significant difference is in the degree of oxidation of modified PET samples, which decreased significantly from unmodified PET. Given conclusions based on analysis of Raman spectra, PET samples likely did not undergo further oxidation of the gaseous plastic fractions due to the large degree of oxygen already present in its structure. Instead, the metal oxides may have acted primarily as a thermal cracking catalyst, making previously unfavourable scission reactions more favourable. From literature, enthalpy of dissociation between C-C bonds is 618.3 ± 15.4 , while C-O bonds is 1076.38 ± 0.67^{183} . As such, the primary scission sight in the PET chain would be between aliphatic C-C bonds. The

introduction of a cracking catalyst may change the thermodynamics of this process and make aliphatic C-O bond scission occur at higher rates than it otherwise would. This would lead to smaller oxygen containing fraction which would then interact with galinstan in a similar mechanism proposed above, thus leading to less structural oxygen in the POGC product.

In Figure 6.21, Figure 6.22, Figure 6.23, Figure 6.24, Figure 6.25, Figure 6.26, Figure 6.27, Figure 6.28, and Figure 6.29 the high resolution C1s and O1s spectra of the various modified polymer derived carbon samples are presented. The red and black lines represent the experimental curves, and deconvolution best fit respectively. The primary peak at 284.5 eV represents aliphatic and aromatic sp^2 bonded carbon species and corroborates the Raman analysis confirming the presence of aromatic and aliphatic regions of the POGC. The asymmetry and broadening of the experimental curve could not be deconvoluted using only one peak, and so peak assignments and deconvolution were performed in such a way as to achieve the lowest possible coefficient of determination between the line of best fit and the experimental curve.

In Figure 6.21, Figure 6.22, and Figure 6.23, PE-AIDC, PE-SiDC, and PE-ZeDC samples showed three carbon species, as well as a small degree of oxidation. An atomic ratio of $\sim 3:1$ exists between sp^2 and sp^3 carbon species, indicating a high degree of graphitisation of the samples. This follows the Raman observation that the sample consists of large polyaromatic regions connected by aliphatic chains. Furthermore, a small degree of carbon vacancies exists within the POGC, likely attributed to the dangling bonds observed in the A_2 band of the Raman spectra. This is particularly pronounced in the case of PE-ZeDC. In comparison with samples derived from unmodified PE precursors, a higher ratio of $sp^2:sp^3$ bonds exist, reinforcing the theory that the addition of metal oxides results in a higher degree of graphitisation, as suggested by the G:D band ratios presented in Figure 6.15. Furthermore, a significantly lower degree of carbon vacancies follows the observation that the various defect related Raman bands were decreased in intensity from these samples. The PE-ZeDC sample was an exception to this statement with a high degree of carbon vacancies at 12.47 at%. This supports the Raman result of a broad A_2 band which arises from defects that give rise to asymmetric stretching and breathing modes in ring systems, such as oxygen defects and dangling bonds¹⁴².

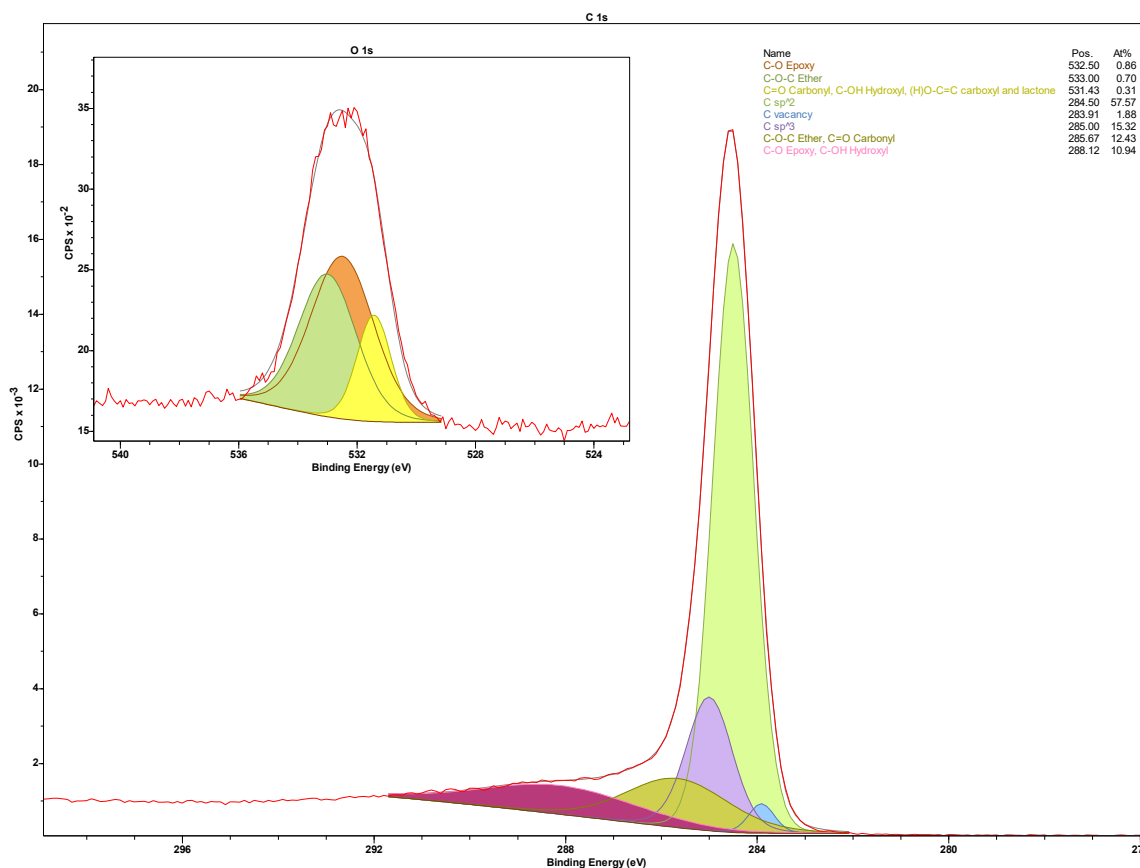


Figure 6.21: High resolution C1s and O1s spectra of polyethylene-alumina derived carbon.

The O1s spectra in Figure 6.21 shows a relatively consistent distribution speciation between various oxygen bonds present. However, with the very low degree of oxygen present in this sample, they are likely to be more effected by oxygen chemisorption than other samples. The PE-SiDC sample contains much more oxygen, and here the O1s spectrum in Figure 6.22 shows a higher degree of ether and epoxy species in the POGC, with a much smaller amount of other species. The O1s spectrum of PE-ZeDC further differs with a high degree of selectivity towards epoxy bonds specifically. This differs from observations of the unmodified PEDC sample where carbonyl, hydroxyl, carboxyl and lactone speciation are dominant. The formation of oxygen bonds which are structurally intrinsic such as epoxies and ethers are most likely indicative that much of the oxygen present is the result of the carbonisation process, rather than atmospheric chemisorption, as these bonds are unlikely to form under atmospheric conditions. Conversely, carbonyl, hydroxyl, carboxyl and lactone groups may more readily form at carbon vacancies, or substitute with protons.

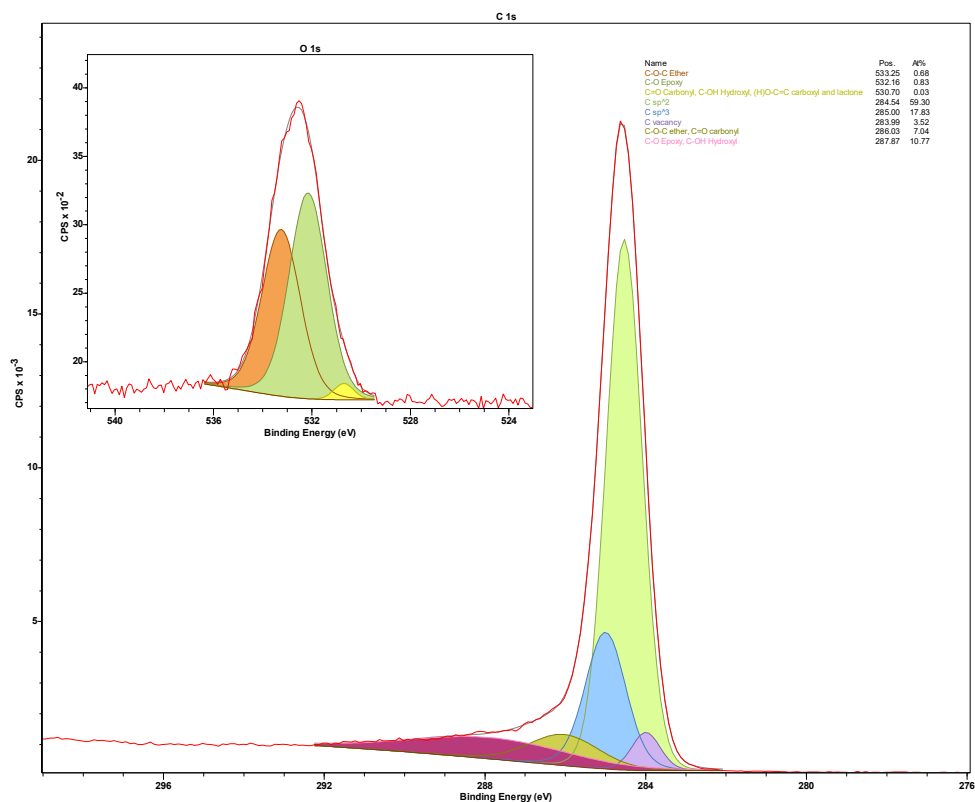


Figure 6.22: High resolution C1s and O1s spectra of polyethylene-silica derived carbon.

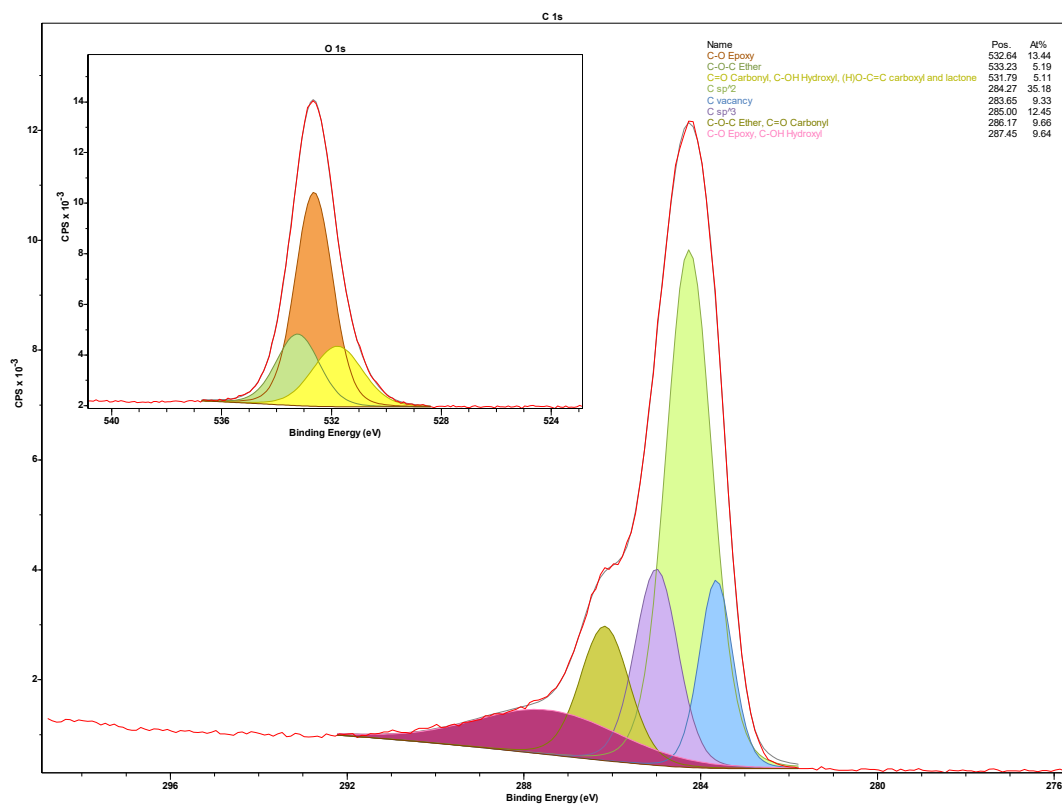


Figure 6.23: High resolution C1s and O1s spectra of polyethylene-zeolite derived carbon.

Figure 6.24, Figure 6.25, and Figure 6.26 show the C1s and O1s spectra of PP-AIDC, PP-SiDC, and PP-ZeDC respectively. These samples show a lower $sp^2:sp^3$ bond ratio when compared to modified PE derived samples at $\sim 2:1$. This suggests a higher degree of aliphatic chain presence in the POGC structure, or the presence of more saturated cyclic structures. Of note is the much lower degree of carbon vacancies, averaging 0.18 at%.

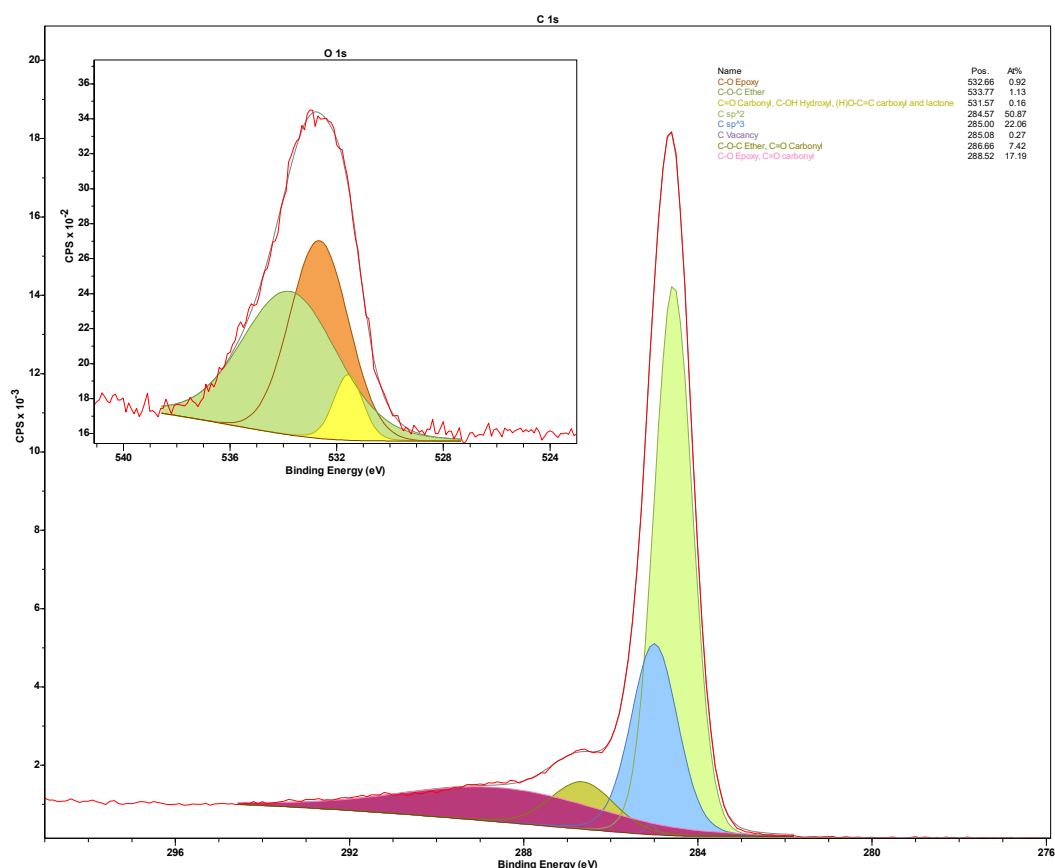


Figure 6.24: High resolution C1s and O1s spectra of polypropylene-alumina derived carbon.

O1s spectra of these samples continue to show a preference for the formation of ether and epoxy bonds to a significant degree. This further supports conclusions made to the nature of oxidation of the POGC in the discussion of the modified PE derived carbons O1s spectra.

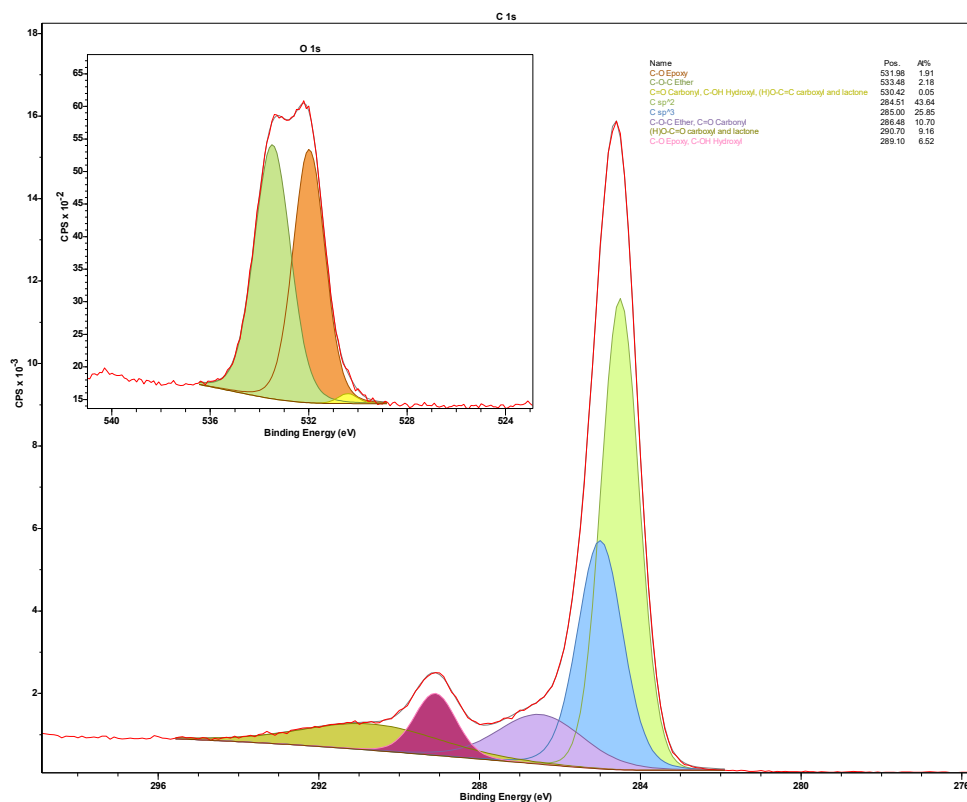


Figure 6.25: High resolution C1s and O1s spectra of polypropylene-silica derived carbon.

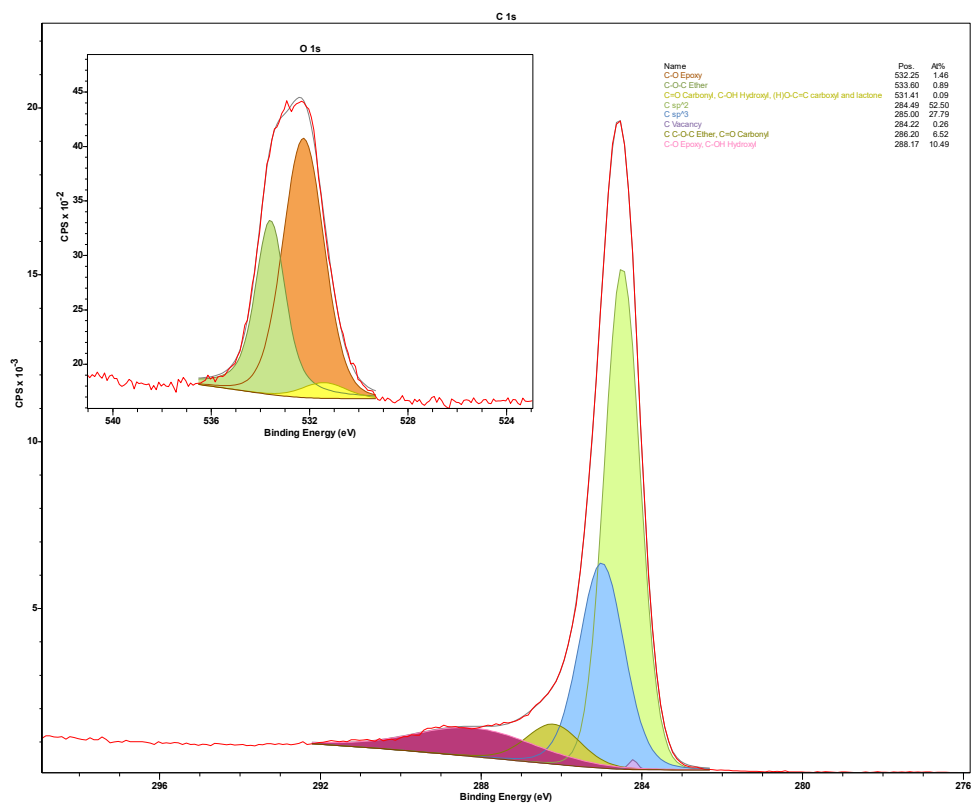


Figure 6.26: High resolution C1s and O1s spectra of polypropylene-zeolite derived carbon.

Figure 6.27, Figure 6.28, and Figure 6.29 show the C1s and O1s spectra of the modified PET derived samples. Here we see an extremely high degree of graphitisation, with $sp^2:sp^3$ bond ratios at $\sim 4:1$, with a strong selection preference for sp^2 carbon. Carbon vacancies also reappear to a large degree which is in support of Raman observations of particularly prominent A_2 bands in these samples. This suggest that polyaromatic regions of modified PET derived samples are larger, however are prone to more lattice defects.

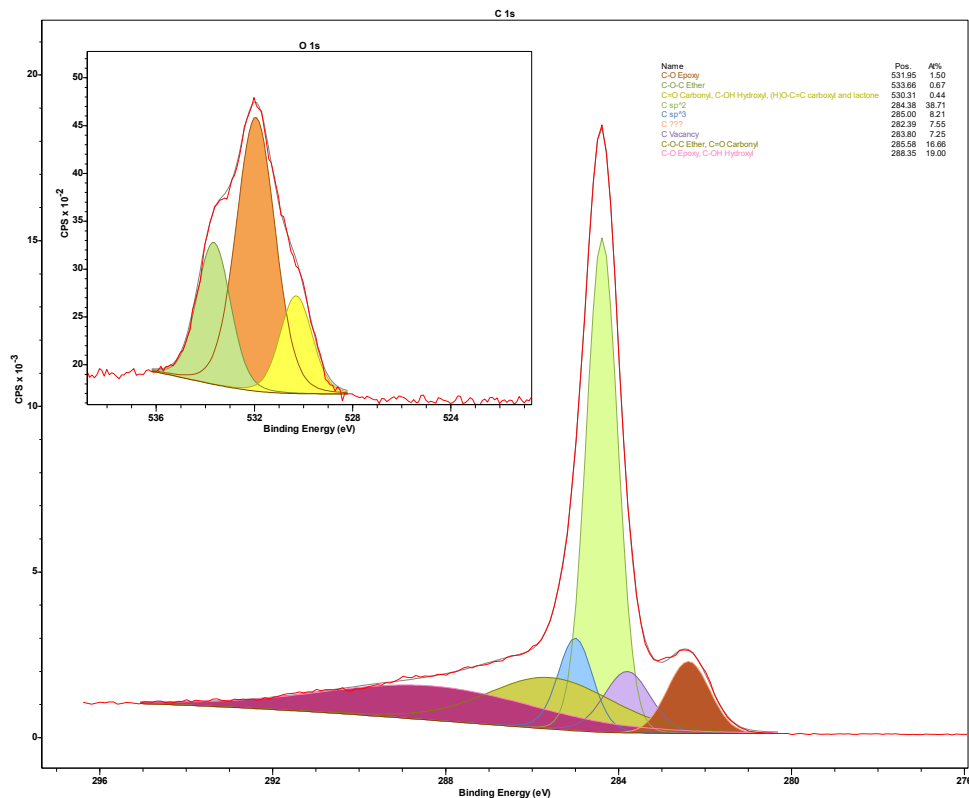


Figure 6.27: High resolution C1s and O1s spectra of polyethylene terephthalate-alumina derived carbon.

Table 6.3 shows that modified PET samples contain the most oxygen, which follows from observations made in Chapter 5. This suggest that oxygen endogenous to the PET structure continues to carry forward into the structure of POGC. However, it is also notable that the at% oxygen in the modified precursor samples is approximately half that of the unmodified samples. Further, we see a much higher degree of carbonyl, hydroxyl, carboxyl and lactone groups present in the modified PET derived samples as compared to other modified polymer samples. This suggests that the preferred modality for incorporation of endogenous oxygen is towards these types of bonds, while exogenous oxygen may play more of a role in the formation of ether and epoxy bonds.

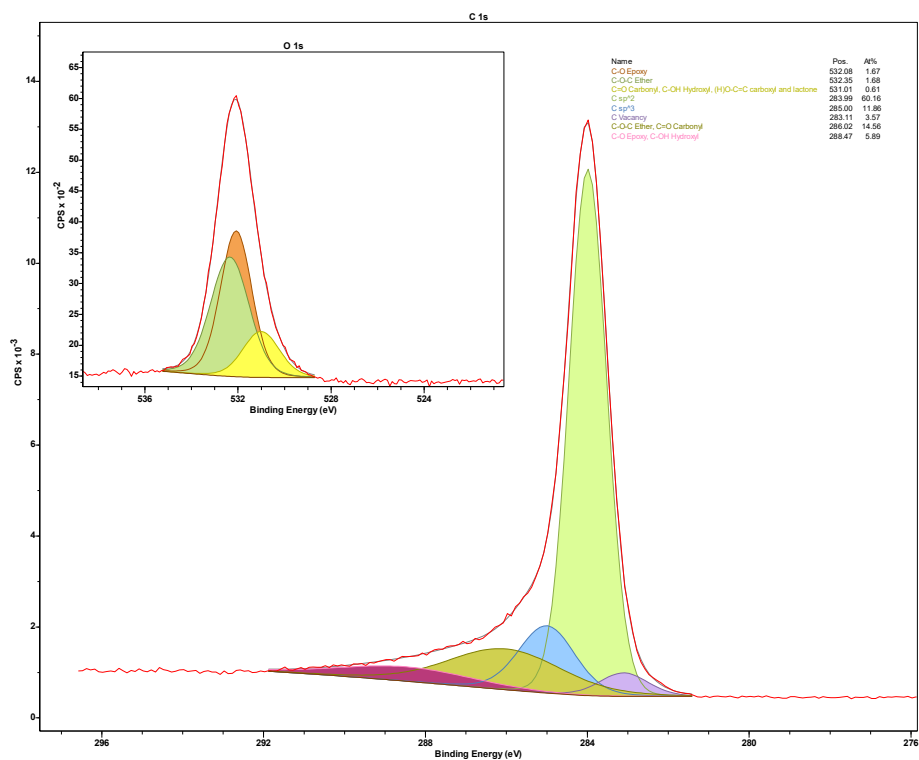


Figure 6.28: High resolution C1s and O1s spectra of polyethylene terephthalate-silica derived carbon.

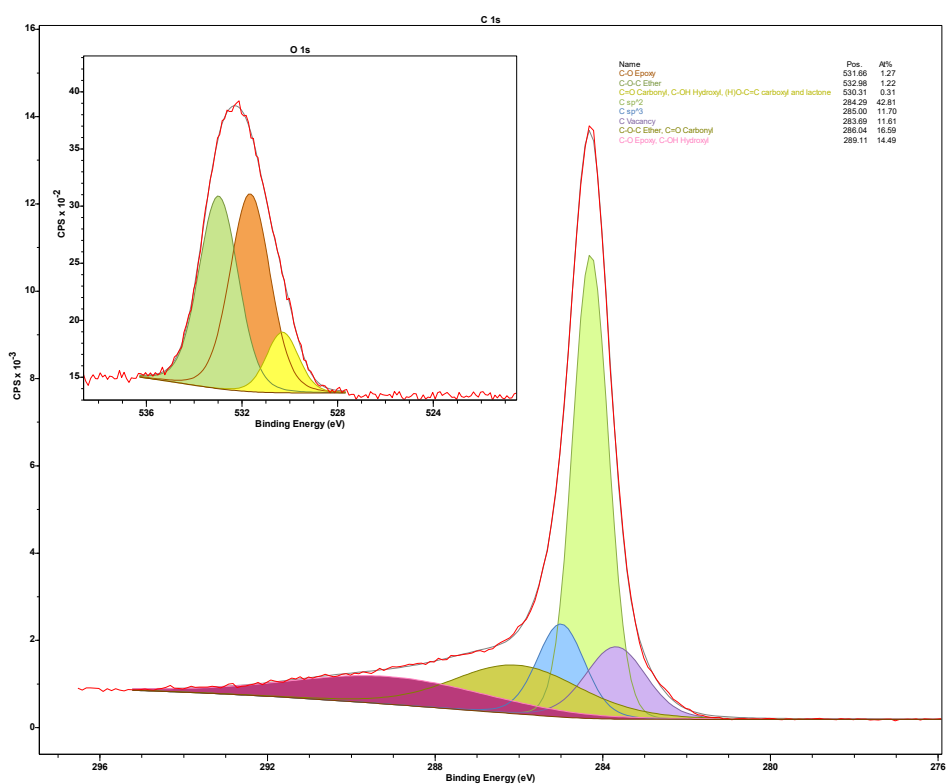


Figure 6.29: High resolution C1s and O1s spectra of polyethylene terephthalate-zeolite derived carbon.

6.6: Summary of findings

- The modification process may have very minor effects on the polymer structure prior to carbonisation.
- Modification of precursors with metal oxides increases yields.
- The modification of precursors with metal oxides reduces lattice defects in the produced carbonaceous product than that of unmodified precursors.
- The degree of sp^2 hybridisation of partially oxidised graphitic carbon produced from modified precursors increases significantly compared to unmodified precursors.
- The consistency of the carbon products from modified precursors increases between different plastics when compared to unmodified precursors.

Chapter 7: Conclusions and future work

7.1: Conclusions

A reactor was designed, tested, and optimised to achieve the aims of this project. Gallium, EGaln, galinstan and EBiSn liquid metals were examined for their suitability for this reaction. Gallium produced no carbonisation. EBiSn was inconclusive as its higher melting point resulted in damage to glassware and an inability to retrieve the carbon product using the outlined post-processing method. EGaln and galinstan produced a retrievable carbonaceous product with galinstan producing marginally better carbonaceous products with larger regions of aromaticity. However, due to galinstan's lower melting point, it was considered more suitable for post-processing and collection of the carbonaceous products.

Carbonaceous materials were successfully produced from sources of waste and virgin plastics at low temperatures using galinstan. Structural analysis using Raman spectroscopy showed that the carbonaceous products were largely amorphous and likely a form of partially oxidised graphitic carbon. Different polymers produced different carbonaceous structures, with PAN and PE producing the most graphitic structures, and PP and PET yielding a more amorphous product with regions of aromaticity, and PS producing a large degree of defects in the lattice. Nylon 6/6 resulted in system blockages and was unable to be carbonised. XPS showed that formation of sp^2 bonded carbons were preferred over sp^3 bonded carbons. Carbonyl bonds were shown to be the preferential modality of oxygen incorporation into the carbon products structure.

The plastic precursors were successfully composited with alumina, silica, and zeolite. This modification process improved visual yields. Carbonaceous products of modified plastic precursors produced a more consistent carbon product with higher degrees of aromaticity and fewer lattice defects compared to unmodified counterparts. The degree of sp^2 hybridisation of partially oxidised graphitic carbon produced from modified precursors increases significantly compared to unmodified precursors.

7.2: Future work

This work successfully demonstrated the use of galinstan to decompose plastics at low temperatures on a lab scale. However, due to limitations with the reactor the yields remained extremely low throughout the experiments. For future exploration of this concept, several key issues must be overcome to increase the conversion rate of the process. The first reactor

design limitation is in the connection between the two heating zones. As discussed in chapters 4 and 5, a significant degree of condensation of polymer occurred between these two heating zones, leading to low conversion rates. A custom furnace design which could maintain system temperatures above the vaporisation temperature of the plastics would allow for more interaction between the polymer vapour and the LM.

Furthermore, the role of the carrier gas diluting the polymer vapour and leading to a shielding effect between polymer vapour and LM was also discussed in Chapter 4. The ability to eliminate this carrier gas would allow for further interactions between polymer vapour and LM. This could be achieved using a smaller initial heating zone to vaporise the plastic. The autogenous pressure generated from the transition from solid plastic to polymer gas could be used to carry the vapours through the system, eliminating the need for argon. Furthermore, a feed system to replenish vaporised plastic could sustain this pressure generation indefinitely.

Finally, the injection method of polymer vapour into the LM could be improved. Due to the high surface tension of the LM, it is difficult to achieve gas injection into the LM bulk. More commonly, gas bubbles would transition to the interface between the glassware and the LM, rather than bubbling through the LM bulk. Additionally, due to the density of LM, there is a positive relationship between pressure and residence time. To increase the residence time of the gas bubbles, the depth of LM must be increased. This can eventually lead to a coalescence of bubbles within the LM, thus lowering the gas surface area, and lowering the interaction between polymer vapour and LM. To fix this, a series of extremely fine needles protruding from a manifold could be used to maintain the smallest possible gas bubbles, as well as to achieve a distributed spread of gas within the LM bulk. This would simultaneously minimise the effects of bubble coalescence as well as the occurrence of gas bubbles working their way to the interface between glass and LM.

In addition to reactor design improvements, modifications to the liquid metal would be an interesting pathway to explore. Supported catalytically active liquid metals (SCALMs) are discussed in Chapter 2. Experimentation with various catalysts using LM for a support may result in higher yields, or different or even controllable carbon morphologies.

8: References

1. A. Rahimi and J. M. García, *Nature Reviews Chemistry*, 2017, **1**, 0046.
2. C. Zhuo and Y. A. Levendis, *Journal of Applied Polymer Science*, 2014, **131**.
3. S. K. a. T. O. K. Matsumoto, U.S.A, 1975.
4. N. F. M. Yunus, M. Zaharia, M. A. Idris, D. Nath, R. Khanna and V. Sahajwalla, *Energy & Fuels*, 2011, **26**, 278-286.
5. V. G. Pol, *Environmental science & technology*, 2010, **44**, 4753-4759.
6. C. Mohanraj, T. Senthilkumar and M. Chandrasekar, *Int J Energy Res*, 2017, **41**, 1534-1552.
7. S. Al-Salem, P. Lettieri and J. Baeyens, *Waste management*, 2009, **29**, 2625-2643.
8. K. F. Drain, W. R. Murphy and M. S. Otterburn, *Conservation & Recycling*, 1981, **4**, 201-218.
9. F. Ackerman, *Local Environment*, 2000, **5**, 223-229.
10. K. S. Novoselov, A. K. Geim, S. V. Morozov, D. Jiang, M. I. Katsnelson, I. V. Grigorieva, S. V. Dubonos and A. A. Firsov, *Nature*, 2005, **438**, 197.
11. M. D. Stoller, S. Park, Y. Zhu, J. An and R. S. Ruoff, *Nano letters*, 2008, **8**, 3498-3502.
12. N. Borsodi, A. Szentes, N. Miskolczi, C. Wu and X. Liu, *Journal of Analytical and Applied Pyrolysis*, 2016, **120**, 304-313.
13. K. A. Ritter and J. W. Lyding, *Nature Materials*, 2009, **8**, 235.
14. K. P. Loh, Q. Bao, P. K. Ang and J. Yang, *Journal of Materials Chemistry*, 2010, **20**, 2277-2289.
15. L. Lin, H. Peng and Z. Liu, *Nature materials*, 2019, **18**, 520-524.
16. G. Ruan, Z. Sun, Z. Peng and J. M. Tour, *ACS nano*, 2011, **5**, 7601-7607.
17. H. Jin, X. Wang, Z. Gu, G. Anderson and K. Muthukumarappan, *Journal of Environmental Chemical Engineering*, 2014, **2**, 1404-1409.
18. D. Serrano, J. Aguado, J. Escola, E. Garagorri, J. Rodríguez, L. Morselli, G. Palazzi and R. Orsi, *Applied Catalysis B: Environmental*, 2004, **49**, 257-265.
19. T. Somanathan, K. Prasad, K. K. Ostrikov, A. Saravanan and V. M. Krishna, *Nanomaterials*, 2015, **5**, 826-834.
20. S. Sharma, G. Kalita, R. Hirano, S. M. Shinde, R. Papon, H. Ohtani and M. Tanemura, *Carbon*, 2014, **72**, 66-73.
21. L. Cui, X. Wang, N. Chen, B. Ji and L. Qu, *Nanoscale*, 2017, **9**, 9089-9094.
22. H. Jin, X. Wang, Z. Gu, Q. Fan and B. Luo, *Journal of Power Sources*, 2015, **273**, 1156-1162.
23. H. M. Jeong, J. W. Lee, W. H. Shin, Y. J. Choi, H. J. Shin, J. K. Kang and J. W. Choi, *Nano letters*, 2011, **11**, 2472-2477.
24. N. Singh, D. Hui, R. Singh, I. Ahuja, L. Feo and F. Fraternali, *Composites Part B: Engineering*, 2017, **115**, 409-422.
25. Y. Moriguchi and A. Terazono, *The International Journal of Life Cycle Assessment*, 2000, **5**, 281.
26. E. Dlugokencky and P. Tans, Trends in Atmospheric Carbon Dioxide, <https://www.esrl.noaa.gov/gmd/ccgg/trends/global.html>, (accessed 19/05/2017, 2017).
27. EEA, Recycling Rates in Europe, <https://www.eea.europa.eu/about-us/competitions/waste-smart-competition/recycling-rates-in-europe/image-view-fullscreen>, (accessed 12/02/2019, 2019).

28. U. EPA, *Advancing Sustainable Materials Management*, Report EPA530-F-18-004, United States Government, Washington DC, 2018.
29. A. Kärrman, C. Schönlau and M. Engwall, *Exposure and effects of microplastics on wildlife: A review of existing data*, Örebro universitet, 2016.
30. M. Sigler, *Water, Air, & Soil Pollution*, 2014, **225**, 2184.
31. R. Andrady and M. Gregory, *Plastics in the marine environment: in: Plastics and the environment*, edited by A. L. Andrady, New York, NY: Wiley, 2003.
32. S. D. Anuar Sharuddin, F. Abnisa, W. M. A. Wan Daud and M. K. Aroua, *Energy Conversion and Management*, 2016, **115**, 308-326.
33. J. A. Onwudili, N. Insura and P. T. Williams, *Journal of Analytical and Applied Pyrolysis*, 2009, **86**, 293-303.
34. R. Miranda, J. Yang, C. Roy and C. Vasile, *Polymer degradation and stability*, 1999, **64**, 127-144.
35. R. Miranda, J. Yang, C. Roy and C. Vasile, *Polymer Degradation and stability*, 2001, **72**, 469-491.
36. S.-H. Jung, M.-H. Cho, B.-S. Kang and J.-S. Kim, *Fuel Processing Technology*, 2010, **91**, 277-284.
37. P. A. Vo Dong, C. Azzaro-Pantel and A.-L. Cadene, *Resources, Conservation and Recycling*, 2018, **133**, 63-75.
38. R. A. M. Meneses, G. Cabrera-Papamija, F. Machuca-Martínez, L. A. Rodríguez, J. E. Diosa and E. Mosquera-Vargas, *Heliyon*, 2022.
39. Y.-J. Lee, *Journal of Nuclear Materials*, 2004, **325**, 174-179.
40. J. D. Wiggins-Camacho and K. J. Stevenson, *The Journal of Physical Chemistry C*, 2009, **113**, 19082-19090.
41. A. Primo, P. Atienzar, E. Sanchez, J. M. Delgado and H. García, *Chemical communications*, 2012, **48**, 9254-9256.
42. K. H. An, W. S. Kim, Y. S. Park, J. M. Moon, D. J. Bae, S. C. Lim, Y. S. Lee and Y. H. Lee, *Advanced functional materials*, 2001, **11**, 387-392.
43. M. Toupin, D. Bélanger, I. R. Hill and D. Quinn, *Journal of power sources*, 2005, **140**, 203-210.
44. S. Chen, Z. Liu, S. Jiang and H. Hou, *Science of the Total Environment*, 2020, **710**, 136250.
45. M. Inagaki, K. C. Park and M. Endo, *New Carbon Materials*, 2010, **25**, 409-420.
46. M. A. Fox and J. K. Whitesell, *Organische Chemie: Grundlagen, Mechanismen, Bioorganische Anwendungen*, Spektrum Akad. Verlag, 1995.
47. T. Cottrell, *The strengths of chemical bonds*, Butterworths, London, 2nd Edition edn., 1958.
48. J. B. Mann, T. L. Meek and L. C. Allen, *Journal of the American Chemical Society*, 2000, **122**, 2780-2783.
49. S. V. Levchik and E. D. Weil, *Polymers for Advanced Technologies*, 2004, **15**, 691-700.
50. I. Lewis, *Carbon*, 1982, **20**, 519-529.
51. D. Choi, D. Jang, H.-I. Joh, E. Reichmanis and S. Lee, *Chemistry of Materials*, 2017, **29**, 9518-9527.
52. B. Kaur, J. Singh, R. K. Gupta and H. Bhunia, *Journal of environmental management*, 2019, **242**, 68-80.
53. W.-h. Lee and J. H. Moon, *ACS applied materials & interfaces*, 2014, **6**, 13968-13976.

54. Y. Yang, F. Simeon, T. A. Hatton and G. C. Rutledge, *Journal of applied polymer science*, 2012, **124**, 3861-3870.
55. I. Karacan and K. Ş. Tunçel, *Polymer degradation and stability*, 2013, **98**, 1869-1881.
56. Y. Wen, K. Kierzek, X. Chen, J. Gong, J. Liu, R. Niu, E. Mijowska and T. Tang, *Waste management*, 2019, **87**, 691-700.
57. S. Chen, G. He, H. Hu, S. Jin, Y. Zhou, Y. He, S. He, F. Zhao and H. Hou, *Energy & Environmental Science*, 2013, **6**, 2435-2439.
58. J. Kou and L.-B. Sun, *Industrial & Engineering Chemistry Research*, 2016, **55**, 10916-10925.
59. M. Ilyas, W. Ahmad and H. Khan, *Water Science and Technology*, 2021, **84**, 609-631.
60. F. Xu, Z. Tang, S. Huang, L. Chen, Y. Liang, W. Mai, H. Zhong, R. Fu and D. Wu, *Nature communications*, 2015, **6**, 7221.
61. T. Hu, Y. Li, W. Gao, X. Wang and Y. Tian, *Microporous and Mesoporous Materials*, 2019, **279**, 234-244.
62. C. Su, L. Bai, H. Zhang, K. Chang, G. Li and S. Li, *Russian Journal of Physical Chemistry A*, 2019, **93**, 1762-1768.
63. S. Mohsenian, M. S. Esmaili, J. Fathi and B. Shokri, *International Journal of hydrogen energy*, 2016, **41**, 16656-16663.
64. P. K. Tripathi, S. Durbach and N. J. Coville, *Applied Sciences*, 2019, **9**, 2451.
65. J. Gong, J. Liu, X. Chen, X. Wen, Z. Jiang, E. Mijowska, Y. Wang and T. Tang, *Microporous and Mesoporous Materials*, 2013, **176**, 31-40.
66. X.-M. Liu, Z. dong Huang, S. woon Oh, B. Zhang, P.-C. Ma, M. M. Yuen and J.-K. Kim, *Composites Science and Technology*, 2012, **72**, 121-144.
67. T. Tang, X. Chen, X. Meng, H. Chen and Y. Ding, *Angewandte Chemie*, 2005, **117**, 1541-1544.
68. N. Mishra, G. Das, A. Ansaldo, A. Genovese, M. Malerba, M. Povia, D. Ricci, E. Di Fabrizio, E. Di Zitti, M. Sharon and M. Sharon, *Journal of Analytical and Applied Pyrolysis*, 2012, **94**, 91-98.
69. U. Narula, C. M. Tan and C. S. Lai, *Microelectronics Reliability*, 2016, **61**, 87-90.
70. U. Narula, C. M. Tan and C. S. Lai, *Scientific reports*, 2017, **7**, 44112.
71. J. Gong, J. Liu, D. Wan, X. Chen, X. Wen, E. Mijowska, Z. Jiang, Y. Wang and T. Tang, *Applied Catalysis A: General*, 2012, **449**, 112-120.
72. D. C. Nath and V. Sahajwalla, *Materials Sciences and Applications*, 2012, **3**, 103.
73. A. K. Geim, *science*, 2009, **324**, 1530-1534.
74. Z. Wang, H. Ogata, S. Morimoto, M. Fujishige, K. Takeuchi, Y. Hashimoto and M. Endo, *Carbon*, 2014, **72**, 421-424.
75. X. Wang, H. You, F. Liu, M. Li, L. Wan, S. Li, Q. Li, Y. Xu, R. Tian and Z. Yu, *Chemical Vapor Deposition*, 2009, **15**, 53-56.
76. N. A. El Essawy, S. M. Ali, H. A. Farag, A. H. Konsowa, M. Elnouby and H. A. Hamad, *Ecotoxicology and environmental safety*, 2017, **145**, 57-68.
77. U. Paulus, T. Schmidt, H. Gasteiger and R. Behm, *Journal of Electroanalytical Chemistry*, 2001, **495**, 134-145.
78. W. S. Hummers Jr and R. E. Offeman, *Journal of the american chemical society*, 1958, **80**, 1339-1339.
79. M. Alfè, V. Gargiulo, R. Di Capua, F. Chiarella, J.-N. Rouzaud, A. Vergara and A. Ciajolo, *ACS applied materials & interfaces*, 2012, **4**, 4491-4498.

80. J. Zhang, G. B. White, M. D. Ryan, A. J. Hunt and M. J. Katz, *ACS Sustainable Chemistry & Engineering*, 2016, **4**, 7186-7192.
81. K. H. Habig, *Journal of Vacuum Science & Technology A: Vacuum, Surfaces, and Films*, 1986, **4**, 2832-2843.
82. C. W. Bale, E. Bélisle, P. Chartrand, S. A. Decterov, G. Eriksson, A. E. Gheribi, K. Hack, I. H. Jung, Y. B. Kang, J. Melançon, A. D. Pelton, S. Petersen, C. Robelin, J. Sangster, P. Spencer and M. A. Van Ende, *Calphad*, 2016, **54**, 35-53.
83. H. Reichert, O. Klein, H. Dosch, M. Denk, V. Honkimäki, T. Lippmann and G. Reiter, *Nature (London)*, 2000, **408**, 839-841.
84. R. Li, L. Wang, L. Li, T. Yu, H. Zhao, K. W. Chapman, Y. Wang, M. L. Rivers, P. J. Chupas, H.-K. Mao and H. Liu, *Scientific reports*, 2017, **7**, 5666-5667.
85. L.-Y. Chen, P.-H. Tang and T.-M. Wu, *The Journal of chemical physics*, 2016, **145**, 024506-024506.
86. J. Yang, J. S. Tse and T. Iitaka, *The Journal of chemical physics*, 2011, **135**, 044507-044507-044506.
87. M. Li, Y. Zhang, C. Wu and H. Geng, *Applied physics. A, Materials science & processing*, 2016, **122**.
88. D. J. González and L. E. González, *Journal of physics. Condensed matter*, 2008, **20**, 114118-114118.
89. N. Lei, Z. Huang and S. A. Rice, *The Journal of chemical physics*, 1996, **104**, 4802-4805.
90. E. DiMasi, H. Tostmann, O. G. Shpyrko, M. Deutsch, P. S. Pershan and B. M. Ocko, *Journal of physics. Condensed matter*, 2000, **12**, A209-A214.
91. N. Lei, Z. Huang, S. A. Rice and C. J. Grayce, *The Journal of chemical physics*, 1997, **106**, 9965-9965.
92. O. G. Shpyrko, A. Y. Grigoriev, R. Streitl, D. Pontoni, P. S. Pershan, M. Deutsch, B. Ocko, M. Meron and L. I. N. Binhua, *Physical review letters*, 2005, **95**, 106103.106101-106103.106104.
93. B. Yang, D. Gidalevitz, D. Li, Z. Huang and S. A. Rice, *Proceedings of the National Academy of Sciences - PNAS*, 1999, **96**, 13009-13011.
94. E. DiMasi, H. Tostmann, O. G. Shpyrko, P. Huber, B. M. Ocko, P. S. Pershan, M. Deutsch and L. E. Berman, *Physical review letters*, 2001, **86**, 1538-1541.
95. H. Niu, L. Bonati, P. M. Piaggi and M. Parrinello, *Nature communications*, 2020, **11**, 1-9.
96. G. Acres, G. C. Bond, B. Cooper and J. Dawson, *Journal of Catalysis*, 1966, **6**, 139-141.
97. C. P. Mehnert, R. A. Cook, N. C. Dispenziere and M. Afeworki, *Journal of the American Chemical Society*, 2002, **124**, 12932-12933.
98. N. Taccardi, M. Grabau, J. Debuschewitz, M. Distaso, M. Brandl, R. Hock, F. Maier, C. Papp, J. Erhard and C. Neiss, *Nature chemistry*, 2017, **9**, 862-867.
99. T. Daeneke, K. Khoshmanesh, N. Mahmood, I. De Castro, D. Esrafilzadeh, S. Barrow, M. Dickey and K. Kalantar-Zadeh, *Chemical Society Reviews*, 2018, **47**, 4073-4111.
100. R. Ueki, T. Nishijima, T. Hikata, S. Ookubo, R. Utsunomiya, T. Matsuba and J. I. Fujita, *Japanese Journal of Applied Physics*, 2012, **51**.
101. J. Prinz, C. A. Pignedoli, Q. S. Stöckl, M. Armbrüster, H. Brune, O. Gröning, R. Widmer and D. Passerone, *Journal of the American Chemical Society*, 2014, **136**, 11792-11798.
102. F.-M. Allioux, S. Merhebi, J. Tang, C. Zhang, A. Merenda, S. Cai, M. B. Ghasemian, M. A. Rahim, M. Maghe and S. Lim, *Carbon*, 2021, **171**, 938-945.

103. C. Palmer, E. Bunyan, J. Gelinas, M. J. Gordon, H. Metiu and E. W. McFarland, *Energy & Fuels*, 2020, **34**, 16073-16080.
104. M. Wolf, D. Narayanan Raman, N. Taccardi, M. Haumann and P. Wasserscheid, *ChemCatChem*, 2020, **12**, 1085.
105. M. Armbrüster, M. Behrens, F. Cinquini, K. Föttinger, Y. Grin, A. Haghofer, B. Klötzer, A. Knop-Gericke, H. Lorenz and A. Ota, *ChemCatChem*, 2012, **4**, 1048-1063.
106. A. Haghofer, K. Föttinger, F. Girgsdies, D. Teschner, A. Knop-Gericke, R. Schlögl and G. Rupprechter, *Journal of Catalysis*, 2012, **286**, 13-21.
107. B. J. L. Pérez, J. A. M. Jiménez, R. Bhardwaj, E. Goetheer, M. van Sint Annaland and F. Gallucci, *International Journal of Hydrogen Energy*, 2021, **46**, 4917-4935.
108. N. Raman, M. Wolf, M. Heller, N. Heene-Würl, N. Taccardi, M. Haumann, P. Felfer and P. Wasserscheid, *ACS Catalysis*, 2021, **11**, 13423-13433.
109. J.-i. Fujita, T. Hiyama, A. Hirukawa, T. Kondo, J. Nakamura, S.-i. Ito, R. Araki, Y. Ito, M. Takeguchi and W. W. Pai, *Scientific reports*, 2017, **7**, 1-10.
110. S. P. Tekade, A. S. Pednekar, G. R. Jadhav, S. E. Kalekar, D. Z. Shende and K. L. Wasewar, *International Journal of Hydrogen Energy*, 2020, **45**, 23954-23965.
111. J. N. Butler and M. L. Meehan, *Transactions of the Faraday Society*, 1966, **62**, 3524-3534.
112. W. Zhang, J. Z. Ou, S. Y. Tang, V. Sivan, D. D. Yao, K. Latham, K. Khoshmanesh, A. Mitchell, A. P. O'Mullane and K. Kalantar-zadeh, *Advanced Functional Materials*, 2014, **24**, 3799-3807.
113. N. Syed, A. Zavabeti, M. Mohiuddin, B. Zhang, Y. Wang, R. S. Datta, P. Atkin, B. J. Carey, C. Tan and J. van Embden, *Advanced Functional Materials*, 2017, **27**, 1702295.
114. X. Sun and H. Li, *RSC advances*, 2022, **12**, 24946-24957.
115. J. Lemus, J. Palomar, M. A. Gilarranz and J. J. Rodriguez, *Adsorption*, 2011, **17**, 561-571.
116. L. Rodríguez, D. Romero, D. Rodríguez, J. Sanchez, F. Domínguez and G. Arteaga, *Applied Catalysis A: General*, 2010, **373**, 66-70.
117. N. Raman, S. Maisel, M. Grabau, N. Taccardi, J. Debuschewitz, M. Wolf, H. Wittkämper, T. Bauer, M. Wu and M. Haumann, *ACS catalysis*, 2019, **9**, 9499-9507.
118. T. Bauer, S. Maisel, D. Blaumeiser, J. Vecchiotti, N. Taccardi, P. Wasserscheid, A. Bonivardi, A. Görling and J. r. Libuda, *ACS catalysis*, 2019, **9**, 2842-2853.
119. E. A. Redekop, V. V. Galvita, H. Poelman, V. Bliznuk, C. Detavernier and G. B. Marin, *ACS Catalysis*, 2014, **4**, 1812-1824.
120. K. Zuraiqi, A. Zavabeti, F.-M. Allieux, J. Tang, C. K. Nguyen, P. Tafazolymotie, M. Mayyas, A. V. Ramarao, M. Spencer and K. Shah, *Joule*, 2020, **4**, 2290-2321.
121. S. Yatsenko, N. Sabirzyanov and A. Yatsenko, 2008.
122. J. Poirier, *Geophysical Journal International*, 1988, **92**, 99-105.
123. N. H. El-Kaddah and D. Robertson, *Metallurgical Transactions B*, 1978, **9**, 191-199.
124. K. Kalantar-Zadeh, J. Tang, T. Daeneke, A. P. O'Mullane, L. A. Stewart, J. Liu, C. Majidi, R. S. Ruoff, P. S. Weiss and M. D. Dickey, *ACS nano*, 2019, **13**, 7388-7395.
125. H. Li, R. Abbasi, Y. Wang, F. M. Allieux, P. Koshy, S. A. Idrus-Saidi, M. A. Rahim, J. Yang, M. Mousavi and J. Tang, *Journal of Materials Chemistry C*, 2020, **8**, 1656-1665.
126. Y. Lin, J. Genzer and M. D. Dickey, *Advanced Science*, 2020, **7**, 2000192.
127. J. Yan, M. H. Malakooti, Z. Lu, Z. Wang, N. Kazem, C. Pan, M. R. Bockstaller, C. Majidi and K. Matyjaszewski, *Nature nanotechnology*, 2019, **14**, 684-690.

128. S. Chakraborty, *Microfluidics and microfabrication*, Springer New York, NY, New York, 1 edn., 2010.
129. I. Egry, E. Ricci, R. Novakovic and S. Ozawa, *Advances in colloid and interface science*, 2010, **159**, 198-212.
130. J. Liu and L. Yi, *Springer Series in Biomaterials Science and Engineering*, 2018, 96.
131. C. P. Sebastian, C. D. Malliakas, M. Chondroudi, I. Schellenberg, S. Rayaprol, R.-D. Hoffmann, R. Pöttgen and M. G. Kanatzidis, *Inorganic Chemistry*, 2010, **49**, 9574-9580.
132. M. G. Kanatzidis, R. Pöttgen and W. Jeitschko, *Angewandte Chemie International Edition*, 2005, **44**, 6996-7023.
133. H. Deming, *Journal of Chemical Education*, 1942, **19**, 336.
134. S. Yu and M. Kaviani, *The Journal of chemical physics*, 2014, **140**, 064303.
135. R. C. Chiechi, E. A. Weiss, M. D. Dickey and G. M. Whitesides, *Angewandte Chemie International Edition*, 2008, **47**, 142-144.
136. D. Zrnic and D. Swatik, *Journal of the less common metals*, 1969, **18**, 67-68.
137. T. Geißler, A. Abánades, A. Heinzl, K. Mehravarán, G. Müller, R. K. Rathnam, C. Rubbia, D. Salmieri, L. Stoppel and S. Stückrad, *Chemical Engineering Journal*, 2016, **299**, 192-200.
138. C. Palmer, D. C. Upham, S. Smart, M. J. Gordon, H. Metiu and E. W. McFarland, *Nature Catalysis*, 2020, **3**, 83-89.
139. D. C. Upham, V. Agarwal, A. Khechfe, Z. R. Snodgrass, M. J. Gordon, H. Metiu and E. W. McFarland, *Science*, 2017, **358**, 917-921.
140. A. Y. Lee, K. Yang, N. D. Anh, C. Park, S. M. Lee, T. G. Lee and M. S. Jeong, *Applied Surface Science*, 2021, **536**, 147990.
141. L. Tsechansky and E. Graber, *Carbon*, 2014, **66**, 730-733.
142. M. W. Smith, I. Dallmeyer, T. J. Johnson, C. S. Brauer, J.-S. McEwen, J. F. Espinal and M. Garcia-Perez, *Carbon*, 2016, **100**, 678-692.
143. V. A. Minaeva, B. F. Minaev, G. V. Baryshnikov, H. Ågren and M. Pittelkow, *Vibrational Spectroscopy*, 2012, **61**, 156-166.
144. C. Thomsen and S. Reich, *Physical review letters*, 2000, **85**, 5214.
145. J. McDonald-Wharry, M. Manley-Harris and K. Pickering, *Carbon*, 2013, **59**, 383-405.
146. C. Hu, S. Sedghi, A. Silvestre-Albero, G. G. Andersson, A. Sharma, P. Pendleton, F. Rodríguez-Reinoso, K. Kaneko and M. J. Biggs, *Carbon*, 2015, **85**, 147-158.
147. L. H. Baekeland, *Industrial & Engineering Chemistry*, 1909, **1**, 149-161.
148. T. M. Letcher, *Plastic waste and recycling: Environmental impact, societal issues, prevention, and solutions*, Academic Press, 2020.
149. P. Villars, K. Cenzual, H. Okamoto, F. Hulliger and S. Iwata, *PAULING FILE Multinaries Edition—2012*, Springer Materials, 2012.
150. T. Geißler, M. Plevan, A. Abánades, A. Heinzl, K. Mehravarán, R. K. Rathnam, C. Rubbia, D. Salmieri, L. Stoppel and S. Stückrad, *International Journal of Hydrogen Energy*, 2015, **40**, 14134-14146.
151. M. Plevan, T. Geißler, A. Abánades, K. Mehravarán, R. K. Rathnam, C. Rubbia, D. Salmieri, L. Stoppel, S. Stückrad and T. Wetzl, *International Journal of Hydrogen Energy*, 2015, **40**, 8020-8033.
152. C. Palmer, M. Tarazkar, H. H. Kristoffersen, J. Gelinas, M. J. Gordon, E. W. McFarland and H. Metiu, *ACS Catalysis*, 2019, **9**, 8337-8345.
153. K. O'Farell, *National Report*, Report R01-04-A21502, Australian Government, Canberra 2018.

154. J. D. Peterson, S. Vyazovkin and C. A. Wight, *Macromolecular Chemistry and Physics*, 2001, **202**, 775-784.
155. B. Girija, R. Sailaja and G. Madras, *Polymer Degradation and stability*, 2005, **90**, 147-153.
156. S. Jipa, T. Zaharescu, R. Setnescu, E. Drăgan and M. Dinu, *Materials Chemistry and Physics*, 2008, **112**, 612-616.
157. T. J. Xue, M. A. McKinney and C. A. Wilkie, *Polymer Degradation and Stability*, 1997, **58**, 193-202.
158. D. Fătu, G. Geambaș, E. Segal, P. Budrugaec and S. Ciutacu, *Thermochimica acta*, 1989, **149**, 181-187.
159. K. Pramoda, T. Liu, Z. Liu, C. He and H.-J. Sue, *Polymer degradation and Stability*, 2003, **81**, 47-56.
160. A. Dhahak, C. Grimmer, A. Neumann, C. Rüger, M. Sklorz, T. Streibel, R. Zimmermann, G. Mauviel and V. Burkle-Vitzthum, *Waste Management*, 2020, **106**, 226-239.
161. D. Kang, N. Rahimi, M. J. Gordon, H. Metiu and E. W. McFarland, *Applied Catalysis B: Environmental*, 2019, **254**, 659-666.
162. L. Liu, Y. Duan, L. Ma, S. Liu and Z. Yu, *Applied Surface Science*, 2010, **257**, 842-846.
163. A. P. Chauhan and K. Chawla, *Journal of Molecular Liquids*, 2016, **221**, 292-297.
164. M. N. Subramanian, *Plastics additives and testing*, John Wiley & Sons, United States of America, 2013.
165. M. Bilton, A. Brown and S. Milne, 2012.
166. G. Levi, O. Senneca, M. Causà, P. Salatino, P. Lacovig and S. Lizzit, *Carbon*, 2015, **90**, 181-196.
167. R. Larciprete, P. Lacovig, S. Gardonio, A. Baraldi and S. Lizzit, *The Journal of Physical Chemistry C*, 2012, **116**, 9900-9908.
168. A. Barinov, O. B. Malcioglu, S. Fabris, T. Sun, L. Gregoratti, M. Dalmiglio and M. Kiskinova, *The Journal of Physical Chemistry C*, 2009, **113**, 9009-9013.
169. G. Alfke, W. W. Irion and O. S. Neuwirth, *Ullmann's Encyclopedia of Industrial Chemistry*, 2000.
170. J. G. Speight, *The refinery of the future*, Gulf Professional Publishing, 2020.
171. G. Lopez, M. Artetxe, M. Amutio, J. Alvarez, J. Bilbao and M. Olazar, *Renewable and Sustainable Energy Reviews*, 2018, **82**, 576-596.
172. A. H. Kuptsov and G. N. Zhizhin, *Handbook of Fourier Transform Raman and Infrared Spectra of Polymers*, Elsevier Science & Technology, Amsterdam, 1998.
173. M. W. Chase Jr and N.-J. T. Tables, *J. Phys. Chem. Ref. Data, Monograph*, 1998, **9**, 1-1951.
174. L. Qiu, V. Murashov and M. A. White, *Solid state sciences*, 2000, **2**, 841-846.
175. R. Rennie and J. Law, *A dictionary of chemistry*, Oxford University Press, 2016.
176. R. Chang and K. A. Goldsby, *General Chemistry: The Essential Concepts*, McGraw Hill, New York, N.Y, SEVENTH EDITION. edn., 2013.
177. A. Julbe and M. Drobek, in *Encyclopedia of Membranes*, eds. E. Drioli and L. Giorno, Springer Berlin Heidelberg, Berlin, Heidelberg, 2016, DOI: 10.1007/978-3-662-44324-8_604, pp. 2055-2056.
178. H. Shintaku, K. Nakajima, M. Kitano, N. Ichikuni and M. Hara, *ACS Catalysis*, 2014, **4**, 1198-1204.
179. S. Singh, M. K. Ghorai and K. K. Kar, *Handbook of Fly Ash*, 2022, 403.

180. J.-B. Donnet and A. Voet, *Carbon black: physics, chemistry, and elastomer reinforcement*, M. Dekker, 1976.
181. T. Ungár, J. Gubicza, G. Ribárik, C. Pantea and T. W. Zerda, *Carbon*, 2002, **40**, 929-937.
182. M. Smith, *March's advanced organic chemistry : reactions, mechanisms, and structure*, Wiley, Hoboken, 7th edition / Michael B. Smith, Professor of Chemistry. edn., 2013.
183. Y.-R. Luo, *Handbook of bond dissociation energies in organic compounds*, CRC press, 2002.